

Håvard Omvik Furdal and Jørgen Røkkum Vevang

Assessment of Elgeseter Bridge Suffering from Alkali-Silica Reactions

Analysis and capacity verification of the bridge
deck with finite element shell models

Master's thesis in Civil and Environmental Engineering

Supervisor: Terje Kanstad

June 2021

Håvard Omvik Furdal and Jørgen Røkkum Vevang

Assessment of Elgeseter Bridge Suffering from Alkali-Silica Reactions

Analysis and capacity verification of the bridge deck
with finite element shell models

Master's thesis in Civil and Environmental Engineering
Supervisor: Terje Kanstad
June 2021

Norwegian University of Science and Technology
Faculty of Engineering
Department of Structural Engineering





MASTER THESIS 2021

SUBJECT AREA: Concrete Structures	DATE: 11.06.2021	NO. OF PAGES: 12 + 140 + 35 = 187
--------------------------------------	---------------------	--------------------------------------

TITLE:

Assessment of Elgeseter Bridge Suffering from Alkali-Silica Reactions
Analysis and capacity verification of the bridge deck with finite element shell models

Tilstandsvurdering av Elgeseter bru utsatt for alkalireaksjoner
Analyse og kapasitetsverifikasjon av brudekket ved bruk av skallelementer

BY:

Håvard Omvik Furdal
Jørgen Røkkum Vevang



SUMMARY:

This master's thesis is a condition assessment of the plates in Elgeseter Bridge, focusing on the effects of alkali-silica reactions (ASR). Elgeseter Bridge is a 200 m long bridge with 9 spans and non-tensioned reinforcement. Core samples have revealed comprehensive ASR, and several cracks have been observed in both beams and columns.

ASR is a chemical reaction in concrete occurring when alkali-reactive aggregates react with alkaline pore water. The reaction product, a swelling gel, causes a volumetric expansion of the concrete. Elgeseter Bridge is estimated to have elongated 180 mm since it was built in 1951. Local variations in the aggregate and different access to humidity have caused a varying degree of ASR within the structure. Both the global elongation and the varying expansion between components introduce additional forces in the bridge.

In this study, dimensioning forces are obtained by a linear elastic finite element analysis (FEA) in Abaqus. Elgeseter Bridge is modelled with shell elements to describe the effects of simultaneously acting forces. The utilization of critical shell sections is assessed in the ultimate limit state through a capacity control using the Iteration Method.

According to the capacity control, the most critical sections are located in the column axes in the middle of the plate between the inner and outer beams. If yielding in the reinforcement is considered as a failure criterion, the utilization ratio is 5.26 in a typical column axis and 6.25 in the northernmost column axis. The reinforcement is, in general, highly utilized in sections along column axes because of significant tensile forces.

Yielding in the reinforcement is detected in 17 of the 32 controlled sections. Among these, 14 sections exceed their capacities if a failure strain of 10‰ in the reinforcement is used as the failure criterion. The capacity control reveals that 9 sections reach failure in the concrete just before failure strain is obtained in the reinforcement.

RESPONSIBLE TEACHER: Professor Terje Kanstad

SUPERVISOR(S): Terje Kanstad, NTNU, Kathrine Stemland, NTNU, Max Hendriks, NTNU, Håvard Johansen, The Norwegian Public Roads Administration

CARRIED OUT AT: Department of Structural Engineering, NTNU

Preface

This master's thesis concludes our five-year master's degree in Civil and Environmental Engineering at The Norwegian University of Science and Technology. It is written in corporation with The Department of Structural Engineering and The Norwegian Public Roads Administration during the spring of 2021.

Writing this thesis has led to many academic discussions, both with each other and with the supervisors. We are grateful for the opportunity to have Elgeseter Bridge as a topic in our thesis. It has given us deep insight in concrete structures suffering from alkali-silica reactions and finite element analysis with shell elements.

The program used in the capacity control is developed by Micael Hailemichael during his master's thesis. The collaboration has been beneficial for both parties, as results provided during the capacity control in this thesis has been useful feedback to the further development of the program. We are thankful for the opportunity of using the program and for interesting discussions regarding capacity controls with shell elements.

We would first like to thank our supervisor, Professor Terje Kanstad for valuable guidance and feedback throughout this semester. Our co-supervisors Kathrine Stemland and Max Hendriks at NTNU and Håvard Johansen in The Norwegian Public Roads Administration also deserve our gratitude.

*Håvard Omvik Furdal and Jørgen Røkkum Vevang
Trondheim, June 2021*

Abstract

This master's thesis is a condition assessment of the plates in Elgeseter Bridge, focusing on the effects of alkali-silica reactions (ASR). Elgeseter Bridge is a 200 m long bridge with 9 spans and non-tensioned reinforcement. Core samples have revealed comprehensive ASR, and several cracks have been observed in both beams and columns.

ASR is a chemical reaction in concrete occurring when alkali-reactive aggregates react with alkaline pore water. The reaction product, a swelling gel, causes a volumetric expansion of the concrete. Elgeseter Bridge is estimated to have elongated 180 mm since it was built in 1951. Local variations in the aggregate and different access to humidity have caused a varying degree of ASR within the structure. Both the global elongation and the varying expansion between components introduce additional forces in the bridge.

In this study, dimensioning forces are obtained by a linear elastic finite element analysis (FEA) in Abaqus. Elgeseter Bridge is modelled with shell elements to describe the effects of simultaneously acting forces. The utilization of critical shell sections is assessed in the ultimate limit state through a capacity control using the Iteration Method.

According to the capacity control, the most critical sections are located in the column axes in the middle of the plate between the inner and outer beams. If yielding in the reinforcement is considered as a failure criterion, the utilization ratio is 5.26 in a typical column axis and 6.25 in the northernmost column axis. The reinforcement is, in general, highly utilized in sections along column axes because of significant tensile forces.

Yielding in the reinforcement is detected in 17 of the 32 controlled sections. Among these, 14 sections exceed their capacities if a failure strain of 10‰ in the reinforcement is used as the failure criterion. The capacity control reveals that 9 sections reach failure in the concrete before failure strain is obtained in the reinforcement.

Sammendrag

Det er i denne oppgaven utført en tilstandsvurdering av bruplaten i Elgeseter bru med fokus på lastvirkningene fra alkalireaksjoner. Elgeseter bru er en slakkarmert betongbru på 200 m som består av 9 spenn. Kjerneprøver av betongen har vist at brua er utsatt for omfattende ASR. Flere store sprekker er observert både i bjelker og søyler.

ASR er en kjemisk reaksjon i betongen som oppstår når alkali-reaktivt tilslag reagerer med alkalisk porevann. Reaksjonsproduktet er en alkaligel som sveller under vannabsorpsjon og fører til en ekspansjon i betongen. Det er estimert at Elgeseter bru har forlenget seg med 180 mm siden den ble bygget i 1951. Lokale variasjoner i tilslaget i betongen og ulik tilgang på fuktighet har ført til variende grad av ASR i konstruksjonen. Både den globale forlengelsen og ulik ekspansjon mellom konstruksjonsdeler fører til tilleggskrefter i brua.

Det er utført en lineær-elastisk elementanalyse i Abaqus for å bestemme de dimensjonerende lastvirkningene. Elgeseter bru er modellert med skall-elementer for å ivareta lastvirkningen i flere retninger samtidig. Utnyttelsesgrader for kritiske snitt er beregnet i bruddgrensetilstand ved bruk av Iterasjonsmetoden.

De mest kritiske snittene er å finne i midtplata mellom ytter- og innerbjelker i søyleaksene, ifølge kapasitetsprogrammet. Ved bruk av flytning i armeringen som bruddkriterie er utnyttelsesgradene 5.26 i en typisk søyleakse og 6.25 i den nordligste søyleaksen. Lengdearmeringen er generelt høyt utnyttet langs søyleaksene som følge av store strekkrefter.

Det oppstår flytning i armeringen for 17 av de 32 kontrollerte snittene. Ved å betrakte en bruddtøyning på 10‰ i armeringen som bruddkriterie, vil 14 av disse snittene få overskridelse i kapasitet. Kapasitetskontrollen viser at 9 snitt får brudd i betongen før bruddtøyning i armeringen er oppnådd.

Contents

Preface	iii
Abstract	v
Sammendrag	vii
Contents	ix
1 Introduction	1
1.1 Background and Motivation	1
1.2 Scope and Limitations	2
2 Alkali-Silica Reactions	3
2.1 Mechanical Properties	5
3 Elgeseter Bridge	9
3.1 Geometry and Static System	10
3.2 Alkali-Silica Reactions in Elgeseter Bridge	11
3.2.1 Status of Columns	14
3.2.2 Status of Bridge Deck	15
3.2.3 Status of Beams	16
3.2.4 ASR in Elgeseter Bridge in the Future	17
4 Guidelines and Materials	19
4.1 Standards	19
4.2 Handbooks	20
4.3 Material Properties	20
4.3.1 Concrete	20
4.3.2 Reinforcement	22
4.4 Cover	23
5 Loads and Load Combinations	25
5.1 Permanent Loads	25
5.1.1 Self-weight	25
5.1.2 Super-self-weight	26
5.2 Variable Loads	28
5.2.1 Traffic Load	28
5.2.2 Temperature Load	32
5.3 Deformation Loads	34
5.3.1 Creep	34
5.3.2 Shrinkage	34
5.4 Accidental Loads	35

5.5	Load Combinations ULS	35
6	Loads from Alkali-Silica Reactions	37
6.1	Internal Load-effects	37
6.2	External Load-effects	39
6.3	Calculation Models Accounting for ASR	43
6.3.1	Load Model 1	44
6.3.2	Load Model 2	44
6.3.3	Load Model 3	45
6.4	ASR Loads in the Longitudinal Direction	46
6.4.1	Geometry used by Aas-Jakobsen	46
6.4.2	Free Expansion	47
6.4.3	ASR Loads from Aas-Jakobsen	48
6.4.4	Transformation of Loads from Aas-Jakobsen	49
6.5	ASR Loads in the Transverse Direction	50
6.5.1	Free Expansion	50
6.5.2	Distribution of Reinforcement in the Transverse Direction	51
6.5.3	Process to Determine ASR Loads in the Transverse Direction	52
6.6	Deviation in Procedure to Determine the ASR Loads	55
7	Finite Element Analysis in Abaqus/CAE	57
7.1	Modelling	58
7.1.1	Elements and Mesh	58
7.2	Geometry and Material Properties	59
7.3	Boundary Conditions and Constraints	60
7.4	Loads	61
7.4.1	Self-weight	61
7.4.2	Traffic Load	61
7.4.3	Temperature Load	64
7.4.4	Alkali Silica Reactions	65
7.5	Derivation of Results	66
7.6	Verification of Results	68
8	Interpretation of Forces	71
8.1	Critical Sections	71
8.2	Self-weight	73
8.3	Traffic Load	75
8.4	Temperature Load	77
8.5	Alkali-Silica Reactions	78
8.5.1	ASR in the Longitudinal Direction	79
8.5.2	ASR in the Transverse Direction	81
9	Resulting Forces	85
9.1	Load Combinations	85
9.1.1	Axis 6 (S1)	86
9.1.2	Zero bending moment span 6 (S2)	88
9.1.3	Mid-span between axis 6 and 7 (S3)	90
9.1.4	Axis 9 (S4)	92

9.1.5	Section with max field moment from self-weight span 9 (S5)	94
9.1.6	Section with large in-plane shear forces from ASR (S6)	96
9.1.7	Axis 10 (S7)	98
9.2	Reinforcement	100
10	Capacity Control in ULS	103
10.1	Capacity Control by the Iteration Method	103
10.1.1	Principals in the Iteration Method	103
10.1.2	Input to the Program	110
10.1.3	Output from the Program	113
10.1.4	Results from the Iteration Method	115
10.1.5	Verification of the Capacity Program using the Membrane Method	118
11	Discussion	123
11.1	ASR Effects	123
11.2	Modelled Stiffness	124
11.3	Modelled Mesh and Loads	125
11.4	Capacity Control	126
11.5	The Capacity Program	130
12	Conclusion	133
	Bibliography	137
A	Drawings	141
B	Verification of ASR Loads from Aas-Jakobsen	149
C	Verification of Bending Moment due to Self-Weight	153
D	Verification of the Iteration Method by the Membrane Method	163

Chapter 1

Introduction

1.1 Background and Motivation

Concrete is one of the most popular building materials, and it is used in many Norwegian bridges. Its structural properties regarding compressive strength, formability and durability combined with the low price and high availability make concrete an attractive material. Combining concrete and reinforcement results in a ductile construction material well suited for advanced structures as long-span bridges. [1]

Concrete has for a long time been considered to be a material with minimal need for rehabilitation and inspection. However, many old concrete structures have shown signs of degradation during the last years. Limited knowledge regarding degradation mechanisms led to minimal attention to durability and maintenance in earlier standards and rule sets. The consequences become apparent today as many structures constructed in accordance with the old standards are starting to age.

This thesis focuses on the structural impact of deterioration due to alkali-silica reactions (ASR) in concrete. ASR is a chemical reaction occurring as alkali-reactive aggregates react with alkaline pore water. The reaction product, a characteristic swelling gel, causes a volumetric expansion of the concrete. An increase in volume can create cracks making both the concrete and the reinforcement more vulnerable to other degradation mechanisms and intrusions from different damaging chemicals. Expansion caused by ASR can further generate significant restraint forces in statically indeterminate systems. [2]

Elgeseter Bridge is a structure prone to expansions due to ASR and has since 1990 been continuously monitored by The Norwegian Public Roads Administration. Several inspections, calculation reports, and master's theses have addressed the structural influence of ASR in the bridge. Large cracks have been observed, and different repairs have been conducted to limit the damage and maintain the

capacity of the bridge. However, great uncertainties are still related to the damage and the capacity of the structure.

1.2 Scope and Limitations

The main focus in previous work regarding Elgeseter Bridge has been related to the damage and the capacity of the columns and the beams. To bring the assessment of the bridge forward, the scope of this thesis is to evaluate the capacity of the bridge plate and to enlighten critical load cases and sections.

Elgeseter Bridge is primarily designed to resist vertical loads, such as self-weight and traffic loads, temperature loads, and loads due to minor deformations from creep and shrinkage. However, the expansions from ASR have created a completely different load situation in the bridge. The current load situation includes forces of magnitudes and directions that were not taken into account when Elgeseter Bridge was designed in 1951. Even though ASR expansions in some sections have beneficial contributions, it is decided to mainly focus on load combinations where ASR has unfavourable contributions.

Dimensioning forces are found by modelling the whole bridge in the finite element analysis (FEA) software Abaqus. An essential choice of this task is to perform the FEA using shell elements. Application of shell elements is desired to perceive the effects of all the simultaneously acting forces. After determination of the most decisive load combinations in the critical sections, the degree of utilization is obtained by the Iteration Method [1] through a program developed by M. Hailemichael [3]. The capacity control in this thesis is limited to only consider forces included in the Iteration Method. Out-of-plane shear forces are therefore not part of the capacity control.

Theory regarding ASR, Elgeseter Bridge, the basis of dimensioning, and different loads are reviewed in Chapters 2-6. Chapter 7 displays the establishment of the shell model, while Chapter 8 interprets the responses obtained from the FEA. Chapter 9 presents the resulting load combinations further used in the capacity control conducted in Chapter 10. General aspects regarding the thesis and the condition of the plates in Elgeseter Bridge are discussed in Chapter 11, and summed up in a conclusion in Chapter 12.

Chapter 2

Alkali-Silica Reactions

Alkali-silica reaction (ASR) is the chemical reaction between alkalis and silica from the reactive aggregates. The reaction product is an alkali-silica gel that swells by water absorption. As a result, pressure develops in the gel and causes tensile stresses in the surrounding material. The tensile stresses cause cracking in the concrete and can also lead to further damage in the concrete combined with other degradation mechanisms such as carbonation and chloride penetration [4].

Three conditions must be fulfilled to develop ASR:

- Reactive aggregates (SiO_2)
- Sufficient availability of alkalis in the cement (Na^+ , K^+) and hydroxide ions (OH^-)
- Moist content with relative humidity (RH) of at least 80-90%

The reaction will not occur if one of these conditions are absent. A higher temperature will increase the rate of the ASR-process [2]. The three necessary conditions are illustrated in Figure 2.1.

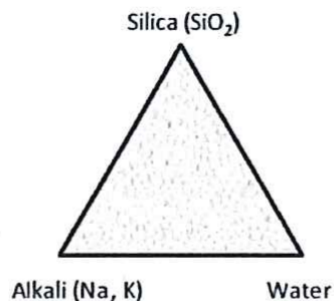


Figure 2.1: Illustration of the three necessary conditions for the ASR-process

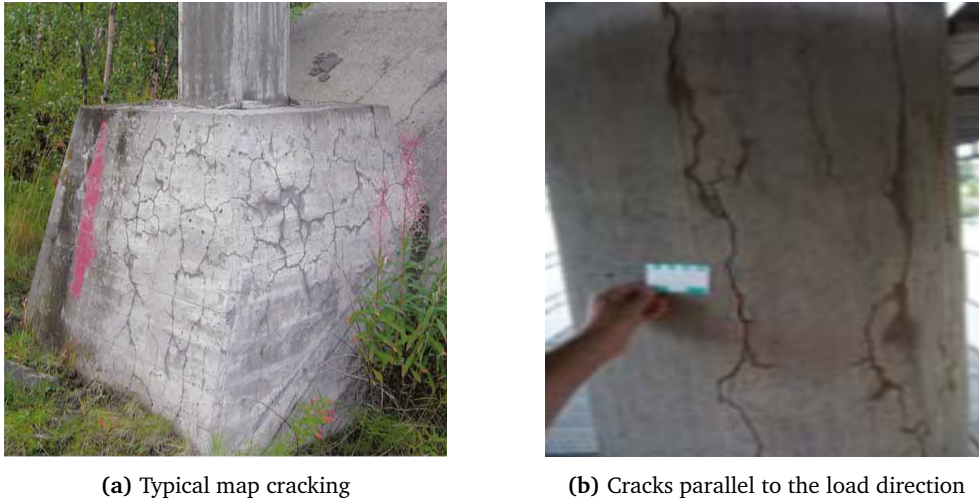


Figure 2.2: The different types of crack patterns related to ASR [2]

As a result of the relative humidity criteria, outdoor concrete structures such as bridges and dams are more exposed to ASR. Local variations in relative humidity and aggregates in the concrete result in expansion differences in the structure. The expansion may vary within one element or between different structural elements. Furthermore, the expansion may also vary over the cross-section and therefore, the measured ASR expansion on the surface of the concrete is just an expression for the average [5]. The outer layer of the exposed concrete will alternately dry out and moisten, typically the outer 5-10 cm of the concrete. Every time the concrete dries out, water will carry some alkali ions out to the surface. Hence, the alkali content near the surface will be lower, leading to better conditions for the ASR to develop a few centimetres within the concrete. Therefore, the combination of larger expansion within the concrete, leaking of alkali ions on the surface, and some shrinkage in the concrete can cause cracking on the surface. Cracks occur when the tensile strength of concrete is exceeded. Furthermore, the cracks can be filled with water when exposed to rain, leading to favourable conditions for further ASR expansion.

When the alkali-silica gel absorbs water and swell, the volume of the concrete will increase and cause a characteristic network of fine cracks joined up in polygonal shapes named "map cracking". This can be seen on the concrete surface, where the concrete is free to expand. These cracks usually do not get more profound than 25-50 mm of the exposed surface and seldom go beyond 100 mm in massive structures [6]. The cracking pattern will often reflect the underlying reinforcement in the concrete. In structural elements where there are longitudinal compressive stresses in the member, cracks will tend to be parallel to the load direction [6]. The different types of cracks are illustrated in Figure 2.2.

Portland cement is a commonly used cement in Norway. Cement is an essential source of acid-soluble contents in concrete. To determine the alkali content in the concrete, it has become a standard practice to express alkali content in terms of mass percentage "sodium equivalent", which can be expressed by Equation (2.1). The constant 0.658 considers that K_2O has a more significant molecular weight than Na_2O . In order to minimize deterioration of concrete, the limit regarding the alkali content in Portland cement has been set to 0.6% Na_2O_{eq} . When the alkali content is lower than this limit, the concrete is accepted as secure against deleterious alkali-silica reactions. However, many concrete structures diagnosed with ASR deterioration were constructed using cement with alkali content up to 1.4% Na_2O_{eq} [7].

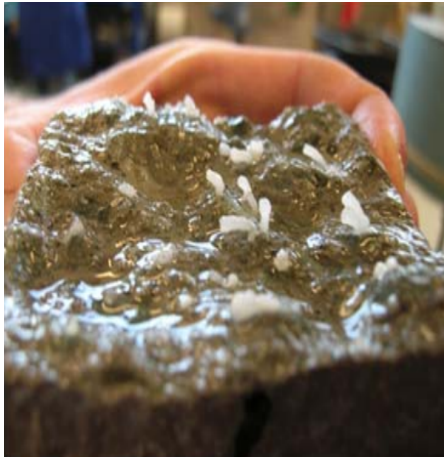
$$\%Na_2O_{equivalent} = \%Na_2O + 0.658\%K_2O \quad (2.1)$$

The Norwegian alkali-reactive aggregates are so-called slowly reactive. Because of the relatively cold climate in Norway, it usually takes at least 10-15 years before the cracks due to ASR will develop on the concrete surface. Therefore, a somewhat usual assumption was that ASR would not be a significant problem in Norway. The problem was regarded as non-existing until 1990. However, many structures have now exceeded fifty years in service life. Because of that, ASR has become a serious issue and is one of the most severe degradation mechanism for concrete structures. For structures built today in an environment with high relative humidity, the problem related to ASR is solved using nonreactive aggregates or low alkali cement [5].

Other conditions like high curing temperatures, shrinkage, and freeze-thaw cycles, may give similar cracks as the characteristic ASR map cracking. Therefore, it is important to identify the cause of the deterioration of the concrete structure with a site inspection and tests in the laboratory of drilled cored samples. It is essential to control critical areas such as important locations for structural stability and safety or areas subjected to unusually severe exposure [6]. Figure 2.3 illustrates different types of ASR gel. The presence of a white gel on the surface of the concrete indicates the presence of ASR. Such deposits on the surface can also be caused by other degradation mechanisms such as frost action.

2.1 Mechanical Properties

Most of the research related to ASR has been focused on the chemical aspect, but it has been an increasing focus on the structural consequences regarding ASR in recent years. Alkali-silica reaction in concrete is a complex phenomenon, and not many models have been developed describing the structural effects of the reaction. However, some models to calculate the effect of shrinkage in concrete



(a) ASR from a laboratory cast concrete sample



(b) Normal occurrence of ASR gel on structures

Figure 2.3: Alkali-silica gel in the form of "ASR worms" from a laboratory concrete sample (a) and "traditional ASR gel" (b) from a drilled concrete core [2]

can also be used to describe the effect of ASR. Nevertheless, the expansion from ASR is more significant than the volume reduction from shrinkage. ASR also affect the mechanical properties of concrete. The most important properties affected by ASR are the tensile strength, compressive strength, and Young's modulus [5].

The material properties in terms of strength and stiffness depend on the degree and orientation of the micro-cracks in the material and if macro-cracks are present. The expansion is smaller in the compressive stress direction, resulting in an anisotropic material behaviour [4]. Several studies have been done on the mechanical properties affected by ASR in recent years. Barbosa et al. [8] studied how the degree and orientation of both micro and macro-cracks due to ASR influenced the compressive strength and modulus of elasticity in drilled cores from ASR-damaged slab bridges. They found that the compressive strength and the stiffness were lower in the direction perpendicular to the cracks than in the direction parallel to the cracks. Giaccio et al. [9] came to the same conclusion by studying laboratory cast cylinders exposed to accelerated ASR and uniaxial loading, which means that the compressive strength and stiffness are higher in the directions where the cracks are oriented in the loading direction. Gautam et al. [10] confirmed the result that the expansion, cracking, and change in stiffness were dependent on the stress state by studying cores that were drilled from cubes exposed to different stress states under accelerated ASR conditions.

It has been shown that the damage due to ASR is hard to evaluate based on the physical measurements on the surface of the concrete. This is due to the anisotropic behaviour of ASR. Therefore, mechanical testing and petrographic

examination on drilled cores from the structure are the most efficient methods to examine the current state of the structure. One of these tests is the stiffness damage test (SDT). Sanches et al. [11] used this method by carrying out five load cycles in compression on cylinders and cores, which consisted of various compressive strength and different reactive aggregates. Based on the recorded stresses and strains, the damage parameters could be calculated. Furthermore, they found that a stress level of 40% of the 28 days compressive strength was sufficient to determine the damage as a function of the expansion level. As a result of the test, several parameters such as the modulus of elasticity, stiffness damage index, plastic damage index and non-linearity index were shown to be a function of the expansion level [4].

It is well known that concrete has low tensile capacity. According to The Norwegian Public Road Administration (NPRA), the tensile capacity can in some directions be approximately zero if the expansion exceeds 1 ‰ [5]. When designing structures in ULS it is common practice to insert reinforcement to take all the tensile forces. However, the shear- and bond strength capacity formulas still rely on the tensile capacity of the concrete. This is especially the case for the bond strength in the anchorage areas. It can be quite challenging to get sufficient capacity in these areas if the concrete does not have any tensile capacity. Therefore, ASR and expansion in these areas can have significant consequences for the bearing capacity.

The expansion due to ASR is expected to be largest for unrestrained structures. For partly or fully restrained structures, the expansion may stop in the current direction if the compressive stress in the same direction is sufficient high [4]. However, there are disagreements among researchers regarding the necessary compressive stress to stop the expansion. The modulus of elasticity is dependent on the direction of expansion relative to the load direction. For the unrestrained direction, the modulus of elasticity will be quite low until the expansion or the gel in the pores is compressed. For the restrained direction, on the other hand, the modulus of elasticity will have a small reduction in the load direction if the compressive stress is sufficiently large [4].

The compressive strength is less sensitive to the expansion than the tensile capacity and Young's modulus. It is suggested that the compressive strength is reduced when the expansion exceeds approximately 2-3 ‰, or if delamination occurs. Therefore the modulus of elasticity and the tensile capacity are considered to be the most critical parameters due to the effects of ASR [5].

Chapter 3

Elgeseter Bridge

In 1949 the city council of Trondheim decided to build a new bridge crossing Nidelva as a part of the European route E6 highway. Two years later, in 1951, the new concrete bridge named Elgeseter Bridge was opened. The bridge connects Elgeseter street in the south and the city centre of Trondheim in the north [12]. Figure 3.1 shows a picture of the bridge.



Figure 3.1: Elgeseter Bridge seen from the east [12]

The passage from Elgeseter to the city centre has a long history, and several bridges have stood at the same location as today's bridge. The first documented bridge crossing the river at this location is found in 1178, and since then, this has been one of the main entryways into the city of Trondheim. Different versions and renewals of the bridge were the only way to get into the city until the great city fire in 1681. During the reconstruction of the city after the fire, a new bridge was built further down the river at Bakklundet. The new bridge, named Old Town Bridge, became the new main entrance to the city, and the bridge at Elgeseter

then rapidly decayed. It took almost 200 years before a new bridge was built at Elgeseter. This new wooden bridge, named Kongsgaards bridge, was opened in 1863 as a part of the railway Stoerenbanen. [13]

In 1945, after the war, a great architect competition was held during the planning of a new bridge at Elgeseter. Among the twenty-seven contesters, the winners were Aas-Jakobsen and the architects Gundolf Blakstad and Herman Munthe-Kaas. It was built by engineer F. Selmer AS [14]. Together they made Elgeseter Bridge as we know it today.

In 2004 Elgeseter Bridge received the award "Betongtavlen" from the Norwegian Concrete Association. In the jury's justification, the bridge was described as an outstanding, future-oriented and beautiful construction. It was also mentioned that its good technical condition illustrates the properties of concrete as a durable material. In 2008 the bridge was declared protected by the Norwegian Directorate for Cultural Heritage. Its design with the slender columns is mentioned to have a high architectural value [15].

3.1 Geometry and Static System

Elgeseter Bridge is a 200 meters long concrete bridge consisting of 9 spans. The length of the end-spans is 21.25 m, while the rest of the spans have lengths of 22.5 m. The bridge is 23.4 meters wide and holds four traffic lanes for cars and two walkways, one on each side. Both walkways have separated lanes for pedestrians and bikers. Over the two spans at the south end, the pedestrian narrows in favour of a fifth traffic lane [16].

For simplicity, the bridge is divided into an axis system used throughout the report. The spans and the column rows are independently counted from south to north, as illustrated in Figure 3.2. Blue numbers count supports and columns, while numbers in red count spans. In addition, the terms west side and east side are used to describe the bridge in the transverse direction.

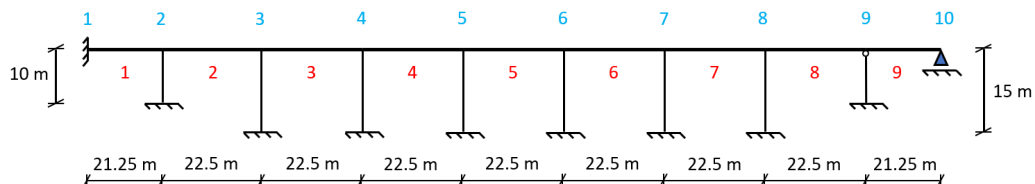


Figure 3.2: Static system

The cross-section of the bridge consists of four equal concrete beams with dimensions 800x1430 mm and a centre distance of 5.5 meters. The beams have

non-tensioned reinforcement and are continuous. The beams and the plates are monolithically cast as one. The plates have a thickness varying between 150-380 mm. The four beams and the bridge deck make the load-carrying girder of the bridge. [16]

The girder is supported by 8 column rows. Monolithic connections between the beams and the columns in axis 2-8 can transfer bending moments between the two components. Columns in axis 9, on the other hand, have a pinned connection to the beams, meaning that no moments are transferred. All columns have a circular cross-section with a diameter of 800 mm. Columns in axis 2 and 9 have a length of 10 m, while columns in axis 3-8 are 15 m. All columns are fixed in the bottom by concrete foundations and piles. The piles supporting the columns are made of timber, while piles at the end supports are made of concrete. [16]

The abutment in axis 1, closest to Elgeseter street in the south, is constructed to be fixed. This end is therefore considered stiff and can move neither vertically nor horizontally. Beams are also constrained from rotating about their axis. In axis 10, on the other hand, the abutment is constructed as a roller with an expansion joint. It can therefore move horizontally in the longitudinal direction of the bridge. [16]

3.2 Alkali-Silica Reactions in Elgeseter Bridge

Elgeseter Bridge has shown signs of expansion in both the columns, the beams and the bridge deck. In 1985, an inspection revealed that the bridge had experienced an elongation of approximately 10 cm and that the expansion joint in axis 10 consequently was about to close [16]. Due to these observations, both the expansion joint and the abutment was renewed the same year. In 1990 three core samples of the concrete showed that harmful alkali-silica reactions had occurred in the bridge. One year later, in 1991, vertical cracks in some of the columns were discovered during an inspection. ASR was assumed to be the cause, and new core samples revealed signs of the damaging reaction in all parts of the bridge, except the inner beams [16].

In 1995, the expansion joint needed to be renewed for the second time due to large expansions. From this time, more frequent inspections were performed to monitor the expansions of the bridge closely. During an inspection in 2000, it was measured that the bridge had expanded by 20 mm during the eight last years. In 2004 the expansion joint and the end support needed to be renewed again, for the third time. An inspection in 2013 showed an elongation of 10 mm since the mounting in 2004 [16]. However, the different elongations measured since 1951 have several uncertainties. Uncertainties are, e.g. the temperature during inspections and possible movements in the abutment.

In 2013 Aas-Jakobsen made a report after a special inspection of Elgeseter Bridge [16], written on behalf of The Norwegian Public Roads Administration. Data from earlier inspections were put together and summarized in charts. Figure 3.3a shows how the elongation has developed from 1951 to 2001. Points 1-4 are located along the end of the bridge in the expansion joint. The blue line represents the estimated elongation. From this chart, the bridge has extended by 140-180 mm during 50 years. This is equivalent to an average of 3.2 mm per year. The chart in Figure 3.3b shows the horizontal displacements of the column tops relative to their foundations, measured in 1991. Dark blue dots indicate measured values, while the other lines show linear estimates. It is seen that the displacement propagates through the bridge from the fixed end in axis 1 to the free end in axis 10. This chart gives an average elongation of 2.5 mm per year.

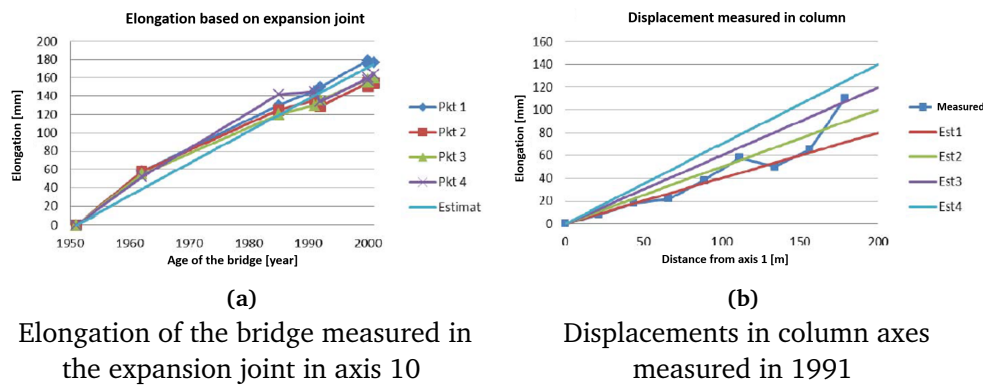


Figure 3.3: Expansion charts from Aas-Jakobsen's report in 2013 [16]

Elongation based on the measured displacements of the column tops may be the most accurate of the two. Measurements conducted in the end support in axis 10 depend on possible movements in the abutment, which can be a source of error. Temperature expansion is accounted for in both charts by knowing the temperature during the measurements. However, some uncertainties regarding temperature expansion are present.

In 2020 Aas-Jakobsen made another report regarding ASR in Elgeseter Bridge [17]. This report refers to a chart made by Trondheim county council, reproduced in Figure 3.4. The chart summarizes the longitudinal expansion based on measurements from all previous inspections and expected further development. The expansion seems to decrease as time goes on, flattening out to a total expansion of 200 mm. An expansion of 200 mm in the 200 m long bridge is equivalent to a strain of 1‰.

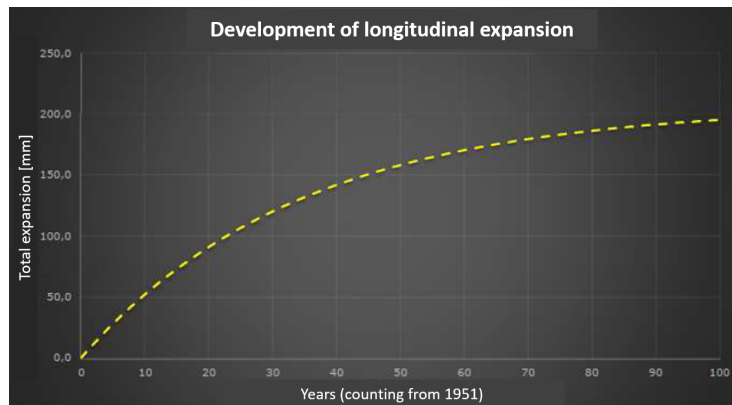


Figure 3.4: Chart illustrating measured and predicted longitudinal elongation, made by Trondheim county council [17]

Upper parts of the bridge are assumed to expand more than lower parts because of higher access to humidity. The picture in Figure 3.5, taken by Aas-Jakobsen in 2012, also shows clear signs of higher humidity in the outer parts of the bridge compared to the inner [16]. The pattern continued along the whole length of the bridge and was equal on both sides. The membrane, which was supposed to protect the concrete from water, was probably damaged in 1985 when the pavements on both sides of the bridge were extended. Due to the damaged membrane, water penetrated the concrete in the outer parts and consequently increased the ASR. The membrane was repaired in 2014 [18]. NPRA has assumed the varying expansions of the bridge, based on results from core samples, measured elongations and other observations regarding Elgeseter Bridge [19]. The resulting strain distribution represents a case where upper and outer parts expand the most. This will be further discussed in Section 6.4.2.



Figure 3.5: Moist concrete in plate between inner and outer beams [16]

3.2.1 Status of Columns

Since 1990 the columns of Elgeseter Bridge have shown signs of extensive cracks due to alkali-silica reactions. The most exposed columns are the ones located in the middle of the river, and the ones on the western side of the bridge [18]. The observed differences in the number of cracks are related to the water content at the surface of the columns. Columns standing in the river and generally on the western side are more exposed to cracking. This is due to higher exposure to water from the river, rainwater and sunlight. The importance of water content can also be seen by comparing the western and eastern side of the columns. Expansions in columns are quantified by calculating the Surface Crack Index (SCI). SCI is calculated by Equation (3.1) [18]:

$$SCI = \frac{\Sigma cw}{l} \quad (3.1)$$

where Σcw [mm] is the sum of the crack widths and l [m] is the length of the considered measuring line. During an inspection conducted by NPRA in 2014, the SCI was calculated separately for the western and eastern side of three columns in axis 4 [18]. The results are illustrated in Figure 3.6, and clearly show that the western side is more exposed than the eastern side (4A: 5.4 vs. 0.8 ‰, 4B: 2.4 vs. 1.0 ‰, 4D: 2.0 vs. 1.2 ‰). Figure 3.7 shows a 7 mm wide vertical crack in column 3A (west).

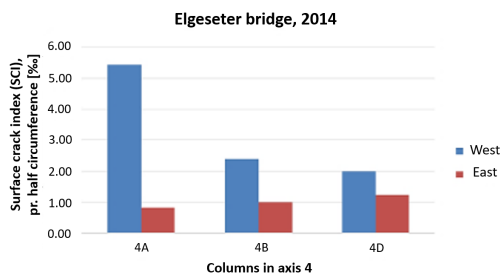


Figure 3.6: SCI compared for west and east side [18]



Figure 3.7: 7 mm crack width in column 3A [18]

Since the ASR monitoring started in 1990, several minor and more significant repairs have been made. In 1998 three crack-exposed columns were surface treated. Measurements 5 years later showed that some of the treated areas had a relative humidity below the ASR limit of 80%, which is desired [16]. In 2003 it was decided to correct the skew that had occurred in the columns due to the elongation of the bridge deck. In axis 7 and 8, the columns were corrected by cutting the

connection to the bridge and re-casting them in a straight position. Columns in axis 9 were corrected by moving the pinned connections [16]. Figure 3.8 shows a connection between a column and a beam in axis 9 after the repair. The column top was moved approximately 150 mm relative to the beam [18].

In 2003 two of the columns were used in an experiment using Carbon Fiber-Reinforcement (CFRP) to stop the ASR expansion, as shown in Figure 3.9. A report made in 2015 by NPRA concluded that even though the CFRP had reduced the crack growth, there was no need for CFRP on the columns [14]. The transverse expansions of the columns were too low for the CFRP to generate sufficiently large compressive forces to prevent further ASR expansions. The recommendation in the report was to keep monitoring the columns and take action if necessary. Capacity controls of the columns are not included in this task.



Figure 3.8: Column top in axis 9 after correction [18]



Figure 3.9: CFRP on columns A and B in axis 2 [18]

3.2.2 Status of Bridge Deck

ASR was confirmed in the bridge deck from core samples in 1991 [16]. However, no typical ASR crack patterns were observed from underneath the bridge. During rehabilitation work of the bridge deck in 2014, clear signs of ASR damages and delaminations were observed in the concrete under the asphalt layer. Areas exposed to delamination were chiselled and replaced by new and non-reactive concrete. The delaminations of the top of the bridge deck were probably caused by a combination of ASR and frost deterioration, which both have a positive correlation with the content of moisture in the concrete. [18]

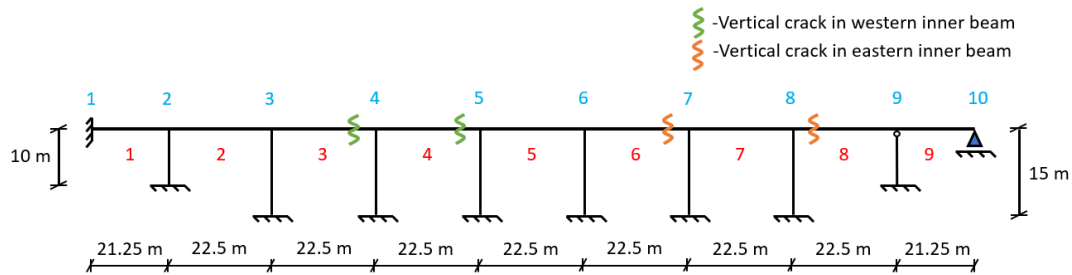


Figure 3.10:

Locations of large vertical cracks in beams illustrated in the static system

3.2.3 Status of Beams

An inspection in 2011 revealed wide cracks in the beams of Elgeseter Bridge [16]. These observations created concerns regarding the capacity of the superstructure and were the reason for Aas-Jakobsen's special report in 2013. During a new inspection, which took place in 2012, vertical cracks up to 6 mm were found in the inner beams, approximately 4.5 m from the columns several places along the bridge. The most prominent cracks in the western inner beam were located in span 3 close to axis 4, and in span 4 close to axis 5. The most significant cracks in the eastern inner beam were located in span 6 close to axis 7 and in span 8 close to axis 8. Locations of these cracks are illustrated in Figure 3.10. The large cracks were reported to be located alone and to be continuous through the whole cross-section of the beams. Two of the cracks are illustrated in Figure 3.11.

The location of the large cracks corresponds to the points of zero bending moment, approximately 4.5 m from supports. Cross-sections are here designed with small amounts of reinforcement, as the bending moment due to the self-weight here is zero. According to Aas-Jakobsen, only 3Ø32 is used as bottom reinforcement in some of these beam sections. For comparison, 20Ø32 are used in the midspans [16]. Expansions due to ASR moves the point of zero bending moment, and cross-sections designed with small amounts of reinforcement suddenly experience a considerable bending moment. The varying degree of ASR has generated compressive forces in outer beams and tensile forces in inner beams. The combination of low amount of reinforcement, the change in moment diagram and the additional tensile forces from ASR, might have caused a significant strain in the inner beams. The mechanical effects from ASR are explained in Chapter 6.

In 2014 some of the beams were reinforced with CFRP to try and stop the propagation of cracks. Different types of fibre reinforcement were used to increase both the bending capacity and the shear capacity. Since the CFRP is dependant on further expansion to contribute to the capacity, the effects are considered negligible. It is assumed that the ASR-expansions since 2014 and the mounted CFRP, not yet have affected each other. The capacity of beams have been thoroughly evaluated



Figure 3.11: Cracks in points of zero bending moment [16]

in reports by Aas-Jakobsen [17], and master's thesis by K. Stemland and K. Nordhaug [20], and by E. Christensen and S. Sande [21], and are therefore not further considered in this thesis.

3.2.4 ASR in Elgeseter Bridge in the Future

Elgeseter Bridge was designed to have a service life of 100 years and should therefore be able to stand for at least 30 more years. In 2019 the total elongation of Elgeseter Bridge was reported to be 180 mm, according to a report from NPRA [19]. A further expansion of the bridge can lead to crack growth, which can have fatal consequences for the capacity of the structure. Larger cracks lead to higher water intrusion in the concrete, increasing the risk of damage due to frost and corrosion on the reinforcement.

Researchers have so far not managed to determine whether alkali-silica reactions decay with time or not. As earlier mentioned, the ASR expansion may stop in restrained systems exposed to sufficiently large compressive stresses. Nevertheless, as long as all three components, *silica*, *alkalis* and *water*, illustrated in the triangle in Figure 2.1, are present, ASR-expansions must be assumed to continue [19].

However, the measured and predicted elongation of Elgeseter Bridge, illustrated in Figure 3.4, shows a clear reduction in expansion during the last years. Based on this chart, Aas-Jakobsen and Trondheim county council agreed that Aas-Jakobsen could use 200 mm as a total elongation in their calculation report in 2020 [17]. The same total elongation is used in this report.

Chapter 4

Guidelines and Materials

A well-established set of rules is necessary to ensure sufficient security and documentation in the building industry. In this chapter, the basis for the dimensioning is introduced. This includes relevant guidelines and material parameters.

4.1 Standards

The Eurocodes obtain a common understanding of security, documentation and rules regarding the construction of buildings [22]. The Eurocodes are standards describing structural design rules that are common for all European countries. Originally, these standards were tools to make it easier to cooperate across national borders and increase the overall security of buildings. The Eurocodes are not mandatory in all European countries, but many nations worldwide are using them. In Norway, the Eurocode has replaced the old National standards. Supplementary to the Eurocodes, each country has National Annexes (NA), which open for own rules and adjustments to the Eurocodes.

When Elgeseter Bridge was designed and built in 1951, the current guideline for reinforced concrete was NS 427, published in 1939. In 1973 a new guideline, NS 3473, was published. Through the following years, NS 3473 was updated and republished several times before it in 2010 was withdrawn and replaced by the Eurocodes.

When performing a bridge classification, it is common practice to use the version of NS 3473 used during the bridge design. The classification should therefore be conducted applying the first edition of NS 3473. Despite this, both Aas-Jakobsen's calculation report from 2020 [17] and K. Nordhaug and K. Stemland's master's thesis [20] have used the newest edition from 2003, NS 3473:2003 [23]. Therefore, in agreement with supervisor T. Kanstad, it is decided to do the same in this report. In addition, the current Eurocodes will be used as a supplementary.

Standards used in this report:

- NS 3473:2003, *Concrete structures - Design and detailing rules* [23]
- NS-EN 1991-1-1:2002, *Eurocode 1: Actions on structures* [24]
- NS-EN 1992-1-1:2004, *Eurocode 2: Design of concrete structures* [25]
- NS-EN 1995-1-5:2003, *Eurocode 1: General actions - Thermal actions* [26]

4.2 Handbooks

Handbooks from NPRA are guidelines containing both rules and guidance regarding the design of public roads. *Handbook N400: Bruprosjektering* covers the design of bridges and other load-bearing structures in the road network [27]. Handbook N400 applies to the whole service life of the structure. To assess the capacity of existing bridges *Handbook R412: Bruklassifisering* is used [28]. The term 'Bridge classification' means determining the maximum traffic load the bridge can resist, considering its drawings, material properties, earlier calculations and current condition.

Handbooks used in this report:

- N400 - *Bruprosjektering* [27]
- R412 - *Bruklassifisering* [28]

4.3 Material Properties

4.3.1 Concrete

Table 4.2-2 in Handbook R412 is used to determine the concrete strength in old bridges, depending on their year of construction [28]. The table relates the different concrete strengths in standards used through time in bridge design. According to the table, the concrete in bridges made after 1945 are characterized as class A in NS427, whereas in NS3473, it is characterized as C25. Handbook R412 specifies that a higher concrete strength than C25 can only be used if this is stated in the drawings of the structure. H. Johansen, on behalf of NPRA, has stated that C25 should be used in bridge classification of Elgeseter Bridge [19]. In NS 3473 [23], C25 means a characteristic cubic strength $f_{ck} = 25MPa$ and a structural strength $f_{cn} = 16.8MPa$ of the concrete.

The design compressive strength, f_{cd} , and the design tensile strength, f_{td} , are found by Equation (4.1). $\gamma_c = 1.40$ according to table 4 in NS 3473. Several other properties of the concrete are given in table 5 in NS 3473. Some of these, together with calculated design values, are summed up in Table 4.1.

$$f_{cd/td} = \frac{f_{cn/tn}}{\gamma_c} \quad (4.1)$$

In 2014, core samples were drilled out from Elgeseter Bridge and tested in a lab by SINTEF [29]. 6 samples were tested in a compression testing machine to examine the compressive strength of the concrete. The results gave a mean value of 36.8 MPa, with a standard deviation of 9.1 MPa. The characteristic cylindrical compression strength, f_{cckj} , is calculated to be 21.3 MPa using Equation (4.2), from section 16.5.1 in NS 3473 [23]:

$$R_k = R_m - w \cdot s \quad (4.2)$$

where R_k is the characteristic value of interest, R_m is the mean value, s is the standard deviation, and w is a constant from table 14 in NS 3473, found to be 1.7. Further on, section 11.1.2 in NS 3473 describes how to calculate the equivalent characteristic cylindrical compression strength, f_{cck} , from the above calculated f_{cckj} . Equation (4.3) result in $f_{cck} = 21.6MPa$, which is just above the compressive strength of the chosen C25 concrete. It is therefore reasonable to use C25 when considering the tests.

$$f_{cck} = 1.2 \cdot f_{cckj} - 4MPa \quad (4.3)$$

However, it is observed a relatively high standard deviation in the test results. From the mean value to the characteristic value, the compressive strength is reduced by 40% according to Equation (4.2). Therefore, the actual strength can in some places be as low as 60% of the mean value. This reduction is almost twice as large as in similar general tests. The variation in compressive strength might be explained by the ASR effects.

The short term Young's modulus is given in section 9.3.2 in NS 3473, here reproduced by Equation (4.4):

$$E_c = k_E \cdot (f_{cc})^{0.3} \quad (4.4)$$

f_{cc} is the cylindrical compression strength and $k_E = 9500(N/mm^2)^{0.7}$. The long-term Young's modulus is calculated by Equation (4.5):

$$E_{c,long} = \frac{E_{c,short}}{1 + \varphi} \quad (4.5)$$

where φ is the creep number. Due to the uncertainties regarding the determination of the creep number, it is decided to use a long-term Young's modulus $E_{c,long} = 10000MPa$. This value is also chosen by NPRA in their report regarding the conditions for the classification of Elgeseter Bridge [19]. This is equivalent to a creep number of $\varphi = 1.33$. Table 4.1 shows the material parameters for the C25 concrete used in the bridge deck and the beams.

Table 4.1: Material parameters concrete C25

Property	Sign	Value
Characteristic compressive cubic strength	f_{ck}	25 MPa
Characteristic compressive cylinder strength	f_{cck}	20 MPa
Characteristic structural compressive strength	f_{cn}	16.8 MPa
Characteristic tensile strength	f_{tk}	2.35 MPa
Characteristic structural tensile strength	f_{tn}	1.40 MPa
Yield strain	ϵ_{co}	2‰
Ultimate strain	ϵ_{cu}	3.5‰
Material factor	γ_c	1.4
Design compressive strength	f_{cd}	12 MPa
Design tensile strength	f_{td}	1 MPa
Young's modulus short-time	E_c	23300 MPa
Young's modulus long-time	$E_{c,long}$	10000 MPa
Poisson's ratio	ν	0.2
Thermal expansion coefficient	α	10^{-5} C^{-1}

4.3.2 Reinforcement

Elgeseter Bridge was designed using smooth steel bars with steel strengths St. 52 and St. 37. Lyse and Wiig illustrate work diagrams for the two steel types in their book "*Betong - uarmert og armert*" from 1957 [30], here shown as Figure 4.1. According to the diagram, the yield stresses for St. 37 and St. 52 are set to 230 MPa and 340 MPa, respectively. The yield stress for St. 37 is verified by table 4.2-3 in R412 [28]. Design values for the yield stresses are calculated as shown in Equation (4.6). The material factor γ_s is found in table 4.2-1 in R412, and set to be 1.25 in ULS.

$$f_{sd} = \frac{f_{sk}}{\gamma_s} \quad (4.6)$$

Worth noticing is also the failure strain of the materials, ϵ_{su} . According to the diagram, St. 37 have a failure strain of 13‰ while St. 52 has a failure strain of 10‰. The Young's modulus in the steel is set to $E_s = 200000$ MPa. Equation (4.7) gives an yield strain, ϵ_{sy} , of 1.15‰ for St. 37 and 1.7‰ for St. 52. Table 4.2 summaries the material properties for the reinforcement. Because the main longitudinal reinforcement and the transverse reinforcement are made of St. 52, this quality is used for all the reinforcement.

$$\epsilon_{sy} = \frac{f_{sd}}{E_{sd}} \quad (4.7)$$

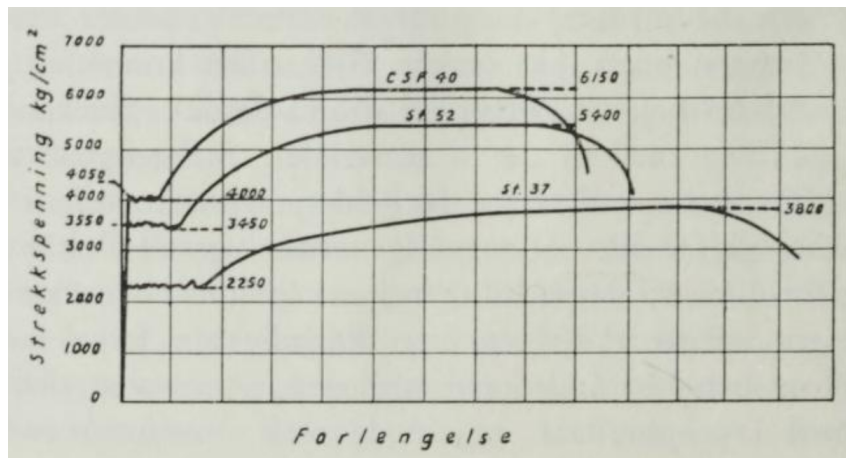


Figure 4.1: Work diagram for steel strengths [30]

Table 4.2: Material parameters St. 37 and St. 52

Property	Sign	St. 37	St. 52
Yield stress	f_{sk}	230 MPa	340 MPa
Material factor	γ_s	1.25	1.25
Design yield stress	f_{sd}	184 MPa	272 MPa
Young's modulus	E_s	200000 MPa	200000 MPa
Design Young's modulus	E_{sd}	160000 MPa	160000 MPa
Failure strain	ϵ_{su}	$\sim 10\text{‰}$	$\sim 10\text{‰}$
Yield strain	ϵ_{sy}	1.15‰	1.7‰

4.4 Cover

Different exposure classes are treated in section 15.2 in NS 3473 [23]. Since Elgeseter Bridge is exposed to splashes from the road containing chlorides, exposure class XD3 is chosen.

According to section 17.1.8 in NS 3473, the minimum cover needed for exposure class XD3 is 50 mm. It is here taken into account that Elgeseter Bridge has a service life of 100 years. Furthermore, the reinforcement is assumed not to be particularly sensitive to corrosion. A cover of 50 mm is chosen for the reinforcement in the beams.

The drawings of Elgeseter Bridge do not include any information regarding the cover in the plates, and consequently some uncertainties are related to this distance. Aas-Jakobsen has set the cover to 15 mm for the transverse reinforcement in their report from 2020 [17]. However, pictures of core samples from the bridge deck, presented by co-supervisor K. Stemland, indicate that the cover is at least

30 mm [31]. A cover equal to 33 mm was chosen in K. Stemland and K. Nordhaug's master's thesis, after scaling and measuring the drawings in Autocad [20]. After consultation with supervisors T. Kanstad and K. Stemland, it is decided to proceed with a cover of 33 mm for the transverse reinforcement in the plate. This corresponds to a cover of 49 mm for the longitudinal reinforcement, as the diameter of the transverse rebars is 16 mm. Choosing a cover of 33 mm instead of 15 mm is considered a conservative assumption because it reduces the height of the effective cross-section.

Chapter 5

Loads and Load Combinations

According to Handbook N400 [27], loads are categorized based on their duration in time. The four main categories are permanent loads, variable loads, deformation loads and accidental loads. This chapter explains how the different loads are included in the dimensioning of the bridge and how they are combined to determine the critical load cases. The resulting forces from the different loads in critical sections are presented in Chapter 9.

5.1 Permanent Loads

Permanent loads include the self-weight of the structure and permanent equipment, water pressure and soil pressure [27]. Only the permanent loads due to self-weight and super-self-weight are included in this thesis.

5.1.1 Self-weight

The self-weight of Elgeseter Bridge includes the bridge deck, the beams and the edge beams. The density of normal-reinforced concrete is 25 kN/m^3 [28]. Table 5.1 shows the pressure loads for elements in Figure 5.1. Loads are found by multiplying the thickness of the concrete layer with the density of concrete.

Self-weight from the edge beams are applied as line loads at the edge of element 1. The area of one edge beam is estimated to 0.235 m^2 , which gives a load equal to:

$$g_{edge_beam} = 0,235 \text{ m}^2 \cdot 25 \text{ kN/m}^3 = 5,86 \text{ kN/m}$$

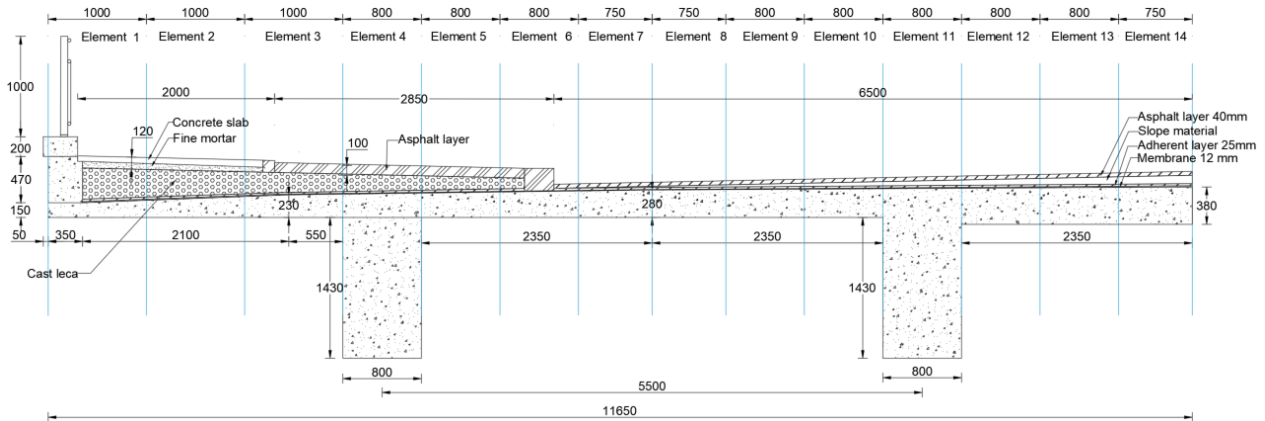


Figure 5.1: Cross-section of Elgeseter Bridge [mm]

Table 5.1: Elementwise self-weight

Element number	Thickness [mm]	Pressure load [kN/m^2]
1	158	3.95
2	194	4.85
3	228	5.70
4	1673	41.82
5	254	6.34
6	265	6.61
7	275	6.87
8	282	7.05
9	286	7.16
10	291	7.27
11	1725	43.13
12	369	9.24
13	374	9.34
14	378	9.45

5.1.2 Super-self-weight

The super-self-weight consists of the different layers in the bicycle- and pedestrian lanes, the wearing course and the railings. During the evaluation of Elgeseter Bridge conducted by Aas-Jakobsen in 2012, the wearing course was found to be almost 35 cm in the middle of the bridge, which results in a large additional load [16]. Consequently, the wearing course was removed and replaced by a new and thinner one in 2014. The new wearing course consists of a 12 mm membrane, a 25 mm adherent layer and a 40 mm thick asphalt layer. Original drawings showing the current wearing course are shown in Appendix A.

Thicknesses of different layers are included in the cross-section illustrated in Figure 5.1. The pressure loads applied on each element due to the super-self-weight are calculated by multiplying the densities, given in Table 5.2, with the height of the corresponding layer. Table 5.3 illustrates the calculated loads for each element. Handbook N400, section 5.2.2.2, states that bridges with a span length less than 50 m should be dimensioned with a minimum wearing course load of 3.5 kN/m^2 . This requirement is satisfied as the average super-self-weight is calculated to be larger than 3.5 kN/m^2 . The loads from the steel railings are implemented as line loads at the end of element 1, with a magnitude of 0.5 kN/m [28].

Table 5.2: Densities super-self-weight

Layer	Density [kN/m^3]
Membrane	25
Adherent layer	25
Asphalt layer	25
Slope material	25
Concrete slab	25
Cast leca	20

Table 5.3: Elementwise super-self-weight

Element number	Pressure load [kN/m^2]
1	9.53
2	8.93
3	9.90
4	6.43
5	5.83
6	3.35
7	2.13
8	2.37
9	2.63
10	2.89
11	3.15
12	3.41
13	3.68
14	3.93

5.2 Variable Loads

Variable loads are loads that vary in time and appear in periods. Variable loads include traffic loads, shock and anchoring loads from ferries, nature loads, and other short term loads. Other short term loads can e.g. be self-weight from equipment used during construction of the bridge or from components temporary placed on the bridge. [27]

Nature loads concern loads that originate from natural conditions like snow, wind and temperature. According to Handbook N400 [27], the snow load should not be considered to act simultaneously as the traffic load. It is assumed that a ploughed and snow-free road is needed for cars to drive on the bridge. Snow loads are therefore neglected in this thesis.

In agreement with supervisor T. Kanstad, it is decided that only the traffic load and the temperature load are relevant among the variable loads for this thesis, as the main focus is to evaluate the capacity of the plate between the beams. Wind loads and other minor variable loads are assumed to have minimal impact on the plates and are therefore neglected.

5.2.1 Traffic Load

Handbook R412 [28] defines how traffic load should be applied in existing bridges. Traffic load is defined as the vertical and horizontal loads from vehicles, cyclists and pedestrians on driving lanes, hard shoulders, bicycle lanes and sidewalks.

Bridges are assigned a bridge class (Bk), reflecting the traffic load allowed to pass the bridge without restrictions. The classification should correspond to the highest bridge class permitted based on the capacity of the weakest element. The capacity control is conducted using the partial factor method, which implies controlling that the dimensioning loads do not exceed the resisting capacity. Elgeseter Bridge is classified as a Bk 10/50 bridge [17].

Vertical loads:

Six load cases are listed to represent the different vehicles on a bridge. Figure 5.2, from Handbook R412 [28], shows the relationship between the load models and the bridge classes. The load models are applied in order to generate the most unfavourable load contributions. Handbook R412 gives rules for how the loads should be applied both in the longitudinal and the transverse direction. All traffic load cases should be considered separately to obtain the dimensioning load cases for the considered section. Dynamic effects are included in the load cases.

The magnitude of the loads representing the different vehicles are found in Figure

5.2, reproduced from R412 [28]. A is the axle load, V is the total weight, p is the additional lorry load, and H is the wheel load. The figure also depicts rules regarding how the loads should be applied in the longitudinal direction of the bridge.

Lasttype	Lastkonfigurasjon (*) H kN	Bruksklasser				
		Bk10	BkT8	Bk8	Bk6	
Hjullast		H	80	56	56	42
Aksellast		A	160	112	112	84
Boggilast		A ₁	65	40	40	30
		A ₂	160	112	112	84
		a	1,3	1,2	1,2	1,2
Trippelboggilast		A ₁	70	60	50	40
		A ₂	140	84	84	56
		a	1,3	1,2	1,2	1,2
Kjøretøylast		A	40	32	32	24
		V	300	280	220	180
Vogntoglast		A	40	32	32	24
		V	500	400	320	280
		p	6	6	6	6

Figure 5.2: Load cases and bridge classes [28]

Figure 5.3, also reproduced from R412 [28], illustrates the widths of the load fields in the transverse direction. The left-hand figure shows a typical heavy vehicle axle with a total width of $T = 3.0$ meters. The right-hand figure shows the width of an additional evenly distributed load applied in traffic lanes without heavy traffic. This load has a width of $t = 2.0$ meters and a magnitude of 6 kN/m .

Traffic loads should be placed unfavourable both in the transverse direction, within the carriageway, and in the longitudinal direction. The carriageway is the total width of where vehicles physically are allowed to drive. For Elgeseter Bridge, this is defined as the distance between the curbs on each side, measured to be 13 m.

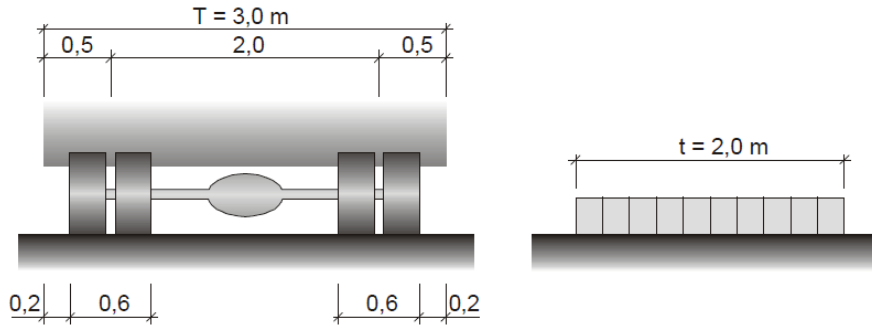


Figure 5.3: Width of load fields [28]

According to Handbook R412 [28], the decisive load case for small bridges and secondary constructions is typically obtained by axle loads, bogie loads or triple bogies. For the superstructure, often the vehicle or the lorry load is the decisive situation. The plate between the beams, which is the main focus of this thesis, can be considered a secondary construction. The bearing of the plate can be compared to a one-way slab supported by two beams. Simple tests have been performed in Abaqus, proving that the bogie loads are more unfavourable for the plate than the vehicle and the lorry load. Therefore, in agreement with supervisors T. Kanstad and H. Johansen, it is decided only to consider the axle load and the two bogie loads. Furthermore, it is observed that Aas-Jakobsen, in their report from 2020 [17], found the bogie loads to be critical for the plate during their capacity control in the transverse direction.

Traffic load can be applied in a maximum of two lanes simultaneously [28]. The dimensioning traffic load cases are found by testing in Abaqus, using the mentioned rules and guidelines. The modelling is discussed in more detail in Section 7.4.2.

How the pedestrian- and bicycle-lane should be loaded depends on how it is separated from the carriageway, its width and whether or not the traffic lanes are loaded. Section 3.2.5.2 in R412 [28] specifies the loads to apply when the pedestrian lane and the carriageway are separated with curbs, which is the case for Elgeseter Bridge. An evenly distributed load of $2kN/m^2$ should be applied on the pedestrian lane if traffic loads are included. If no traffic load is applied, the evenly distributed load should be $4kN/m^2$. It is assumed that the evenly distributed load has a minimal impact on the inner plates as it acts on both sides of the beams and the low intensity. The pedestrian load is therefore neglected.

Horizontal loads:

Horizontal forces occur as vehicles accelerate, both by braking and by increasing the speed. Handbook R412 [28] separates horizontal loads into braking load, transverse load and centrifugal load. None of these loads can appear without the vertical loads.

The braking load originates from the braking of a vehicle and depends on the length of the bridge. According to R412 [28], a braking load equal to 300 kN should be applied, as the bridge length is larger than 40 m. The transverse load accounts for skew or unsymmetrical braking and has a magnitude of 25% of the braking load. However, it is decided to neglect both the braking load and the transverse load. Elgeseter Bridge is located close to the city centre with traffic lights close to both ends. Vehicles will be forced to drive at a relatively low speed, which leads to a low braking load. In addition, braking loads will primarily affect the dimensioning of the columns supporting the bridge in the horizontal direction. Horizontal forces are assumed to be absorbed by the abutment in the south end.

The centrifugal load appears in bridges built with a horizontal curvature, as vehicles need a lateral acceleration to turn. This acceleration of the vehicle is obtained through a centripetal force acting towards the centre of the turning radius. The counterforce pushes the bridge deck in the opposite direction, generating a horizontal load in the transverse direction. Handbook R412 [28] states that the centrifugal force only appears if the turning radius $R < 1500$ meters. Because Elgeseter Bridge is a straight bridge, which means $R \approx \infty$ the centrifugal load will not be an issue. None of the horizontal traffic loads are therefore included in this thesis.

5.2.2 Temperature Load

The volume of concrete varies due to different temperatures. An increased temperature leads to expansion of the concrete, while a reduction in temperature leads to a volume reduction of the concrete. The combination of the change in volume and a static indeterminate system generates restraining forces in the structure. Boundary conditions prevent the structure from expanding. Eurocode 1: NS-EN 1991-1-5 [26], hereby referred to as EC1-1-5, states how temperature changes should be included. The thermal load impact is determined from two contributions; an evenly distributed temperature field and a vertically varying temperature.

The evenly distributed temperature fields originate from the variation in temperature during a year. Temperature differences between summer and winter cause a uniform and equal volume change through the whole bridge. A uniform shrink-

age counteracts the elongation from ASR and reduces the bending moments in the beams. Consequently, it has a beneficial contribution and can therefore be conservatively neglected. A temperature-caused elongation, on the other hand, has an unfavourable contribution. The column tops will follow as the superstructure elongates and transfer bending moments to the beams through their rigid connections. However, the columns are flexible compared to the greater and stiffer beams. The transferred bending moments from the columns are therefore considered to be marginal, and it seems like a reasonable simplification to neglect them. Low column stiffness also provides small restraint axial forces in the superstructure. It is even disputed whether or not it is correct to include the temperature loads together with ASR. This is further discussed in Chapter 11. Evenly distributed temperature loads are neglected in this study.

Vertically varying temperature loads include the diurnal variation. Short term temperature variations between day and night give a linearly, alternatively non-linearly, varying temperature field through the cross-section. The actual temperature gradients can vary in all directions, giving curvatures and bending moments in several ways. However, according to EC1-1-5 [26], it is common only to consider a vertical variation. Horizontal variation appears if one side of the bridge is more prone to e.g. sunlight than the other. The non-linear temperature variation, which opens for extreme cooling or heating cases, is neglected in this study. This simplification seems reasonable considering the temperate and stable climate in Trondheim. Thus, only the linear vertically varying temperature field, described as *Method 1* in EC1-1-5, is considered in this thesis.

Vertically varying temperatures:

Variation of temperature is included through two temperature gradients, $\Delta T_{M,heat,0}$ and $\Delta T_{M,cool,0}$. The gradients are given in table NA.6.1 in EC1-1-5 [26], and represent the cases where the upper bridge deck is heated and cooled, respectively. Elgeseter Bridge is classified as a *type 3* bridge because of its composition of concrete beams. The gradients are then found to be:

$$\Delta T_{M,heat,0} = 15^{\circ}C$$

$$\Delta T_{M,cool,0} = 8^{\circ}C$$

These temperature gradients apply for bridges with a 50 mm thick asphalt layer. From Figure 5.1, the total thickness of the wearing layer in Elgeseter Bridge, including the asphalt layer, the adherent layer and the membrane, is set to be 77 mm. A reduction factor k_{sur} , found in table NA.6.2 in EC1-1-5 [26], accounts for the different asphalt layer thickness. k_{sur} is found by interpolating between values given for thicknesses of 50 mm and 100 mm, and are found to be 0.838 for $\Delta T_{M,heat,0}$ and 1.0 for $\Delta T_{M,cool,0}$. The resulting gradients are calculated to be:

$$\Delta T_{M,heat} = k_{sur,heat} \cdot \Delta T_{M,heat,0} = 12.6^{\circ}C$$

$$\Delta T_{M,cool} = k_{sur,cool} \cdot \Delta T_{M,cool,0} = 8^{\circ}C$$

The uniform and the vertically varying temperature loads are usually combined through eight equations given in section 6.1.5 in EC1-1-5 [26]. Because the uniformly distributed temperature load is neglected, only the two cases where the bridge deck is either heated or cooled become relevant. The two load factors reducing the temperature loads, ω_N and ω_M , are not included since only one case occurs at a time.

5.3 Deformation Loads

According to N400 [27], deformation loads are related to applied deformations or the structure's material properties. These loads include prestressing forces, shrinkage, creep, relaxation, settlements and deformations from loads applied to the structure. Only creep and shrinkage are relevant in this study since Elgeseter Bridge is a non-prestressed bridge.

5.3.1 Creep

Concrete exposed to compression over a long period of time will continue to be compressed beyond the instantaneous contraction occurring when the load is applied [1]. This phenomenon is called creep. The creep strain is dependent on the size of the load in addition to the load duration. According to NS3473 [23] section 9.3.2, the creep strain is assumed to be proportional to the concrete stress and can be expressed by the following equation:

$$\varepsilon_{cc} = \varphi \cdot \varepsilon_c = \varphi \cdot \frac{\sigma_c}{E_{ck}} \quad (5.1)$$

where φ is the creep number, σ_c is the stress in the concrete due to long-term load and E_{ck} is the short-term Young's modulus.

As mentioned in Section 4.3.1, a long-term Young's modulus equal to 10000 MPa is used in this thesis, which corresponds to $\varphi = 1.33$. The effects of creep are accounted for by using the long-term Young's modulus for long-term loads consisting of the self-weight and the ASR load.

5.3.2 Shrinkage

Shrinkage is a result of dehydration of the concrete. In contrast to the creep strain, the strain due to shrinkage is independent of the magnitude and duration of the load. The total shrinkage strain consists of two contributions, dehydration shrinkage and autogenous shrinkage [1].

The dehydration shrinkage develops slowly and is a function of moisture in the hardened concrete. In comparison, the autogenous shrinkage is a linear function of the concrete strength. Consequently, most autogenous shrinkage develops in an early stage after casting [1].

Elgeseter Bridge is located in a moist environment. Hence, the dehydration shrinkage is not calculated in this thesis. Furthermore, the strain due to shrinkage will have the opposite effect as the ASR strains. Because the shrinkage will reduce the ASR effects, it is considered conservative to not include the shrinkage in the calculations.

5.4 Accidental Loads

Accidental loads occur due to incorrect operation, accidents, or abnormal events. The latter includes impact loads from vehicles, ships or rail traffic, loads from falling objects, fire with the following explosion, explosion with the subsequent fire, and loads caused by avalanche and flood. [27]

Occurrence and consequences due to accidental loads can be related to a given risk level. Accidental loads can be excluded from the analysis as long as the probability of events is below 10^{-4} each year [27].

5.5 Load Combinations ULS

Load combinations for existing bridges are treated in Handbook R412 [28] appendix 1, section 3.3. A minimum requirement when performing bridge classification is a capacity control in the ultimate limit state (ULS). Two different load combination sets should be controlled with load factors described in Table 5.4. Dimensioning forces are found for each section in the bridge by combining the characteristic loads with the current load factors.

Table 5.4: Load factors for ULS according to Handbook R412 [28]

Combination	Permanent loads, P	Deformation loads, D	Variable loads, Q
a	1.15	γ_d	$\gamma_1 \cdot Q_1$
b	1.0	1.0	$\gamma_2 \cdot Q_1 + 0.8 \cdot \sum Q_n$

where:

$$\begin{aligned}\gamma_1 &= 1.4 && \text{Traffic in one lane} \\ &= 1.3 && \text{Traffic in two lanes} \\ &= 1.0 && \text{Temperature load} \\ &= 1.6 && \text{Other variable loads}\end{aligned}$$

$$\begin{aligned}\gamma_2 &= 1.2 && \text{Traffic load} \\ &= 0.8 && \text{Temperature load} \\ &= 1.3 && \text{Other variable loads}\end{aligned}$$

$$\gamma_d = 1.0$$

$$\begin{aligned}Q_1 &= \text{Characteristic value for the most unfavorable variable load considered} \\ Q_n &= \text{Characteristic value for other unfavorable variable loads}\end{aligned}$$

Only the ULS will be controlled in this thesis. The ASR load will have a load factor equal to 1.0 for both load combinations. The load combination factors for ULS are shown in Table 5.5.

Table 5.5: Load combination factors in ULS

Combination	G	ASR	TR	TE
ULSa-TR	1.15	1.0	1.3*	0
ULSa-TE	1.15	1.0	0	1.0
ULSb-TR	1.0	1.0	1.2	0.8
ULSb-TE	1.0	1.0	0.8	0.8

* 1.4 if traffic in only one lane.

where the symbols represent the following:

G	Self-weight
ASR	ASR load
TR	Traffic load
TE	Temperature load

Chapter 6

Loads from Alkali-Silica Reactions

The concrete expansion due to ASR is considered a long-term effect and will lead to forces in the structure in addition to other forces such as permanent loads, traffic loads and live loads. The forces caused by ASR can be of significant size, and it can take many years for the forces to develop. Thus, it is essential to take these forces into account in the models for capacity calculations.

The loads from ASR are dependent on the expansion and how the expansion is distributed over the cross-section. Furthermore, the amount and distribution of reinforcement and the external restraints also affect the loads. Structures that are not restrained will get an internal load effect due to the expansion caused by ASR, while structures that are restrained can get external forces and moments. The different load effects and models to account for the expansion due to ASR will be further explained in this chapter.

6.1 Internal Load-effects

When a reinforced concrete structure get exposed to ASR, only the concrete will expand. The bond stresses between the reinforcement and the concrete lead to a tensile force in the reinforcement, which will try to resist the concrete's expansion. Consequently, due to the requirement of equilibrium, this will give a compressive force in the concrete. Therefore, the expansion will result in an internal force system that will change the reinforcement- and concrete stresses.

Figure 6.1 illustrates the principle of internal restraints in a reinforced concrete beam. If the beam is without reinforcement, it can expand freely, and there will not occur any internal stresses in the concrete. Therefore, the tensile stresses in the concrete due to free expansion is neglected. This is illustrated with the red

dashed lines. To understand the contribution from the reinforcement, the concrete and the reinforcement can first be treated as independent parts. The next step is to give the reinforcement the same expansion as the concrete and then attach them. The tensile force in the reinforcement will then be applied to the concrete as a compression force, which will reduce the free expansion of the concrete. In the final strain situation, illustrated with the blue dashed lines, the compression force in the concrete is the same as the tensile force in the reinforcement.

When the reinforcement is treated in this way, it is possible to understand the cross-section's different strain contributions better. The stress contributing strain in the concrete is the difference between the final strain (blue lines) and the initial strain caused by the free expansion (red lines). In contrast, the stress contributing strain in the reinforcement corresponds to the final strain situation (blue lines).

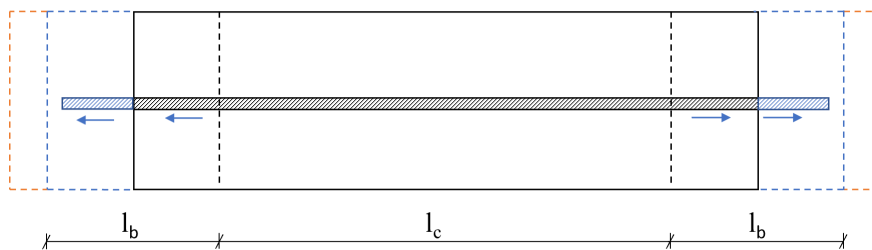


Figure 6.1: Expansion of a beam with reinforcement placed in center of gravity

The stress in the reinforcement increases over an anchorage length, l_b , through bond stresses. This means that the bond between the reinforcement and the concrete is not fully achieved in this area, and the reinforcement will therefore slip a little near the ends of the beam, which is illustrated in Figure 6.1. Over the length, l_c , the bond between the reinforcement and the concrete is fully obtained, and compatibility between the two components is achieved. The effects in the anchorage areas will not be included in this report because the error of such a simplification is assumed to be relatively small in a large structure with a lot of continuous reinforcement [5].

Internal stresses due to ASR will only occur as long as the material behaviour is linear elastic. Since the ultimate moment capacity is calculated when the reinforcement is yielding, the initial strain due to ASR will have a minor impact on the capacity. Thus, the stresses from the expansion can be considered as an internal pre-tension effect. However, the state of the cross-section has a significant impact on the response due to the expansion. This will vary within the structure as a result of different external loads and various degree of expansion. Significant parts of the structure will be in stage II during the expansion due to simultaneously acting loads such as dead-load and live loads. Stage II means that the area of the cross-section has cracked. The concrete's cracked area has zero tensile capacity, and the reinforcement takes all the tensile forces. A typical assumption for

a structure exposed to dead load and different live loads is to assume that the areas in the mid-spans and over the supports are in stage II, and areas close to the zero-moments are in stage I. However, this may be a rough assumption because areas are often somewhere between stage I and stage II [5]. In this thesis, only the stage I-stiffness will be considered in the analysis of the bridge.

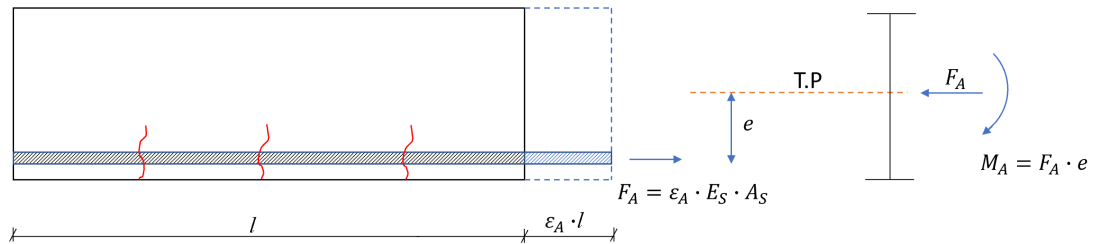


Figure 6.2: Loads from ASR on reinforced concrete

When the reinforcement is eccentrically placed, the reinforcement will give a moment in addition to the axial force in the cross-section. This is illustrated in Figure 6.2. Common practice is to relate the force to the centre of gravity, T.P. of the cross-section in stage I [5]. Reinforced concrete elements often have more tensile reinforcement than compression reinforcement. For a mid-span section, this will result in a bending moment in the cross-section due to ASR, illustrated as M_A in Figure 6.2. The rearranging of internal forces will not result in external load contributions for a static determined structure.

If the bending moment from ASR is larger than the bending moment from the self-weight, the cross-section tends to curve upwards. In general, the expansion due to ASR will increase the compressive force in the concrete and increase the tensile force in the reinforcement. However, the reinforcement in the compression zone may change to a tensile state if the expansion due to ASR is sufficiently large. Therefore, it is essential to carefully consider the different strain contributions in both the tensile- and the compressive reinforcement.

6.2 External Load-effects

When a structure is fixed against rotation or elongation, it will get an external restraint. If external restraints prevent the expansion due to ASR, additional load contributions in the structure will occur.

A statically determined beam exposed to a higher expansion in the upper part will curve upwards, and no external moments will be present in the beam. For a continuous beam supported by columns, the curvature will be prevented by the columns resulting in a restraining moment in the beam, as shown in Figure 6.3.

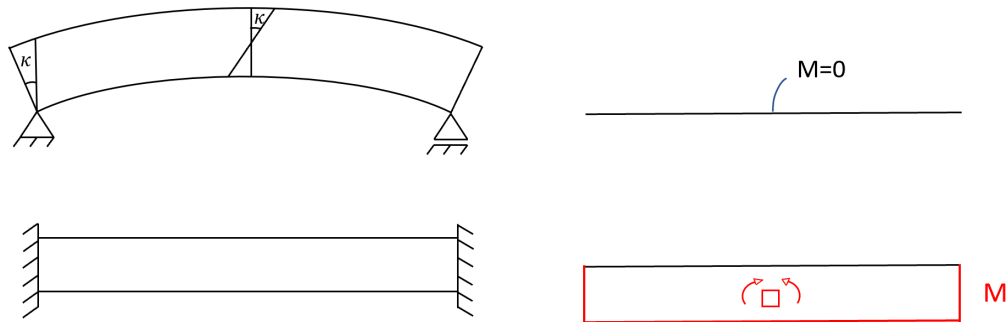


Figure 6.3: Beam with more expansion in the upper part

Elgeseter Bridge is constructed with a fixed support at the south side and an expansion joint at the north side, axis 1 and 10, respectively in Figure 3.2. Thus, the expansion in the bridge will increase towards the city side. Consequently, the displacement in the top of the columns closest to this side can be significantly large. Furthermore, all the column rows except the row closest to the city (axis 9) are monolithically connected to the beams. Therefore, the expansion due to ASR in the bridge will result in moments in the columns, which will distribute linearly in the beams, as illustrated in Figure 6.4.

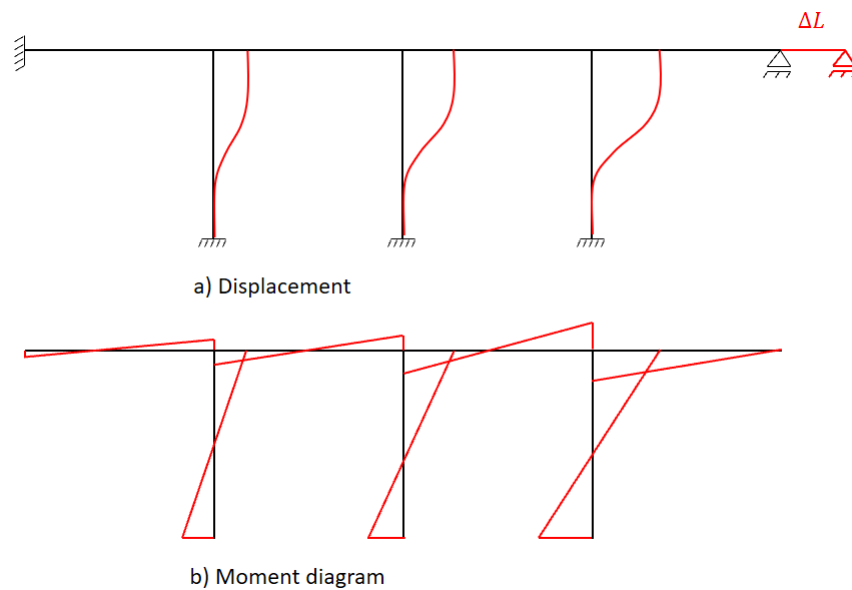


Figure 6.4: Structure with columns monolithically connected to expanding beams

A continuous beam/slab-bridge can often expand almost freely in the longitudinal direction because of the small resistance from the columns, given that one of the end supports have an expansion joint. This will result in a relatively small axial force in the beams from the columns, which can often be neglected in this type of

structures [5]. Typically the expansion joint is only designed for expansion caused by temperature. If the expansion due to ASR is large enough, the expansion joint gap may be closed, resulting in compressive forces in adjacent structural members such as the abutment. The static system can change, and this must be taken into account in the capacity calculations.

The expansion due to ASR can vary locally in the structure due to different exposure to humidity. This can result in external restraints from adjoining parts. For example, Figure 6.5 shows two adjoining beams, where beam A is exposed to an initial strain ε_0 . If both beams were exposed to the same initial strain, no external forces would occur. However, the initial strain in beam A will force beam B to follow due to compatibility criteria between the beams. Thus, beam B will get a tensile force, N_B , from the adjoining beam's expansion. Moreover, beam B will resist the expansion, resulting in a compression force N_A in beam A.

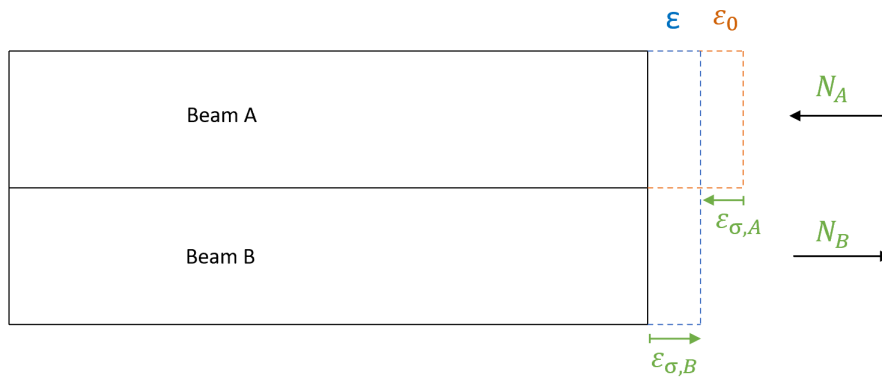


Figure 6.5: External restraint from adjoining parts

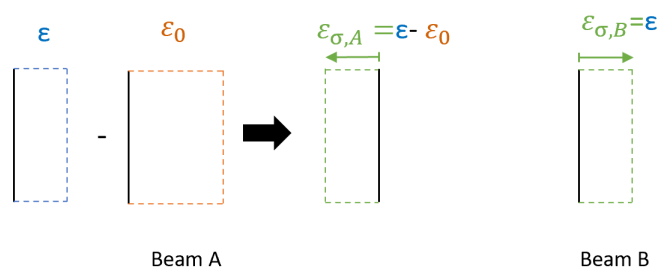


Figure 6.6: Different strain contributions in Beam A and Beam B

An important aspect is the difference between the final strain, ε , and the stress contributing strain ε_σ , illustrated in Figure 6.5. The final strain is the structure's resulting strain state, whereas the stress contributing strain gives stresses in the structure. These strains arise because of the restraining forces between the ele-

ments due to compatibility. The stress contributing strain is an imaginary strain state, and to be able to get this strain, the initial strain must be subtracted from the final strain as follow:

$$\varepsilon_{\sigma} = \varepsilon - \varepsilon_0 \quad (6.1)$$

An external restrained structure exposed to a uniform expansion due to ASR will get a constant pressure over the height, as shown in Figure 6.7.1, given that the cross-section is in stage I. On the other hand, for a beam in stage II, most of the compressive force will be taken through the compression zone over the supports, as illustrated in Figure 6.7.2. If the expansion is sufficiently large, the compressive force might start to close the cracks in the lower part, resulting in stress distributions as shown in Figure 6.7.2 and Figure 6.7.3. Therefore, a section in stage II may get back to a stage I situation, depending on the load-combination and expansion degree. This will lead to an increase in axial and bending stiffness.

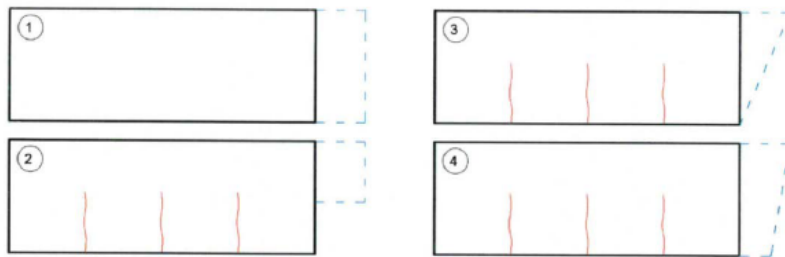


Figure 6.7: Force distribution for a restrained beam depending on the degree of cracks and expansion [5]

The expansion due to ASR in a continuous beam will generally increase field moments and reduce the support moments from the external loads. It will also shift the areas with zero moments in the structure, as illustrated in Figure 6.8. The amount of longitudinal reinforcement reflects the size of the moment in a section. Many existing structures are not designed for additional bending moments due to ASR, which is also the case for Elgeseter Bridge. Thus, areas designed for zero bending moment have a small amount of reinforcement, often smaller than the corresponding minimum reinforcement of today's structures. Consequently, significantly moments can appear in sections that are not designed for such loads. These sections can become very critical in a structure. The elastic moment capacity can be exceeded, resulting in the formation of plastic hinges. This can change the static system, leading to exceedance of the moment capacity in other sections.

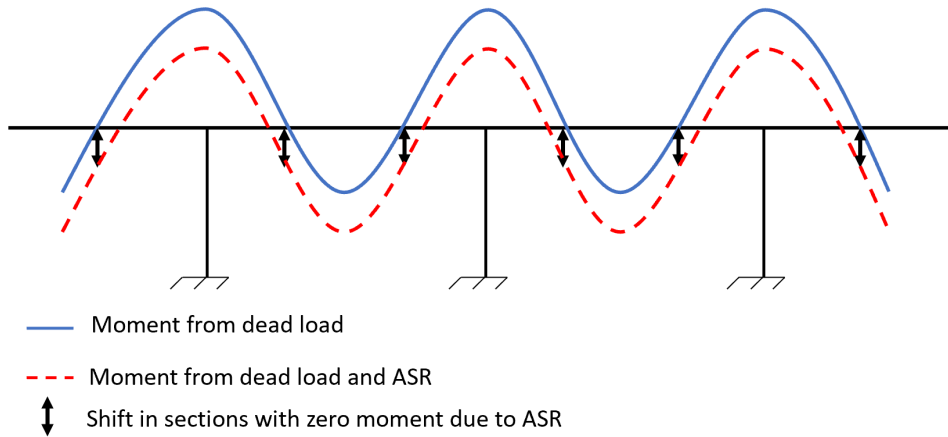


Figure 6.8: Shift in moment distribution due to ASR

6.3 Calculation Models Accounting for ASR

The expansion due to ASR can vary locally in the cross-section and the longitudinal direction of the bridge. The Norwegian Public Road Administration published in 2016 "Alkali-Silica Reactions - Guidance for structural analysis" [5], which describes how the expansion due to ASR can be included in the structural analysis. Three different models were suggested:

- Model 1: Beam or slab with a uniform or linear expansion over the height of the cross-section
- Model 2: Beam or slab with a higher expansion in one part of the structure than the other (such as a T-beam with a higher expansion in the flange than in the web)
- Model 3: Slab or T-beam with different expansion over the width of the cross-section

When describing the expansion due to ASR, one model can be used, or a combination of several models, if the variation of expansion in the structure is more complex. Since ASR is a process that extends over a long time period, the long-term Young's modulus of concrete needs to be used in the calculations. A common factor for all the load models is the stage of the concrete. Therefore it is essential to consider if the concrete can take tensile stresses (stage I) or if the concrete is cracked such that only the compression zone of the concrete can transfer stresses (stage II). This is a complex issue since the ASR effects can transform the concrete from a stage II state back to a stage I state. The stage II state will also only occur in the section where the crack is located. At both sides of the crack, the concrete will be in a stage I state.

6.3.1 Load Model 1

This model is used when the expansion is either constant or linear over the cross-section and is based on the theory presented in Section 6.1. Figure 6.9 a) shows the cross-section of a T-beam exposed to a constant expansion. The amount of reinforcement is larger in the lower part, which results in different tensile forces in the reinforcement, as illustrated in Figure 6.9 b). These forces generate compressive forces in the concrete and are treated as a compressive force and an additional moment about the axis of gravity, $T.P.$, as shown in Figure 6.9 d). The moment is given as:

$$M_1 = F_s \cdot e_s - F'_s \cdot e'_s$$

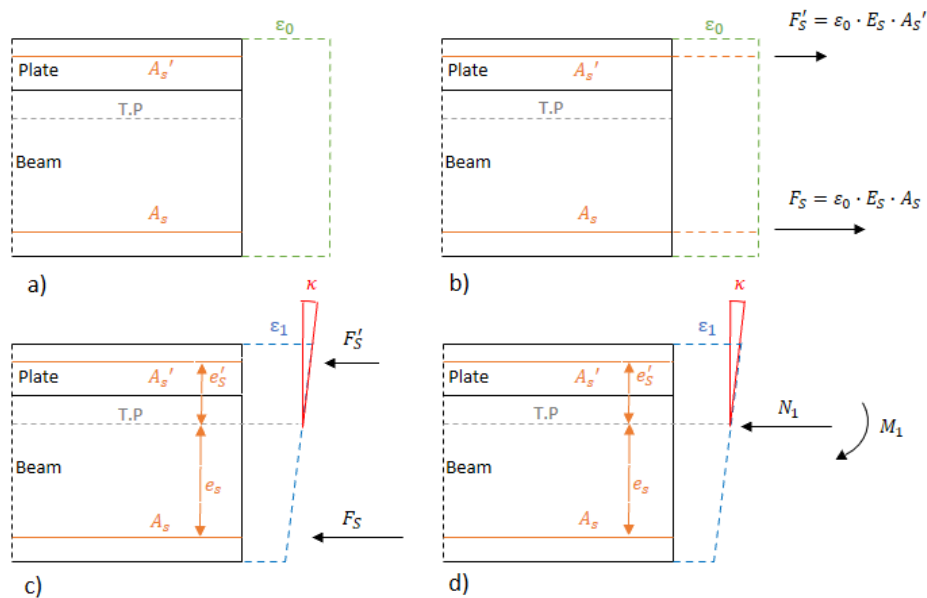


Figure 6.9: Internal load effects for load model 1

To find the loads from ASR due to external restraints, the uniform expansion in the axis of gravity, $T.P.$, is inserted as a temperature load in the analysis, in addition to the temperature gradient corresponding to the curvature, κ , of the section.

6.3.2 Load Model 2

The bridge deck is often more exposed to moisture than the beams, resulting in expansion due to ASR only in some parts of the cross-section. Load model 2 is described for a T-beam where only the plate is given an expansion, as illustrated in Figure 6.10 a). To determine the loads from this model, the expansion in the plate is first restrained with force, F_{c2} , such that the cross-section does not get any stresses, as shown in Figure 6.10 b). The same force is then applied to the

reinforced cross-section as an equivalent tensile force, as shown in Figure 6.10 c). Thus, this force can be treated as a tensile force, N_2 , and a moment, M_2 , about the axis of gravity, $T.P$, as shown in Figure 6.10 d). The moment will give an upward curvature of the cross-section.

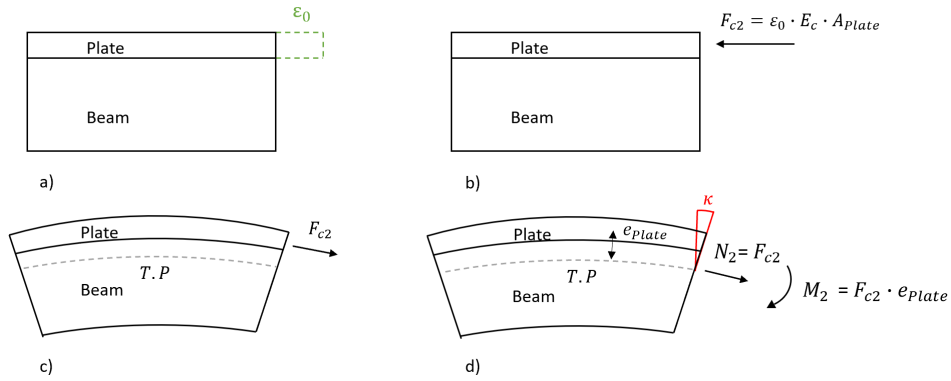


Figure 6.10: Internal load effects for load model 2

The loads from ASR might result in tension in the whole cross-section, also in combination with external loads. However, this is only an imaginary state used to determine the final strain state of the cross-section. The stress contributing strain in the reinforcement is equivalent to the final strain. In contrast, the stress contributing strain for the plate is found by subtracting the initial strain from the final strain, resulting in compression for the plate.

There are many uncertainties regarding which force can be established for a restrained and cracked plate. Therefore, this model is best suited for a situation where the plate is in compression due to a dead-load, typically for a section in the span. The compression force in the plate due to ASR will then increase the compression zone in the cross-section [5].

6.3.3 Load Model 3

Load model 3 is based on the same principles as load model 1 and 2. The difference is that load model 3 is used to calculate the load effects due to different expansion over the width of the cross-section, while load model 1 and 2 is used when the expansion varies over the height of the cross-section. Typically the outer beams will be more exposed to humidity than the inner beams. This will result in an additional expansion in the outer beams compared to the inner beams. The inner beam will try to prevent the outer beam from expanding, resulting in a compressive force in the outer beam and a tensile force in the inner beam. This case is described in Figure 6.5 where the expansion varies in the width of the cross-section. Beam A and beam B correspond to the outer beam and inner beam, respectively.

Load model 3 results in both axial forces, shear forces and moments in the plate. The shear forces distribute in the plane of the plate, whereas moments can arise both about the vertical axis in the centre line and as torsional moments in the plane of the plate [5].

When evaluating the expansion over the cross-section's width, the principles based on load model 2 can only be used when one part of the cross-section is expanding. In contrast, load model 1 should be used if the expansion is varying linearly over the cross-section's width [5]. Load model 3 is best suited to determine the average axial strain in the longitudinal direction, given that the beams are prevented from rotating about the vertical axis. When both the outer beams are expanding equally, this would be the case due to symmetry. However, the situation becomes more complex when the reinforcement's contributions are accounted for due to the variation in reinforcement along the bridge. Consequently, the beams and the plate will get rotation about both axes, in addition to the axial displacement.

6.4 ASR Loads in the Longitudinal Direction

Aas-Jakobsen carried out a detailed report of Elgeseter Bridge in 2020, where the state of the bridge was considered, especially concerning ASR. A stage I-stiffness in addition to a reduced stiffness (stage II) in critical areas along the bridge were evaluated. The calculations are based on a linear elastic analysis, and the bridge was modelled using a frame model. The ASR loads were considered as equivalent temperature loads, where the contributions from the reinforcement were included in these loads [17].

In order to find the corresponding temperature loads from ASR, several parameters need to be considered. The free expansion of the concrete, the amount of reinforcement in the cross-section, and the stage of the concrete will affect the magnitude of the loads.

In this thesis, the loads from Aas-Jakobsen corresponding to the stage I analysis are used to evaluate the response due to ASR in the longitudinal direction.

6.4.1 Geometry used by Aas-Jakobsen

The outer- and inner beams have a height of 1675mm and 1740mm, respectively. The bridge plate has a thickness varying from 150mm in the free end to 380mm between the inner beams. The simplification of the cross-section is modelled as shown in Figure 6.11. The edge beams contribute to increased stiffness. Therefore, it is reasonable to model the outer beams with a thickness of 280mm. The different layers of reinforcement in the upper part, A_{s0} , and the lower part, A_{su} , are placed

in their centre of gravity. Moreover, the axis of gravity, *T.P.B.*, is calculated for an unreinforced concrete section in stage I [17].

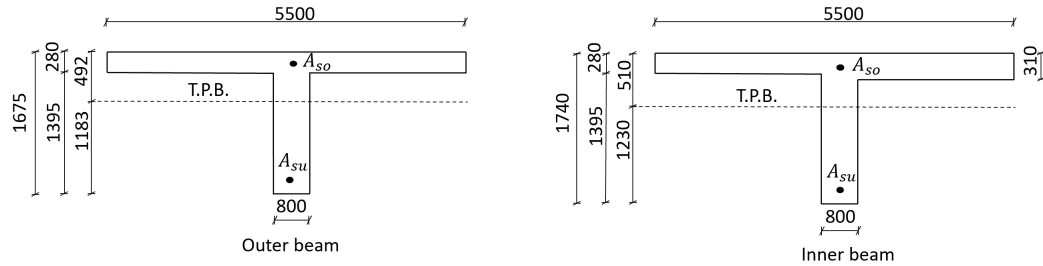


Figure 6.11: Cross-section used by Aas-Jakobsen to determine the ASR loads [mm]

When the reinforcement's resistance due to ASR expansion is calculated, all the longitudinal reinforcement in the plate are included. Some parts of the longitudinal reinforcement are bent upwards in the areas around the columns to act as shear reinforcement. This reinforcement has horizontal anchorage length, which is not included in the ASR-calculations nor the capacity controls [17].

Aas-Jakobsen used an element length equal to 1.25 meter in the analysis. This length corresponds well to the bridge's span width, resulting in 17 elements for the two outer spans and 18 elements for the internal spans. Consequently, the same element lengths are used in this thesis.

6.4.2 Free Expansion

As mentioned in Section 3.2, it is observed a higher expansion due to ASR in the upper part of the bridge in addition to the outer beams compared to the inner beams. Furthermore, the variation of ASR is assumed to be small in the longitudinal direction. The Norwegian Road Administration suggested a distribution of the strain due to free expansion in their report of Elgeseter Bridge [19], which is shown in Figure 6.12. The strain distribution corresponds to load model 1 due to the linear variation of strain over the cross-section height. Furthermore, the expansion is more prominent in the outer beams, resulting in the load effects explained for load model 3.

The size of the free strain, a , is chosen such that the total expansion of the bridge due to ASR is 200 mm. An important aspect is that the total expansion corresponds to the expansion in the cross-section axis of gravity. The reinforcement will prevent some of the free expansion. Therefore a higher value of the free expansion is required, compared to a situation without reinforcement. The ASR loads from Aas-Jakobsen is calculated using a free strain, $a = 0.52\text{‰}$ to achieve a total displacement of 200 mm.

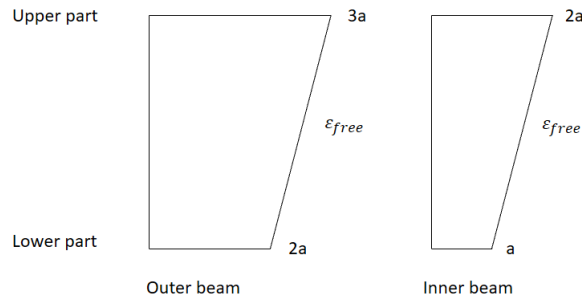


Figure 6.12: Assumed free strain

6.4.3 ASR Loads from Aas-Jakobsen

The axial strain and curvature due to ASR are larger for the outer beam, as illustrated in Figure 6.13 and Figure 6.14. As a result of different amounts of reinforcement along the bridge, the resulting strains from ASR loads will also vary in the longitudinal direction. The outer- and inner beam corresponds to the cross-sections shown in Figure 6.11.

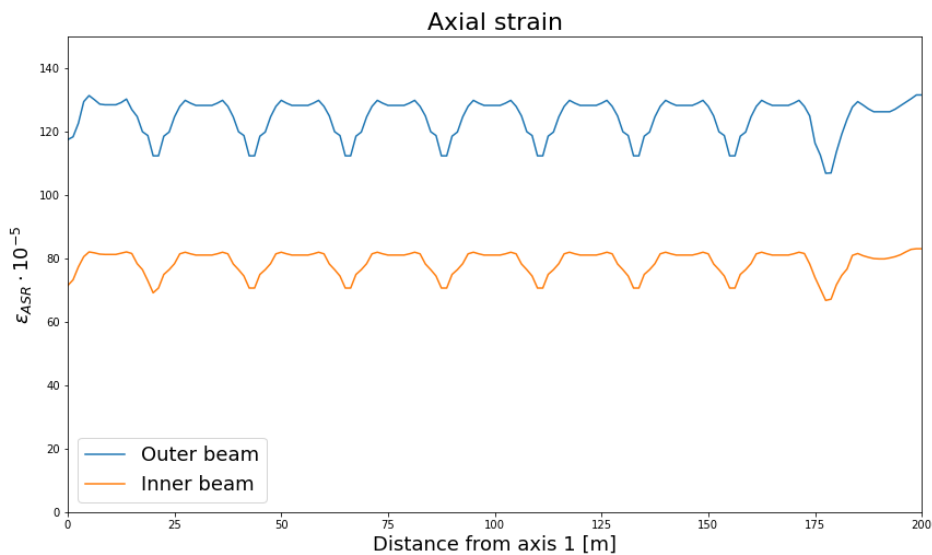


Figure 6.13: Distribution of axial strain from ASR loads along the bridge

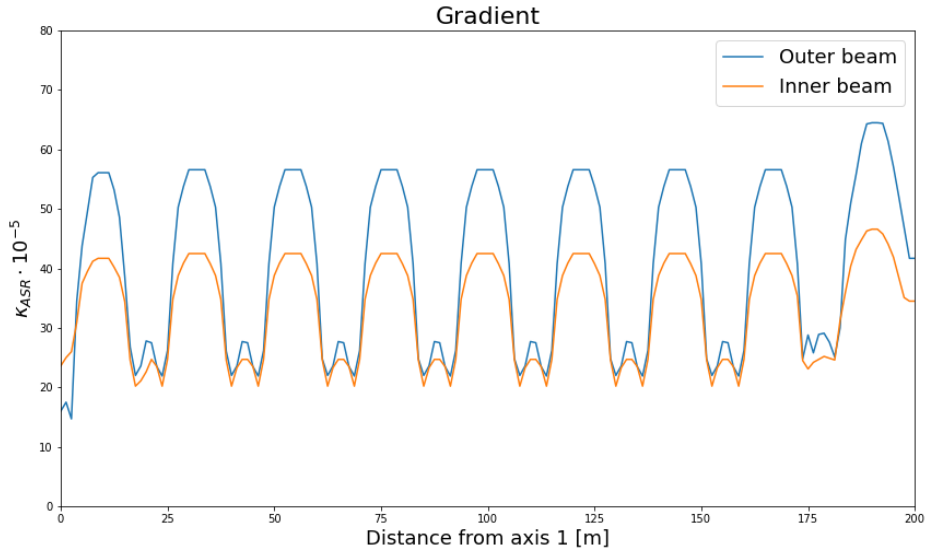


Figure 6.14: Distribution of gradient due to ASR along the bridge

6.4.4 Transformation of Loads from Aas-Jakobsen

The ASR loads from Aas-Jakobsen is given as a uniform expansion in the axis of gravity, $\varepsilon_{T.P.B.}$, and a curvature over the height of the cross-section, κ . In order to use these loads, the different contributions need to be weighted in the same height as the nodes in the shell model. As shown in Figure 6.15, one element in Aas-Jakobsen's analysis corresponds to six shell elements in the plate and two shell elements in the beam. The elements in the beam extend over the total height of the cross-section. Furthermore, the nodes are placed in the middle of the plate and the beam. Aas-Jakobsen has applied the temperature loads in beam elements, while the loads are implemented in the nodes in the shell model. The modelling of Elgeseter Bridge will be described in more detail in Chapter 7. The axial strain from the ASR loads in the plate nodes and the beam nodes are calculated from Equation (6.2) and (6.3) respectively:

$$\varepsilon_{flange} = \varepsilon_{T.P.B.} + \kappa \cdot y_{flange} \quad (6.2)$$

$$\varepsilon_{beam} = \varepsilon_{T.P.B.} - \kappa \cdot y_{beam} \quad (6.3)$$

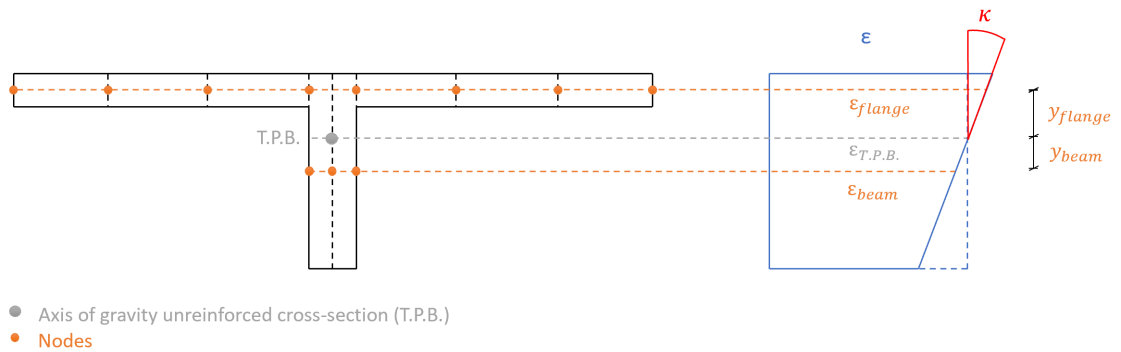


Figure 6.15: Transformation of ASR loads from frame-model to shell-model illustrated for the outer beam

The temperature loads in the longitudinal direction for the different elements are given by Equations (6.4) and (6.5), describing the contributions from the uniform expansion and the curvature respectively.

$$\Delta T_N = \frac{\varepsilon}{\alpha} \quad [^{\circ}\text{C}] \quad (6.4)$$

$$\Delta T_M = \frac{\kappa}{\alpha} \quad \left[\frac{^{\circ}\text{C}}{\text{m}}\right] \quad (6.5)$$

Where α is the coefficient of thermal expansion of concrete, equal to $10^{-5} \text{ } [^{\circ}\text{C}^{-1}]$. In this way, the initial strain from Aas-Jakobsen is applied directly in the Abaqus analysis.

6.5 ASR Loads in the Transverse Direction

The ASR loads in the transverse direction are found by evaluating the free expansion and the restraining forces from the reinforcement. The procedure to determine the loads will be presented in this chapter.

6.5.1 Free Expansion

It is assumed the same free expansion of the concrete in the transverse direction as for the longitudinal direction, illustrated in Figure 6.12. The dimension of the plates is shown in Figure 6.11 and the values of free expansion of the plate are given in Table 6.1.

Table 6.1: Free expansion in the transverse direction with $a = 0.52‰$

	Plate 280 mm		Plate 310 mm
	Outer T-beam	Inner T-beam	Inner T-beam
Expansion top	3a	2a	2a
Expansion T.P	2.917a	1.920a	1.911a
Expansion bottom	2.833a	1.839a	1.822a

6.5.2 Distribution of Reinforcement in the Transverse Direction

Due to the variation in reinforcement in the transverse direction of the bridge, the restraining forces from the reinforcement will also vary in the transverse direction. The amount of transverse reinforcement is interpolated and evaluated in the nodes as shown in Figure 6.16. It is assumed that the axis of gravity for the upper - and lower reinforcement layer is placed 41 mm from the free edge for nodes 1-11 and nodes 14-15. Whereas for node 12, the lower layer is located 51 mm from the bottom edge, and the upper layer is located 41 mm from the upper edge. Finally, the lower reinforcement layer is located 45 mm from the lower free edge for node 13. The reinforcement is shown in the original drawings in Appendix A.

The transverse reinforcement of the beams is assumed to have a small impact on the ASR loads. The ASR contributions from the reinforcement in the beams are therefore neglected. The amount of transverse reinforcement is calculated for a width of 1.25 meter in the longitudinal direction and weighted in the transverse direction for each node. Weights are decided by considering the contributions for the current layers to each node. The reinforcement amounts are shown in Table 6.2. These values are used for the whole bridge due to the small variation in transverse reinforcement throughout the bridge.

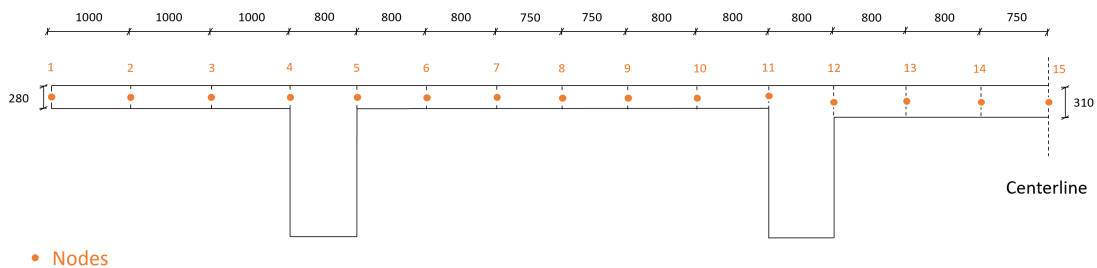


Figure 6.16: Location of nodes to determine the amount of reinforcement in the transverse direction [mm]

Table 6.2: Distribution of reinforcement in the transverse direction

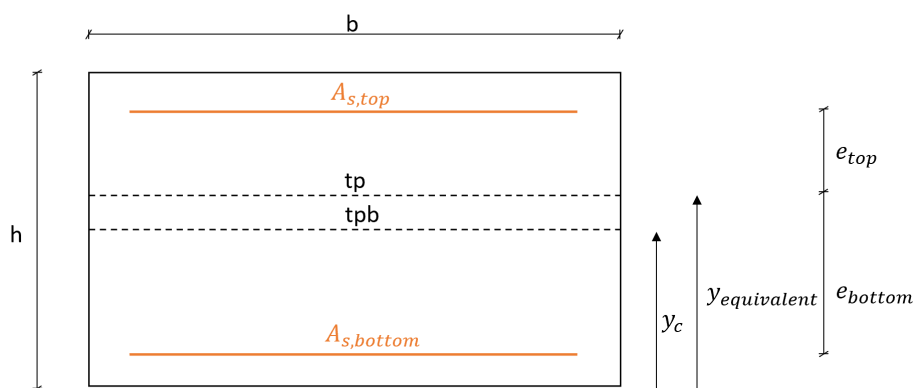
Nodes	Reinforcement top [mm^2]	Reinforcement bottom [mm^2]	Reinforcement middle [mm^2]
1	1257	165	0
2	1508	166	0
3	2074	402	0
4	2890	166	0
5	2890	754	0
6	1898	1005	0
7	1382	754	0
8	754	1005	0
9	804	854	0
10	1181	1156	0
11	2061	503	532
12	779	1566	1330
13	0	505	1927
14	0	2394	0
15	0	2394	0

6.5.3 Process to Determine ASR Loads in the Transverse Direction

The following procedure is used to find the temperature loads due to ASR for the transverse direction and is based on the principles described for load model 1 in section 6.3.1.

1. Cross-section parameters

The cross-section parameters for an elastic analysis are established.



tpb – axis of gravity of the concrete-only section

tp – axis of gravity of the reinforced cross-section

Figure 6.17: Cross-section parameters for the plate

Table 6.3: Cross-section parameters plate

	Plate 280	Plate 310
b [mm]	1250	1250
h [mm]	280	310
y_c [mm]	140	155
A_c [mm ²]	350000	387500
I_c [mm ⁴]	$2.29 \cdot 10^9$	$3.10 \cdot 10^9$

The stiffness contribution from the reinforcement is taken into account by Equations (6.6), (6.7) and (6.8).

$$A_{equivalent} = A_c + (\eta - 1) \cdot A_{s,total} \quad (6.6)$$

$$y_{equivalent} = \frac{A_c \cdot y_c + (\eta - 1) \cdot \sum(A_{s,i} \cdot y_{s,i})}{A_{equivalent}} \quad (6.7)$$

$$I_{equivalent} = I_c + A_c \cdot (y_{equivalent} - y_c)^2 + (\eta - 1) \cdot \sum(A_{s,i} \cdot (y_{equivalent} - y_{s,i})^2) \quad (6.8)$$

where η is given as $E_s/E_{c,long}$, and $y_{s,i}$ is the distance from the bottom free edge up to the current reinforcement layer, $A_{s,i}$.

2. Contributions from free ASR-expansion

The free expansion is calculated for different heights based on the values in Table 6.1:

- $\varepsilon_{free,top}$ - strain in the top edge
- $\varepsilon_{free,bottom}$ - strain in the bottom edge
- $\varepsilon_{free,tpb}$ - strain in the axis of gravity of the concrete-only section
- $\varepsilon_{free,As,i}$ - strain in reinforcement layer number i

The curvature over the height of the cross-section can be expressed as:

$$\kappa_{free} = \frac{\varepsilon_{free,top} - \varepsilon_{free,bottom}}{h} \quad (6.9)$$

Finally, the temperature load corresponding to free expansion is given by Equations (6.10) and (6.11).

$$\Delta T_{N-free} = \frac{\varepsilon_{free,tpb}}{\alpha} \quad (6.10)$$

$$\Delta T_{M-free} = \frac{\kappa_{free}}{\alpha} \quad (6.11)$$

3. Contributions from the reinforcement

The following equation determines the tensile forces in the reinforcement corresponding to the free expansion:

$$F_{s,i} = \varepsilon_{s,i} \cdot E_s \cdot A_{s,i} \quad (6.12)$$

The tensile forces results in an axial force and a moment in the cross-section given by Equations (6.13) and (6.14) respectively. The moment contribution from the reinforcement in the middle layer for nodes 11-13 is neglected due to small moment-arms.

$$N_{reinforcement} = \sum F_{s,i} \quad (6.13)$$

$$M_{reinforcement} = F_{s,bottom} \cdot e_{bottom} - F_{s,top} \cdot e_{top} \quad (6.14)$$

The strain and the curvature are determined by Equations (6.15) and (6.16) respectively.

$$\varepsilon_{reinforcement,tpb} = \frac{N_{reinforcement}}{E_{c,long} \cdot A_{equivalent}} \quad (6.15)$$

$$\kappa_{reinforcement} = \frac{M_{reinforcement}}{E_{c,long} \cdot I_{equivalent}} \quad (6.16)$$

The temperature load corresponding to the resistance from the reinforcement can be expressed by Equations (6.17) and (6.18).

$$\Delta T_{N-reinforcement} = \frac{\varepsilon_{reinforcement,tpb}}{\alpha} \quad (6.17)$$

$$\Delta T_{M-reinforcement} = \frac{\kappa_{reinforcement}}{\alpha} \quad (6.18)$$

4. Resulting ASR loads

The resulting temperature loads due to ASR are calculated by Equations (6.19) and (6.20). Furthermore, the different ASR contributions are shown in Table 6.4.

$$\Delta T_{N-ASR} = \Delta T_{N-free} + \Delta T_{N-reinforcement} \quad (6.19)$$

$$\Delta T_{M-ASR} = \Delta T_{M-free} + \Delta T_{M-reinforcement} \quad (6.20)$$

Table 6.4: Temperature loads ASR transverse direction

Nodes	$\Delta T_{N-free} [^{\circ}C]$	$\Delta T_{M-free} [\frac{^{\circ}C}{m}]$	$\Delta T_{N-reinforcement} [^{\circ}C]$	$\Delta T_{M-reinforcement} [\frac{^{\circ}C}{m}]$	$\Delta T_{N-ASR} [^{\circ}C]$	$\Delta T_{M-ASR} [\frac{^{\circ}C}{m}]$
1	151.7	31.0	-11.6	-122.9	140.1	-91.9
2	151.7	31.0	-13.5	-146.8	138.2	-115.8
3	151.7	31.0	-19.2	-167.8	132.5	-136.8
4	151.7	31.0	-23.2	-257.3	128.5	-226.3
5	151.7	31.0	-26.7	-190.1	125.0	-159.1
6	151.7	31.0	-21.9	-88.2	129.8	-57.2
7	151.7	31.0	-16.7	-67.9	135.0	-36.9
8	125.7	30.5	-11.5	17.8	114.2	48.3
9	99.8	29.9	-8.7	-0.2	91.1	29.7
10	99.8	29.9	-11.8	-6.7	88.0	23.2
11	99.8	29.9	-15.4	-104.2	84.4	-74.3
12	99.4	29.9	-15.9	32.4	83.5	62.3
13	99.4	29.9	-11.1	32.5	88.3	62.4
14	99.4	29.9	-10.6	129.1	88.8	159.0
15	99.4	29.9	-10.6	129.1	88.8	159.0

A positive gradient is defined as shown in Figure 6.15. The resistance from the reinforcement results in negative temperature loads, whereas the free expansion and the resulting strains give positive temperature loads. The large negative value for the resulting gradient in node 11 is due to a high amount of reinforcement in the upper part and a small amount in the lower part.

6.6 Deviation in Procedure to Determine the ASR Loads

When determining the ASR loads in the transverse direction, a Young's modulus equal to 200000 MPa is used for the reinforcement. In contrast, Aas-Jakobsen has used a reduced stiffness equal to 160000 MPa. ASR loads are treated as external loads and the Young's modulus should therefore not be reduced in the load calculations. Nevertheless, the values from Aas-Jakobsen are considered satisfactorily accurate.

Aas-Jakobsen has determined the ASR loads in the longitudinal direction differently than described in Section 6.5.3. There are some uncertainties regarding how Aas-Jakobsen is calculating the different strain contributions. The deviation between the two methods for a given cross-section is shown in Table 6.5. It is used a reduced Young's modulus to be able to compare the two methods. Complete calculations for the method described in this thesis is shown in Appendix B.

Table 6.5: Deviation between Aas-Jakobsen's method and the method described in Section 6.5.3

	ASR procedure	Aas-Jakobsen	Deviation
ΔT_{N-free}	121.74	121.74	0 %
ΔT_{M-free}	26.32	26.32	0 %
$\Delta T_{N-reinforcement}$	-19.48	-18.99	2.6 %
$\Delta T_{M-reinforcement}$	-13.97	-13.71	1.9 %
ΔT_{N-ASR}	102.25	102.75	0.5 %
ΔT_{M-ASR}	12.35	12.61	2.1 %

A deviation of 0.5% and 2.1% for the axial strain and the gradient are considered satisfactory. This shows that Aas-Jakobsen's method matches well with the method described in this thesis.

Chapter 7

Finite Element Analysis in Abaqus/CAE

The finite element analysis (FEA) in this thesis is performed in Abaqus/CAE. Abaqus/CAE is a software used to create models, conduct analyses and visualize results. Its user-friendly interface makes it well suited for both simple and complex analyses. CAE stands for 'Complete Abaqus Environment', a graphical interface that includes the whole process from creating the model to the post-processing of results [32].

Abaqus provides three different methods for solving finite element analyses. The three methods are Abaqus/Standard, Abaqus/Explicit and Abaqus/CFD, where the first one is used in this thesis. Abaqus/Standard is an implicit solver primarily used in static or low-speed dynamic problems. [32]

A FEA is necessary to be able to interpret the response in the bridge. The different loads, presented in Chapter 5 and Chapter 6, are applied and analysed one by one in individual models. Forces in desired elements are extracted from the results tab and load combined manually. Simple verifications are conducted by evaluating the deformed shapes from the loads.

This chapter is a review of the work conducted in Abaqus regarding the FEA of Elgeseter Bridge. This includes the modelling of the bridge, the application of different loads, and eventual simplifications. Performing a FEA of a structure like Elgeseter Bridge in Abaqus involves many choices, and simplifications are inevitable. Different decisions can affect the results in various ways, and it is important to be aware of the possible consequences.

7.1 Modelling

The Abaqus model consists of the whole bridge, where all four beams and all 32 columns are included. All columns are modelled with the same length, even though the columns in axis 2 and 9 are 10 meters long. This simplification is assumed to have an insignificant effect on the forces in the superstructure, due to the small stiffness in the columns compared to the superstructure. The columns are modelled using beam elements, while the superstructure is modelled with horizontal shell elements. The longitudinal direction of the bridge is modelled along the x-axis, while the y-axis symbolizes the transverse direction. The z-axis is consequently upwards. Furthermore, only a linear elastic analysis is evaluated in this thesis. Hence, stage I concrete is assumed for all loads in the Abaqus analysis.

The FEA model is established and drawn in meters. Since Abaqus is not applying units in the analysis, it is important to be consistent with the chosen units to interpret the desired results. Table 7.1 shows the Abaqus units corresponding to meters [33].

Table 7.1: Abaqus units [33]

Quantity	SI
Length	<i>m</i>
Force	<i>N</i>
Mass	<i>kg</i>
Time	<i>s</i>
Stress	<i>Pa(N/m²)</i>
Energy	<i>J</i>
Density	<i>kg/m³</i>

7.1.1 Elements and Mesh

The element length is decided to be 1.25 m in the longitudinal direction, which corresponds to the element size used in Aas-Jakobsen's report from 2020 [17]. This element size is used in models including the self-weight, the temperature load and the ASR loads. For models with traffic loads, an element length of 0.625 meters is used. This makes it easier to apply the point loads from traffic at desired locations.

For most load cases, the plates are divided into six elements in the transverse direction; Two elements in the middle with a width of 0.75 m and four with a width of 0.8 m. However, for the traffic load, the element distribution varies between the different load models. Nodes are needed where the point loads are to be applied, and the mesh differs accordingly. An element width similar to the element length of 0.625 m is desirable.

Both the plates and the beams are modelled with S4R shell elements. S4R is a linear four-sided conventional shell element, where each node has six degrees of freedom. The S4R element is a robust general-purpose element that is suited for a wide range of problems. Primarily uniformly reduced integration is used to avoid membrane and shear locking. This element exhibits good in-plane bending behaviour with enhanced hourglass control [34].

The length of the plates between the longitudinal beams is larger than 15 times the thickness of the plate. For this reason, the out-of-plane shear deformation will be small compared to the out-of-plane bending deformation. Thin-shell theory, where the out-of-plane shear deformations are neglected, is therefore used. Shell elements are well suited to represent in-plane forces, as well as out of plane forces. This makes it possible to understand the different load contributions in the plate, which is the primary concern in this thesis.

Intuitively, the use of only one horizontal shell element over the height of the beams seems inexpedient since the thickness becomes the largest dimension of the element. In the first place, the beams were modelled with vertical shell elements, which seemed more logical. However, the out-of-plane bending for the beams is better represented when the shell element is placed horizontally. Furthermore, the thickness-span width ratio for the beams is relatively small, which substantiates the use of only one element over the height. This also simplifies the connection between the plates and the beams. The choice of horizontal shell elements in the beams is made in consultation with co-supervisor M. Hendriks at NTNU - Department of Structural Engineering [35].

The columns are modelled with four vertically placed beam elements. The chosen element type is B23, which is a three-noded quadratic beam in space element. This is assumed to be sufficiently accurate to represent the contributions from the columns to the superstructure [35].

7.2 Geometry and Material Properties

The geometry used in the analysis corresponds to the geometry in Figure 6.11. Outer plates and the plate between the outer- and inner beam are modelled with a thickness equal to 280 mm, whereas the plate between the inner beams is modelled with a thickness equal to 310 mm. The outer- and inner beams are 1675 mm and 1740 mm high, respectively.

Both the self-weight and the ASR loads are treated as long-term loads. Consequently, the long-term Young's modulus is used for the analysis of these loads. In contrast, the traffic load and the temperature load are short-time loads, and the short-time Young's modulus is thus used to evaluate the response from these loads. The Poisson's ratio is set to 0.2 for the concrete.

7.3 Boundary Conditions and Constraints

For both the beams and the plates, the reference surfaces of the elements coincide with the shell's mid surfaces. As shown in Figure 7.1, the reference surfaces of the elements in the beams are located much lower compared to the elements in the plates. Tie constraints are used in the transition between the plate and the beam to obtain a connection corresponding to the actual behaviour of the bridge. Tie constraints ensure that both translation and rotation of the slave nodes follow the motion of a master node. In this case, the slave nodes are at the edge of the plate closest to the beam, while the master nodes are the nodes in the beam closest to the plate.

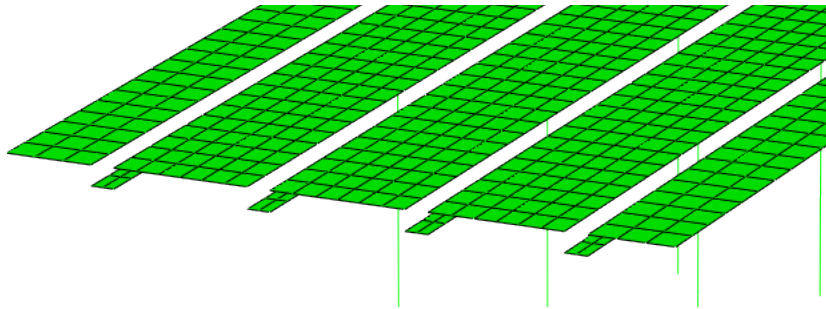


Figure 7.1: Location of reference surface for the shell elements

The columns in axis 2-8 are monolithically connected to the beams, while the columns in axis 9 have a pinned connection. In order to obtain a correct connection between the columns and the beams, two elements are used over the width of the beams. This ensures that the centre nodes in the beams are placed vertically over the top nodes in the columns. Beams and columns are attached by tie constraints, as illustrated in Figure 7.2a. The upper column nodes are established as slave nodes, and the centre nodes in the beams are selected as master nodes. Both rotation and translation are tied for the connections in axis 2-8, whereas only the translation is tied in axis 9. All columns are fixed to the ground.

Elgeseter Bridge is fully constrained at the south end and simply supported in the north end. Multi-point constraints (MPC) are chosen to represent the supports. MPCs allow the motion of the end nodes at the reference surface to be constrained to the rotation and translation in selected control points. The slave nodes are located at the reference surface of the beam, whereas the control points correspond to the nodes at the bottom edge of the beams. The constraints at the end supports are illustrated in Figure 7.2b. Both translation and rotation are fixed in the south end, while only the translation in the vertical direction is fixed in the north end. The bridge is prevented from rigid body motion in the transverse direction

due to the fixed support in the south end and the constraints from the columns. Modelling the supports directly in the reference surface gives the same results. However, MPC is used to reproduce the actual physical design of the supports. Boundary conditions and constraints are defined in the initial step before any of the loads are applied.

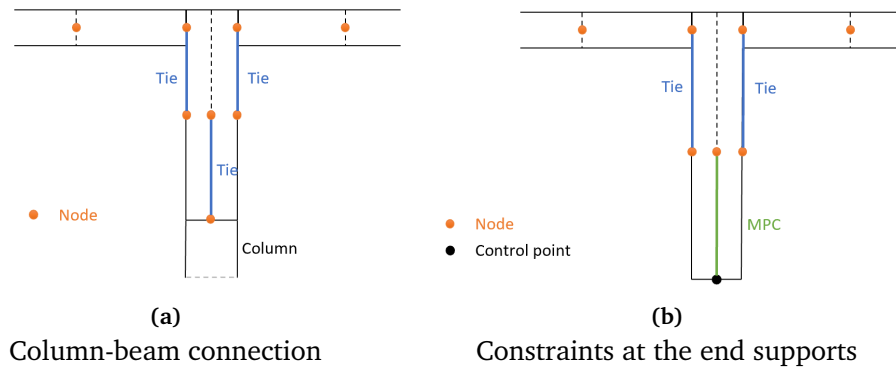


Figure 7.2: Illustration of different constraints used in the analysis

7.4 Loads

All loads are implemented in Abaqus CAE. The self-weight, the ASR load and the temperature load are applied for the whole bridge. In contrast, the traffic load is applied in specific ways and positions to generate unfavourable load contributions to the inner plates. This section describes how different loads are applied in the Abaqus model and the possible simplifications and modifications conducted in the analysis. The resulting forces from the various loads and the final load combinations are presented in Chapter 9.

7.4.1 Self-weight

The variation of the self-weight is preserved by applying the actual weight as pressure loads in each element. The pressure loads from the self-weight and the super-self-weight are shown in Table 5.1 and Table 5.3 respectively and are modelled as one load in the analysis.

7.4.2 Traffic Load

According to Handbook R412 [28], a wheel load should be applied over a surface area of 0.2 m in the longitudinal direction and 0.6 m in the transverse direction. However, due to the challenges of modelling with shells in Abaqus, the axle loads are instead applied as point loads acting in nodes located in the center of gravity of the elements. The alternative, and probably more correct solution, would

have been to apply the loads as surface loads. The loaded areas are then projected down to the centre of gravity and applied there. To include this, elements with the size of the projected areas would have been applied and placed precisely under the loaded areas. Creating meshes like this would have been very time-consuming.

Each Abaqus model, including traffic loads, must have a customized mesh where the nodes fit the load model. The element size in the longitudinal direction is halved from 1.25 m to 0.625 m for the traffic loads to achieve a better length-width ratio. The longitudinal distance between axle loads is, according to Figure 5.2 [28], supposed to be 1.3 m. However, this distance is set to 1.25 m, which corresponds to two-element lengths. This simplification is considered to have minimal impact on the response in the plates. Partitions are made through the plates in the longitudinal direction to create nodes for the desired point loads. The partitions are meshed independently to make quadratic and even elements.

Figure 7.3 illustrates the chosen load locations in the transverse direction. These load models are constructed within the rules discussed in Section 5.2.1, to obtain the most critical situations for the inner plates. Load models Traffic_1-Traffic_5 contain triple bogies, while Traffic_6 contains two double bogies. Traffic_1 is designed to generate the largest bending moments in the mid-plate. The triple bogies in Traffic_2 are placed as close to the pedestrian lane as possible to create bending moments above the outer beams. Traffic_3 and _4 act close to the inner beams and create large support moments. Both Traffic_2, _3 and _4 also generate great field moments in the plate between the inner and outer beams. Traffic_6 has the same configuration as Traffic_3, except it contains double bogies instead of triple.

The location of axles in Traffic_5 is determined by using dimensionless tables provided by supervisor T. Kanstad [36]. The tables result in dimensionless bending moments for continuous beams of different static systems subjected to point loads at different locations. Critical locations for axle loads, used in Traffic_5, are found by considering the bridge as a continuous beam with four supports, corresponding to the plate supported by the four beams.

All six traffic load configurations are applied in eight axes along the bridge. Concentrated load effects are obtained by placing the loads in the critical sections 1-6. Differentiation of the bending moment equations for a simple beam shows that traffic loads located $0.33L$ and $0.42L$ away from the columns in axis 6 and 9, respectively, generate the largest global support moments. Six transverse load cases in eight longitudinal axes result in a total of 48 individual load models in Abaqus.

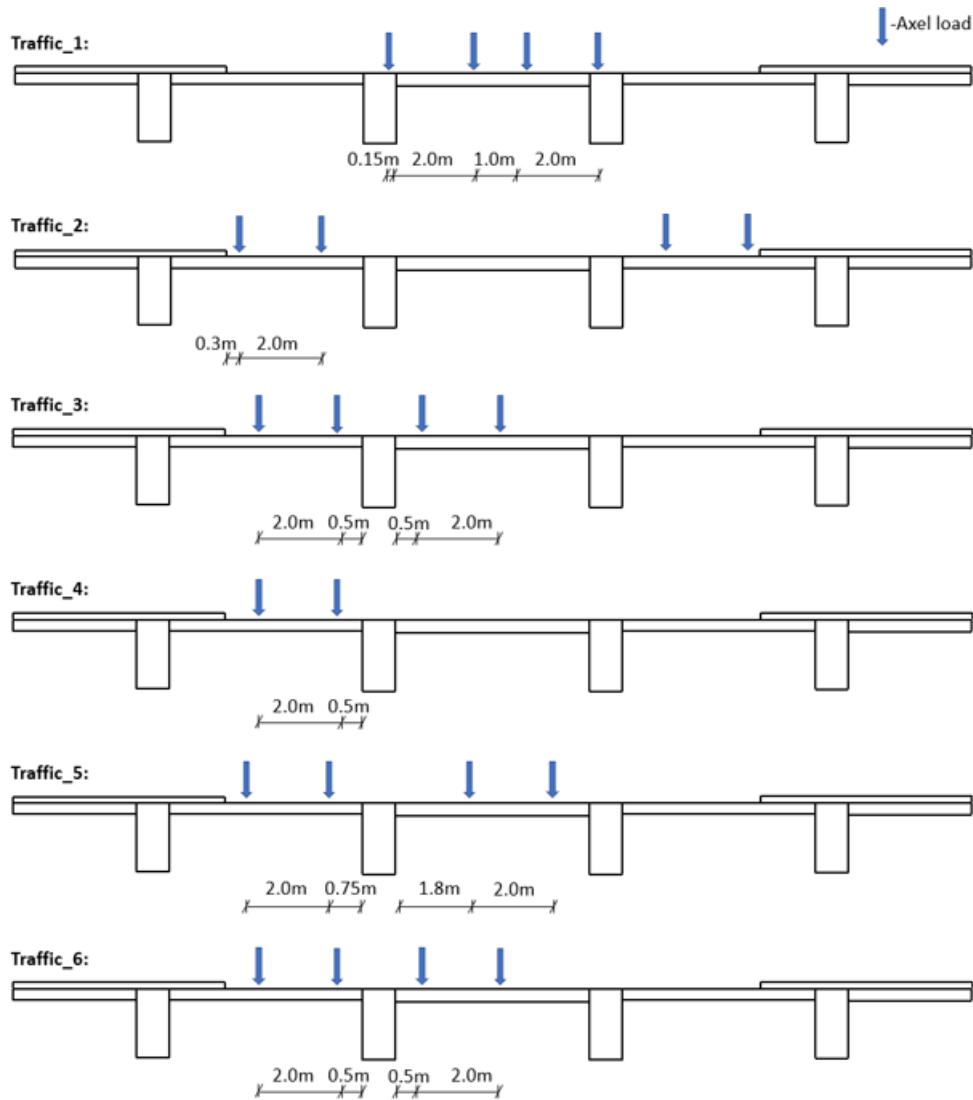


Figure 7.3: Traffic loads

Evenly distributed loads on the pedestrian lane and in other traffic lanes are neglected. They are not considered to have a large impact on the plates compared to the concentrated axle loads, which act directly in the critical sections. Avoiding these additional loads also reduces the modelling time in Abaqus. The evenly distributed loads are meant to act only in unfavourable lanes. Considering where these loads should have been applied or not in all different configurations of the traffic load would have been a time-consuming process.

7.4.3 Temperature Load

The temperature gradients $\Delta T_{M,heat}$ and $\Delta T_{M,cool}$, found in Section 5.2.2, represent the temperature difference between the upper and lower edge of the cross-section. Temperature loads are applied through *Predefined Fields* in Abaqus. An initial temperature of 0°C is assigned to the initial time step of the analysis. The temperature change is represented through another predefined temperature field assigned to the analysis's load step. Abaqus can then track the response in the construction due to the temperature variation between the load steps.

The thermal expansion coefficient, α , causes the deformations due to temperature change. The thermal coefficient is applied in all three directions, causing expansion/contraction in all directions. Temperature change in the columns is neglected. It is assumed that only the volume change in the superstructure is important for the plates.

Figure 7.4 illustrates two ways of modelling the gradient. Figure 7.4a shows how temperature loads are applied to elements according to EC1-1-5 [26]. All elements here bend about their own centre of gravity as only a gradient, and no reference temperature is applied in each node. This way of modelling temperature loads makes the bottom of the beams and the bottom of the plates having the same temperature. This way of modelling the temperature seems correct for the middle parts of the plate. However, this leads to a rather unrealistic temperature variation in the transition zone between beams and plates.

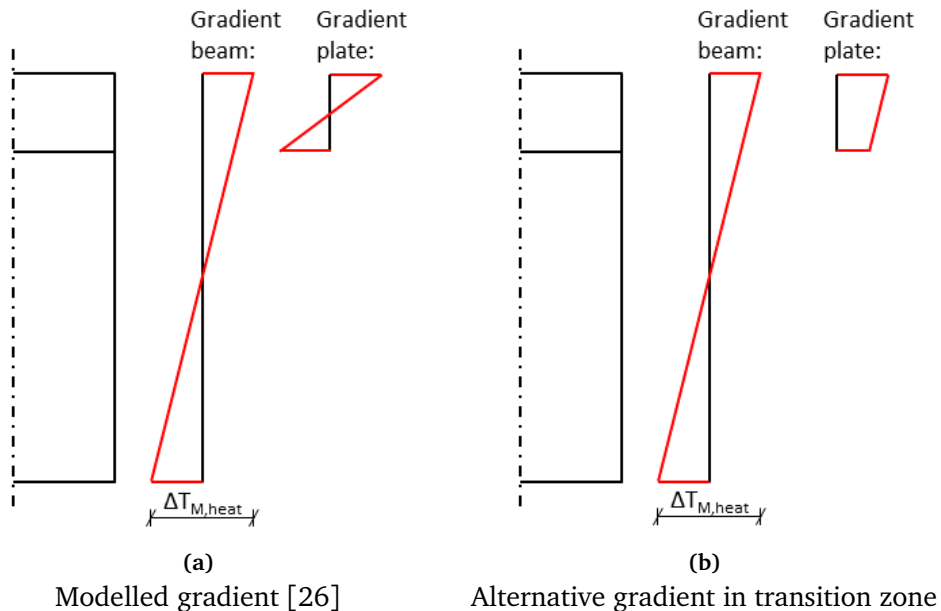


Figure 7.4: Two ways of applying the temperature gradient $\Delta T_{M,heat}$

Figure 7.4b displays an alternative temperature distribution better suited for the transition zone between the beams and the plates. The temperature of the plate corresponds to the temperature of the beam at the same height, which seems more realistic due to compatibility in the transition zone. However, it is decided to go on with the gradient from Figure 7.4a, which is considered to be the most correct method for the rest of the plates.

7.4.4 Alkali Silica Reactions

In order to preserve the effects due to ASR, the loads are modelled separately for the longitudinal and transverse direction. The process to determine the corresponding temperature loads for both directions is described in Chapter 6.

The ASR loads are modelled using predefined temperature fields, where the temperature loads are implemented in the nodes of the elements. In the initial step, the whole bridge is given a reference temperature of 0°C . The resulting temperature forces due to ASR are implemented as a *Reference magnitude* and a *Thickness gradient*, as illustrated in Figure 7.5. The thickness gradient is inserted as a change of temperature over the height $[\frac{^{\circ}\text{C}}{\text{m}}]$, and cause a curvature of the superstructure. The reference magnitude gives a uniform expansion. Temperature loads are applied in the nodes, even though Aas-Jakobsen has implemented the loads along the beam elements. Predefined temperature fields can only be applied in nodes in shell models. However, the two approaches reproduce the same response in the bridge due to ASR.

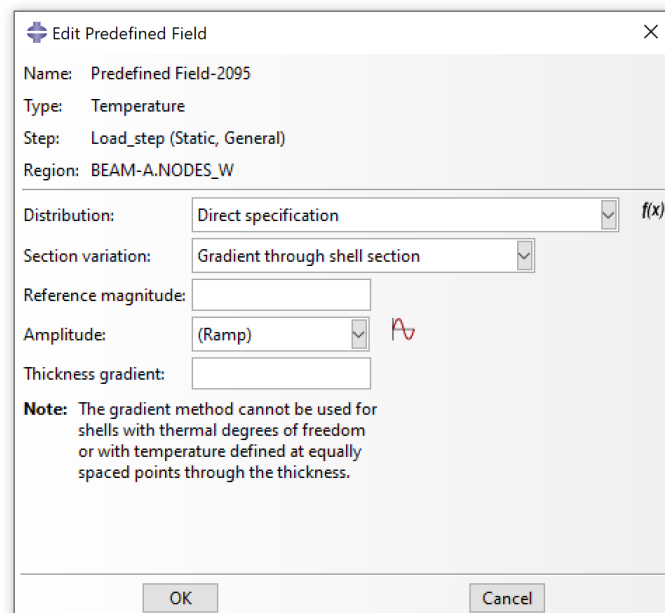


Figure 7.5: Implementing ASR loads as predefined temperature fields in Abaqus

Concrete expands in all directions when exposed to an increase in temperature. Since the loads from ASR are modelled separately for the two directions, the thermal expansion coefficient must be modified to only contribute in the corresponding direction. This is done by using an orthotropic thermal expansion coefficient.

7.5 Derivation of Results

Forces extracted from Abaqus are shown in Figure 7.6. All forces are given as force per unit width, which in this model corresponds to per meter. Section forces (SF) have unit N/m and section moments (SM) have unit Nm/m . SF1 and SF2 are axial forces in the longitudinal and transverse direction, respectively. Positive values mean that the element is exposed to tensile forces, while negative values mean compression. Arrows in Figure 7.6 point in the positive direction of the forces. Section moments are assigned positive values if they give tensile forces in the upper parts of the element. Axial forces, SF1 and SF2, and the membrane shear force, SF3, act in the plane of the shell element and are therefore called membrane forces [37]. Bending moments, SM1 and SM2, and transverse shear forces, SF4 and SF5, are called plate forces and act out of the plane. SM1 and SM2 are referred to as bending moments about the global y - and x -axis, respectively. SM3 is the twisting moment.

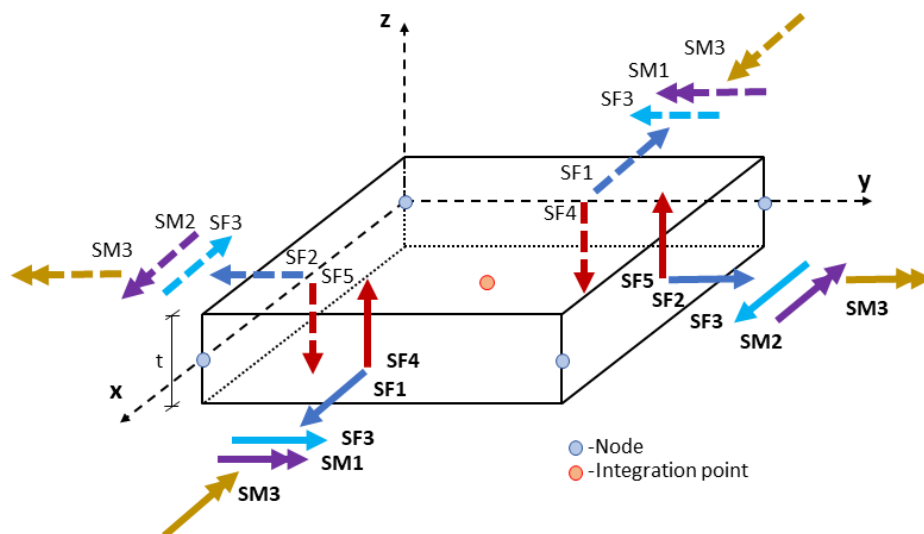


Figure 7.6: Shell element with section forces (SF) and moments (SM) extracted from Abaqus

As illustrated in Figure 7.6, the S4R shell elements have one node in each of the four corners. However, reduced integration reduces the number of integration points by one in each direction, compared to full integration, where all nodes are used as integration points. Results for an S4R element are therefore provided in

only one integration point. Nodes and integration points are illustrated in Figure 7.6.

The desired forces are extracted from the integration points in the model by using probe values. For a specific critical section, it is chosen to conservatively gather forces from the most unfavourable elements nearby the considered section. Choosing between elements is inevitable, as locations of integration points vary due to the varying meshes. This is considered reasonable, especially for the traffic load since it is moving. Forces from different loads are summed up by load combinations, as described in Section 5.5.

Contour plots and deformed shapes are helpful tools to examine and understand the response and structural behaviour. Understanding how forces are distributed and how they are transferred through the structure is necessary to determine critical sections and load contributions. Contour plots use colours to show the magnitude of the desired variable. Blue and red often symbolize the negative and positive extreme values, respectively. Contour plots are used to identify critical sections for different loads. Modelling loads in independent models makes it easier to interpret the response in the bridge. The deformation plots are scalable, which is useful to enlighten small displacements.

Default contour plots in Abaqus use values from neighbouring elements to make smooth colour plots. The smooth distributions look realistic considering the way forces are smoothly distributed. However, it is important to remember that by using S4R elements, the forces are calculated in one node per element. Figure 7.7a and 7.7b illustrate the smoothed and the distinct valued plot, respectively. The distinct valued plots are used when extracting resulting forces to make sure no extreme values are ignored. However, smoothed plots are used for illustrations.

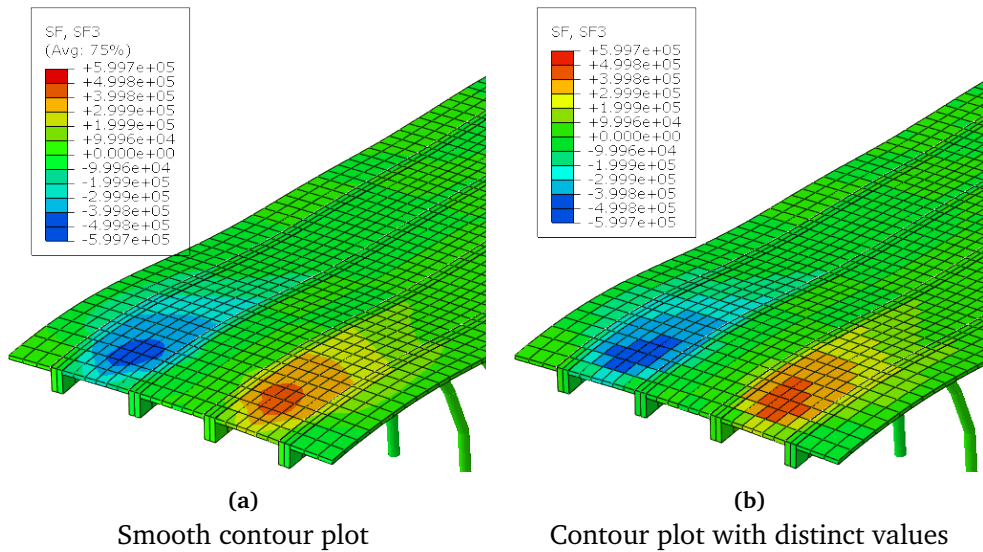


Figure 7.7: Contour plot options in Abaqus, illustrated by SF3 from ASR

7.6 Verification of Results

An important aspect of modelling is the verification of the results. Even though the analysis run without errors, the results must agree with the expected outputs. The shell model of Elgeseter Bridge is complex, and it is not straightforward how the different loads are transferred in the model.

Self-weight

Bending moments from the self-weight about the y-axis, SM1, are compared with values from Aas-Jakobsen's T-beam in their report from 2020 [38]. The verification is conducted by calculating the bending moments about the axis of gravity corresponding to Aas-Jakobsen's T-beams. Shell elements within the T-beam give contributions from their axial force and their bending moments. Complete calculations regarding the comparison are given in Appendix C. Aas-Jakobsen has calculated the super-self-weight slightly different, and some deviation in results are expected. Furthermore, uncertainties are related to the values from Aas-Jakobsen's report as they are extracted from relatively coarse moment diagrams. However, the deviations presented in Table 7.2 are observed to be relatively small, and the model is considered to transfer the self-weight correctly.

Table 7.2: Verification of self-weight in axis 8 and 9

	Shell model [kNm]	Aas-Jakobsen [kNm]	Deviation [%]
Outer T-beam axis 8	4227	3975	6.3
Inner T-beam axis 8	2815	2750	2.3
Outer T-beam axis 9	4732	4800	1.4
Inner T-beam axis 9	3349	3400	1.5

Traffic Load

The accuracy of applying the axle loads as point loads are verified through influence diagrams [39] provided by supervisor T. Kanstad. Traffic load configuration *Traffic_4*, illustrated in Figure 7.3, is used for the verification. All six wheels from the triple bogie are drawn into the diagram with their projected load areas. A factor describing the contribution to the bending moment is then extracted from the diagram for each wheel load. The total bending moment in the middle of the plate is found by summing the contributions.

The verification is conducted using two influence diagrams [39] representing the upper and lower limit of the bending moment in the plate. The upper limit describes a simply supported one-way slab. This is a conservative representation since the beams provide stiffness to the plate. The lower limit case is more similar to the behaviour of the plates in Elgeseter Bridge and is represented by a one-way slab with one fixed end and one simply supported end. Inner beams are less prone to rotations due to the support from each other and the inner plate. On the other hand, the outer beam gets no stiffness contribution from the outer plate and is easier to rotate. The chosen upper and lower limit influence diagrams result in bending moments of magnitudes 28.6 kNm/m and 22.0 kNm/m , respectively. In comparison, the corresponding Abaqus model gives a bending moment of 23.9 kNm/m . Using point loads in Abaqus instead of surface loads is assumed to be sufficiently accurate since the resulting bending moment is between the upper and lower limit. It is also observed that the bending moment is closer to the lower limit, as expected.

Longitudinal ASR

Loads due to ASR obtained from Aas-Jakobsen are calculated based on a total displacement of 200 mm in the longitudinal direction. The shell model gives a total displacement of 203.1 mm and 198.6 mm for the outer- and inner beams, respectively. The average total displacement is then calculated to be 200.8 mm, substantiating that the ASR load is modelled correctly in the analysis.

Chapter 8

Interpretation of Forces

Loads are applied and analyzed in individual models in order to extract and interpret the responses separately. This chapter will discuss the load effects in Elgeseter Bridge and explain each modelled load. The resulting responses are extracted from the Abaqus models presented in Chapter 7.

The plates can be considered as one-way slabs, supported by two beams. Vertically acting loads applied on the plates are generally transferred through the slab and into the bearing beams. Beams transfer forces to the columns, where they further are sent down to the ground.

In the following plots, only forces in the plates will be displayed. Some forces in the beams are very large compared to the forces in the plates and might therefore dominate the extreme values and colours in the contour plots. Ignoring the beams makes it easier to illustrate and enlighten the response in the plates. However, it is essential to remember that the beams are exposed to great forces, even though the following plots show zero force expressed by the green colour.

Colour charts attached to the following contour plots illustrate the magnitudes designated to different colours. The displayed values are only used to interpret the response by considering the magnitude and the sign of the loads. For extraction of forces for the final load combination, exact values from the desired elements are used. Signs in the contour plots correspond to Figure 7.6, where all forces are oriented in their positive directions.

8.1 Critical Sections

Due to symmetry, only one of the plates between the inner and outer beams is evaluated, together with the inner plate. Chosen critical sections A, B, C, D and E are shown in orange in Figure 8.1. Sections A, C and D correspond to the integration points in the plates closest to the beams. Most elements have a width

of 0.8 m, which means that the integration point is located 0.4 m out from the beams. Sections B and E are located in the mid-span of the outer and inner plate, respectively. These five sections are chosen because they are expected to experience the most significant bending moments in the transverse direction, SM2, from the vertical loads.

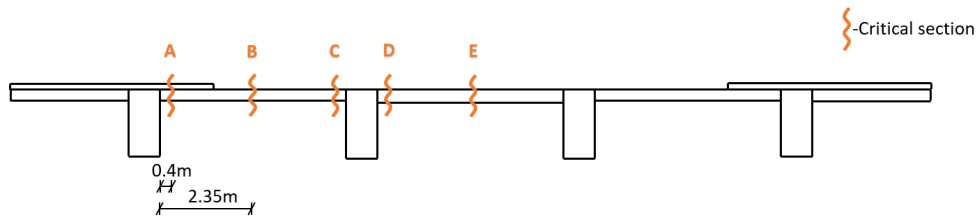


Figure 8.1: Critical sections in the transverse direction, A-E

The five critical transverse sections are considered at seven different sections in the longitudinal direction. The chosen sections, named 1-7, are shown in Figure 8.2. Sections 1 and 4 represent sections above columns in axis 6 and 9, respectively, where the maximum global bending moments from vertical loads are located. Sections 3 and 5 correspond to the points of maximum global bending moment in the mid-span due to the self-weight, while section 2, on the other hand, represent the point of zero bending moment. Because of a significant membrane shear force generated by the ASR load, also section number 6 at the end of span 9, is considered. Section 7 is located in the outermost element row in axis 10 to control the great transverse compressive force due to the ASR load.

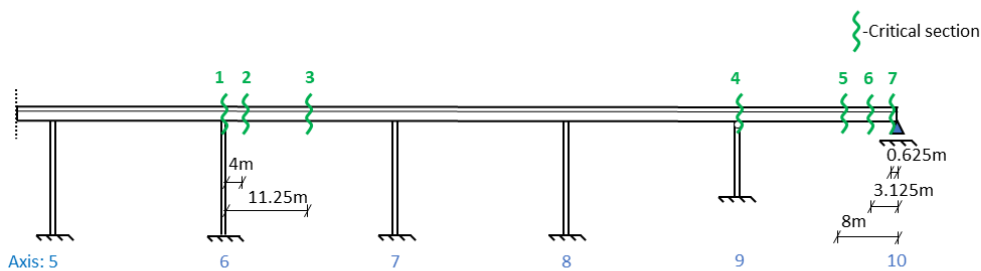


Figure 8.2: Critical sections in the longitudinal direction, 1-7

Every critical section is hereby assigned a section ID based on Figure 8.1 and Figure 8.2. The ID of a critical section is composed of the longitudinal section number, followed by the transverse letter. They will be referred to as S, for section, followed by their ID.

8.2 Self-weight

Forces generated by the self-weight are generally observed to be significant compared to contributions from other loads. The cross-section of the whole superstructure seen as one experiences a global bending moment from the self-weight, causing axial forces in the plates. The global bending moment generates tensile forces in the slabs in the column axis and compressive forces in the slabs in mid-spans.

The variation between tensile and compression forces is relatively steady along the bridge, except in the northernmost column axis and the following span. The pinned connections between beams and columns in axis 9 allow a greater curvature of the superstructure. This leads to more prominent global bending moments and consequently more significant axial forces in the plates. The contour plot of SF1 from the self-weight is illustrated in Figure 8.3a. It is important to remember that only the axial force in the plates are shown.

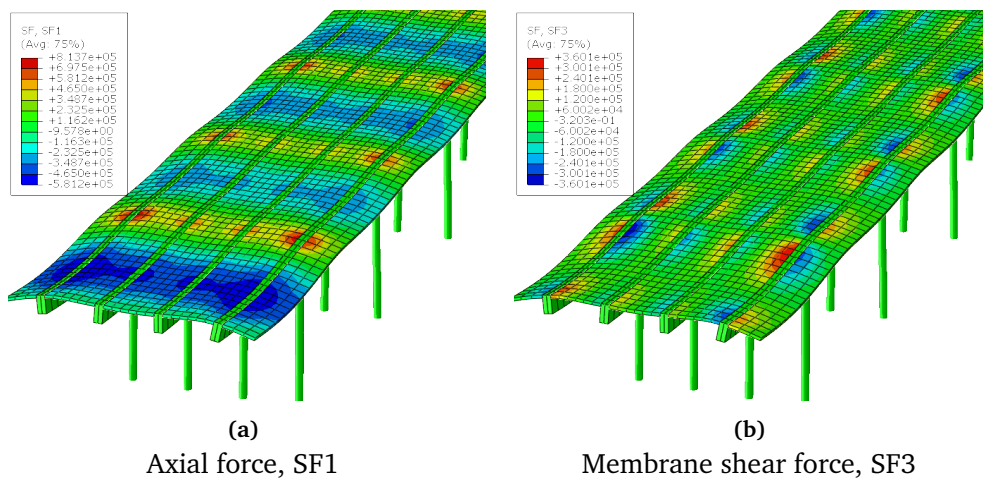


Figure 8.3: Section forces from self-weight

Contour plots reveal some interesting aspects regarding the way forces are transferred through the structure. Figure 8.3a and Figure 8.3b illustrate SF1 and SF3, respectively, in the plates due to the self-weight. It is observed that SF3 is low where SF1 is steady and constant, and that SF3 has its maximum values where SF1 changes the most. The reason for this is that SF3 occurs from the change in axial force due to the horizontal equilibrium. Figure 8.4 illustrates a beam between two columns with its effective widths, including the plates, in three sections. By considering the longitudinal equilibrium of the three sections with their effective widths, it is clear that membrane shear forces from the beam are needed for the axial force to change in the plate. The purple arrows illustrate in-plane shear forces acting on the plate from the beam. The green arrows show how shear forces are transferred through the slab.

The three sections in Figure 8.4 are illustrated with different effective widths, b_{eff} . A common practice in dimensioning of a T-beam is to use the effective width, calculated based on the location of the zero bending moment, the span length and the boundary conditions. According to EC2, T-beams should be considered as rectangular beams with effective width b_{eff} in the mid-span where the compression zone is in the flange [25]. This makes the neutral axis move higher up in the cross-section, allowing greater strains in the lower reinforcement. Over column axes, where the compressive zone is located in lower parts, only the width of the web is considered. However, the reinforcement within the calculated effective width can be used in the flange. The upper section in Figure 8.4 is therefore sketched with an effective width of b_{eff} , even though the flange is in tension. In reality, axial forces spread out gradually in the flange, from zero in the point of zero bending moment to its maximum in the mid-span and over columns. Sections in Figure 8.4 are therefore illustrated with different effective widths due to their location in the span.

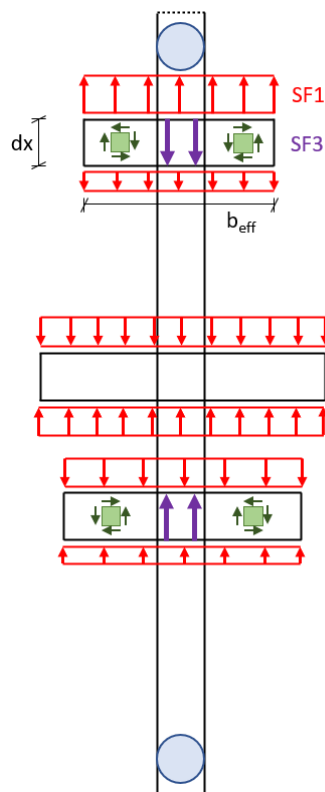


Figure 8.4: Longitudinal equilibrium of three T-beams with their effective widths, seen from above

8.3 Traffic Load

The six traffic loads, illustrated in Figure 7.3, are chosen to give the most unfavourable load contributions to the critical sections shown in Figure 8.1. Common for the traffic loads is that they give very concentrated forces, compared to the other loads.

Traffic loads applied in mid-spans create a global bending moment for the superstructure about the y-axis, SM1, inducing axial forces, SF1, in the slabs. These axial forces amplify the contributions from the self-weight, generating tensile forces in the nearby column axes and compressive forces in the mid-span underneath the loads. Traffic loads located $0.33L$ and $0.42L$ away from the columns in axis 6 and 9, respectively, generate the largest global support moments. Traffic loads located in the column axes, on the other hand, give insignificant global bending moments. Forces here go directly down to the columns without generating a global curvature on the superstructure.

The axle loads provide concentrated bending moments in both directions due to local deformations of the plate. The resulting contour plots for the bending moments from the load case Traffic_3, located over columns in axis 6, are shown in Figure 8.5. Worth noticing is how concentrated the fields of negative bending moments illustrated in blue are. This is because bending moments originate from the curvature caused in the slabs and are therefore largest under the load and in the transition to the beams. Most of the bending moment is transferred to the beams through SM2, shown in Figure 8.5b, because of the rigid connection to the beams and the short span. As Figure 8.5a illustrates, also bending moments about the y-axis, SM1, are generated. SM1 is smaller than SM2 due to the longer span absorbing the deformation and a smaller curvature in the x-direction.

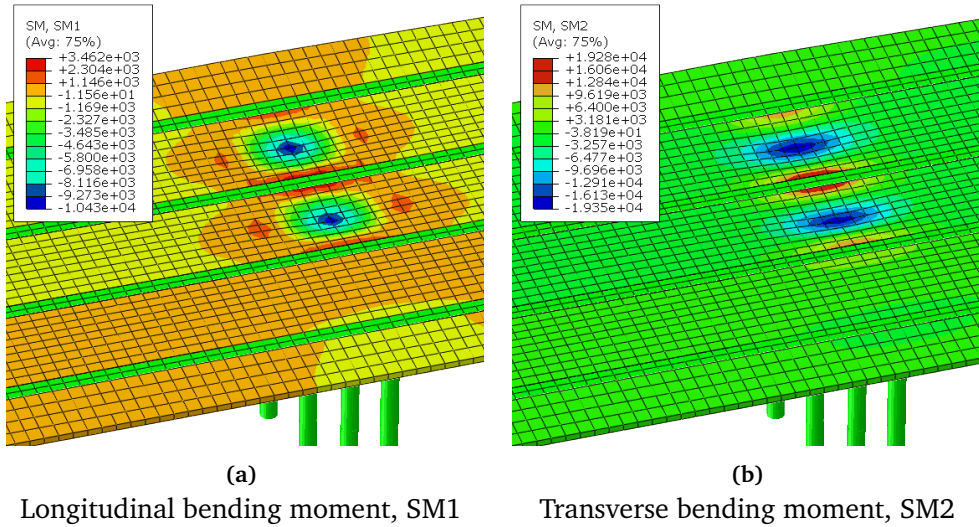


Figure 8.5: Bending moments from load Traffic_3 located in column axis 6

Figure 8.6 displays SF1 and SF3 for load case Traffic_3 located in span 6. Membrane shear forces are generated as traffic loads are located in the mid-span, for the same reason as for the self-weight, illustrated in Figure 8.4. Notice that SF3 is zero where SF1 is stable, like in the column axes and beneath the loaded area. The membrane shear force increases significantly as the axial force starts to change. Thus, SF3 from traffic loads is most relevant for the capacity control in sections at the point of zero bending moment.

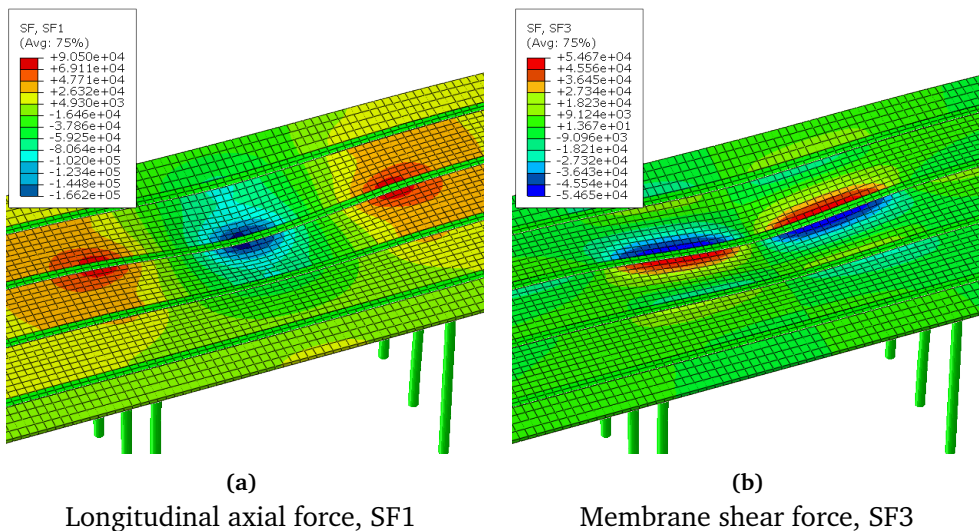


Figure 8.6: Section forces from load Traffic_3 located in span 6

8.4 Temperature Load

Generally, the temperature loads have a marginal impact on the bridge compared to the other more significant loads. However, load combinations with temperature as the dominating load is in some sections observed to be decisive. This happens primarily in sections where traffic loads give favourable contributions. Forces from temperature change arise due to the restraints in the structural system. The temperature gradient, through the height of the cross-section, forces the superstructure to curve vertically. The columns and the fixed supports prohibit this free deflection and cause restraint forces in the structure. Restraint moments are determined by the stiffness of the structure, EI , and the induced curvature, κ , as shown in Equation (8.1).

$$M = -EI \cdot \kappa \quad (8.1)$$

The two modelled temperature fields, corresponding to the heated or cooled upper surface, result in global bending moments with opposite signs. A heated surface creates an upward deformation, which generates a negative global bending moment. The opposite case, with a cooled surface, provides a positive global bending moment. Figure 8.7 displays the contour plots for SM1 for both temperature fields. Notice that the sign of the bending moments is almost constant for all elements in a temperature field and that the two cases have opposite sign. Deformations, and thus the global bending moments, are more significant in the case with a heated surface due to the larger gradient found in Section 5.2.2. The transverse bending moment, SM2, has the same sign and magnitude as the longitudinal bending moment, SM1.

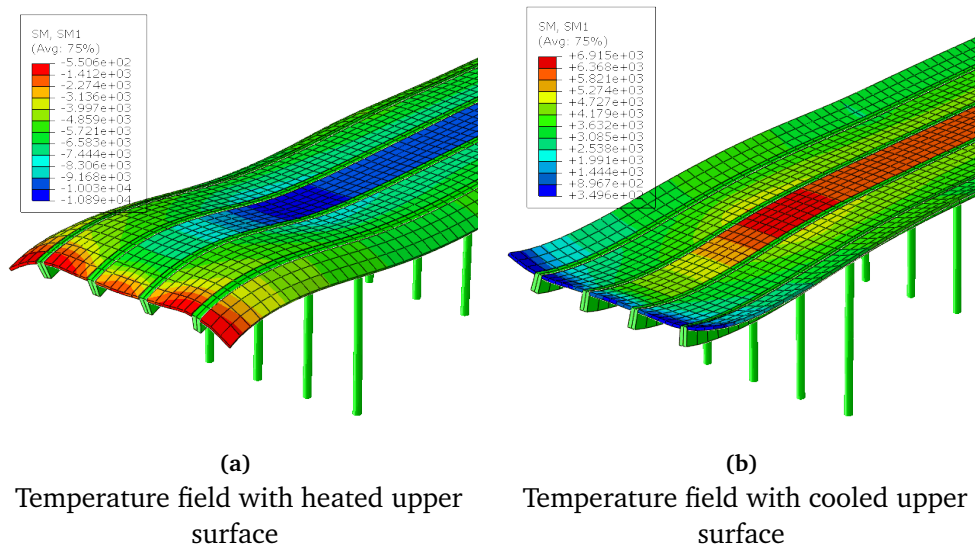


Figure 8.7: Longitudinal bending moment, SM1, for the two temperature fields

The axial force, SF1, increases as the global curvature is allowed to develop in spans 8 and 9, as shown in Figure 8.8. The plates have no uniform expansion from the temperature loads and are therefore not expanding together with the parts of the beams at the same height. The gradients in the beams cause a global curvature of the superstructure and induce axial forces in the plates. Axial forces in the plates of spans 1-7 are observed to be fluctuating between positive and negative insignificant values because of minor global curvatures. However, the restraint moments generate large axial stresses in the upper parts of the beams in these spans.

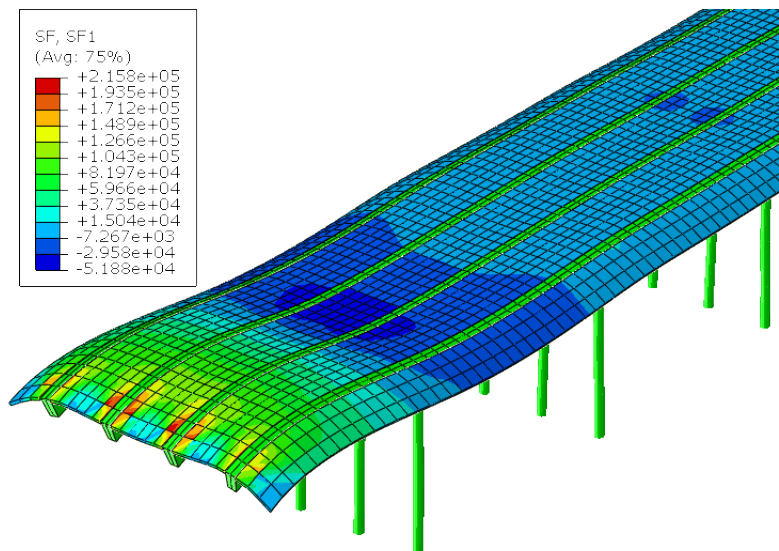


Figure 8.8: Axial force, SF1, from the temperature load TempH

The last two element rows near axis 10 are observed to be exposed to concentrated axial forces in the transition between the beams and the plates. Axial forces are significant in span 9, and need to build up fast from zero at the simply supported end. The process of building up axial forces, including concentrated shear forces, SF3, and transverse axial forces, SF2, are more clearly illustrated in the resulting forces from ASR and will be explained in more detail in Section 8.5. Further out in the span, the axial forces distribute to neighbouring elements. Elements have approximately equal axial force already in element row 4, 4.375 m from axis 10.

8.5 Alkali-Silica Reactions

Alkali-silica reactions provide some of the most significant forces observed in the structure. As earlier mentioned, the expansions due to ASR are modelled in separate models for the longitudinal, and transverse direction to easier interpret the responses. Thus, the two cases are discussed and presented individually.

8.5.1 ASR in the Longitudinal Direction

Analysis performed in Abaqus shows that ASR is the load that generates the most significant axial forces, SF1, in the plates of Elgeseter Bridge. The expansions provide relatively stable axial forces along the bridge, as illustrated in Figure 8.9. Compressive and tensile forces are displayed in blue and red, respectively.

The sign of SF1 changes in the middle of the plates between the inner and outer beams, section B. Consequently, the axial force has to be zero somewhere in the slab between the beams. None of the integration points in the Abaqus model is located precisely along this line of zero axial force. The resulting SF1 is therefore conservatively extracted from the nearby element with the most unfavourable contribution to the load combination. The axial force increases fast after changing sign, and significant axial forces are also obtained in section B.

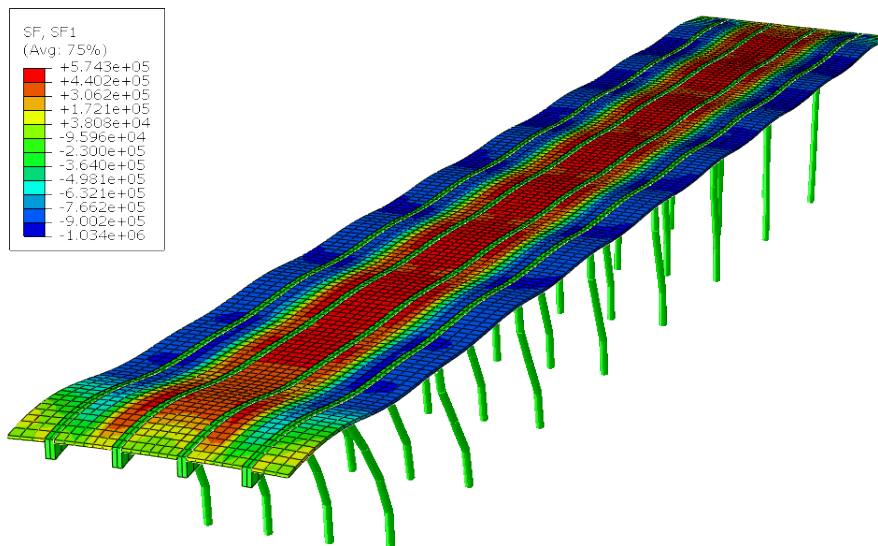


Figure 8.9: Axial force, SF1, from ASR in the longitudinal direction

Columns give additional axial forces in the superstructure due to their horizontal deformations. This additional force builds up towards the fully restrained end support in axis 1 from zero in span 9, as more columns contribute. However, the columns have low stiffness, and the provided compressive force is therefore small.

Axial forces, SF1, are stable along the bridge, except in span 9, as Figure 8.9 shows. The supports in axis 10 are free to move in the longitudinal direction of the bridge and can not absorb axial forces in the x-direction. Thus, for the axial force to build up, large internal forces are generated in the slabs of span 9. Figure 8.10 illustrates the contour plots for the transverse axial force, SF2, and the membrane shear force, SF3. Large transverse compressive forces appear along the edge in axis 10 as the plates are pushed together. The inner plate is most

exposed, as the blue colour in Figure 8.10a clearly shows. However, just 5 meters out in the span, the sign of the force has changed, and suddenly the inner plate is subjected to tensile forces.

Figure 8.10b displays the characteristic membrane shear force, SF3, in the slabs of Elgeseter Bridge generated by ASR. The membrane shear force has a considerable magnitude along the whole bridge but has its clear maximum of just 2-3 meters from the end support. Both SF2 and SF3 originate from the build-up of the axial force, SF1, at the beginning of span 9.

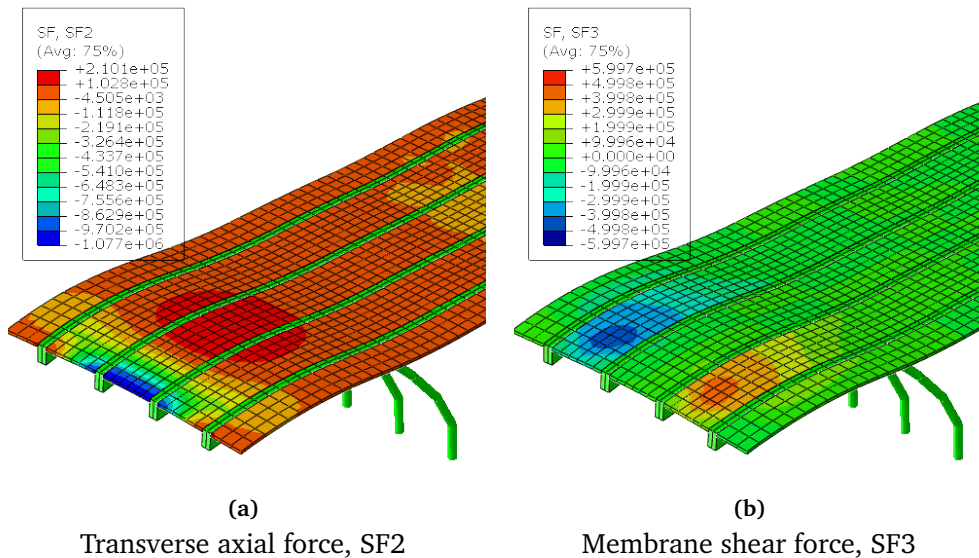


Figure 8.10: Section forces in span 9 from ASR

Figure 8.11 illustrates the last part of span 9, seen from above, and is used to explain the forces in the plates generated by ASR. The superstructure is divided into four T-beams, depending on the sign of the axial force, SF1. Figure 8.11a separates parts in compression and tension in colours blue and red, respectively. The purple element in Figure 8.11b is an imagined segment of the western outer T-beam. Horizontal equilibrium of the element in x-direction clarifies that a shear force is needed to neutralize the earlier mentioned increasing axial force, SF1, from ASR. This is a consequence of the fact that no horizontal forces can be absorbed in the two free edges of the element. The simply supported end in axis 10 provides no horizontal restraints.

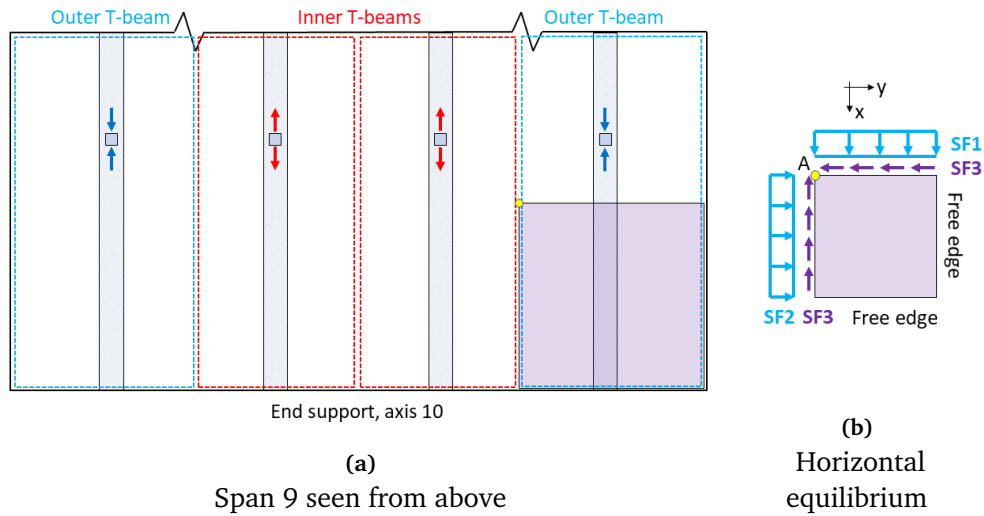


Figure 8.11: Horizontal equilibrium of a part of span 9 towards axis 10, seen from above

Further on, moment equilibrium about point A of the element illustrated in Figure 8.11b is conducted. To obtain moment equilibrium, an axial force in the y-direction, SF2, is needed. SF1 and SF2 are the only forces generating moment about point A. Finally, a membrane shear force, SF3, is introduced because it is the only force that can maintain horizontal equilibrium in the y-direction. Figure 8.11b shows all horizontal forces acting on the element.

Axial forces, SF1, use span 9 to build up as explained by generating large SF2 and SF3. On the other hand, in spans 1-8, the axial forces are acting on the elements with approximately the same magnitude from both sides. Thus, only minor shear forces and transverse axial forces are needed to keep the elements in equilibrium.

The gradient modelled to reproduce the ASR expansions makes the upper parts expand more than the lower. The generated deflection is comparable to the response from the temperature load with a heated surface. Restraint forces from the columns create a global negative bending moment along the bridge, inducing compression forces in the plates. Unlike the response from the modelled temperature loads, the slabs and the top of the beams expand together when subjected to ASR. Expansions are compatible between the plates and the top of the beams. The bending moments SM1 in the slabs have the same sign as the global bending moment. SM1 in the plates are of considerable magnitude, while bending moments in the transverse direction, SM2, are insignificant.

8.5.2 ASR in the Transverse Direction

The amount of transverse reinforcement is constant in the longitudinal direction of the bridge. The temperature fields are consequently equal for all element

rows along the bridge, and thus, no restraint forces due to varying expansion in the transverse direction are generated. However, varying reinforcement in the transverse direction causes an inconsistent ASR expansion over the width of the bridge. The last column of Table 6.4, containing the calculated temperature fields, shows that the gradient even changes sign over the width. Figure 8.12 shows the contour plot for SM2 with corresponding deformation.

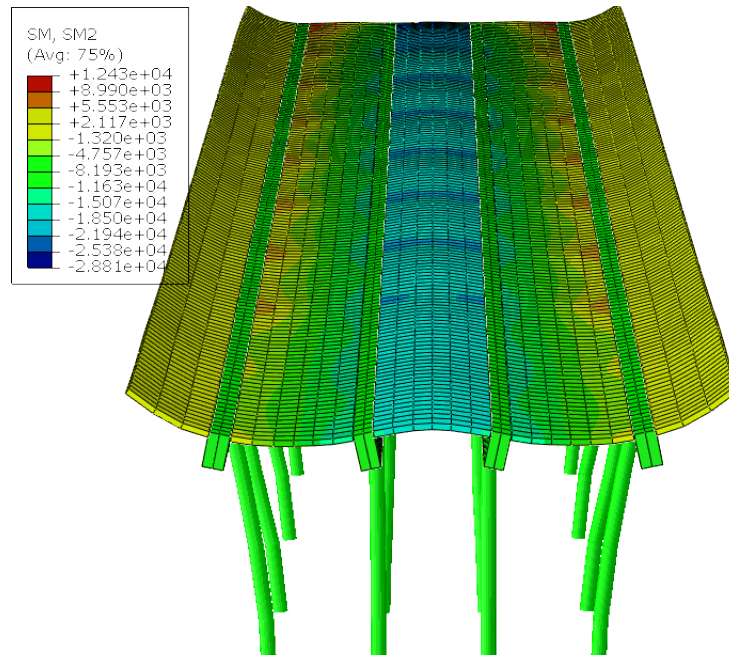


Figure 8.12: Transverse bending moment, SM2, from ASR in the transverse direction

The positive gradients in the mid-plate generate an upward deflection, which the beams counteract by introducing a negative restraint moment, displayed in Figure 8.13. Most parts of the plates between the inner and outer beams are exposed to gradients with a negative sign, causing a downward deformation. However, the rotation of the inner beams, induced by the large gradients in the inner plate, causes a further downwards deflection. Outer plates expand freely without restraints from the beams, and consequently, they have negligible bending moments. SM2 in the beams are ignored in the plot in Figure 8.13 to highlight the response in the plates.

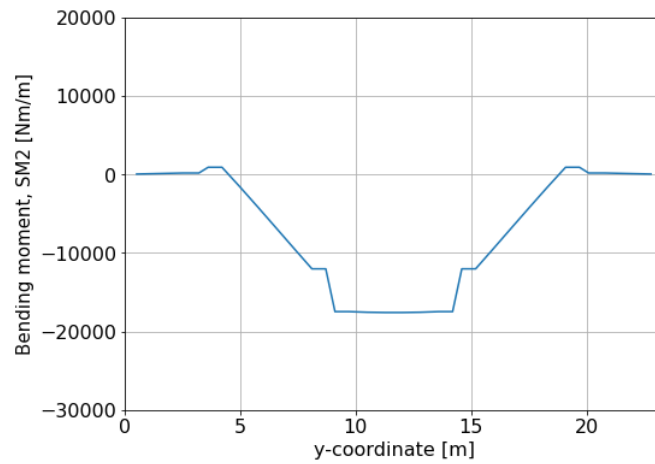


Figure 8.13: Transverse bending moment, SM2, from ASR in a typical mid-span section

Including the transverse ASR expansions in the analysis introduces considerable force contributions. SM2 is observed to be in the same order of magnitude as the transverse bending moment from the self-weight in section E, in the inner plate.

Chapter 9

Resulting Forces

In this chapter, the resulting forces are presented for the critical sections illustrated in Section 8.1. Forces generated from the different loads and the dimensioning load combinations are tabulated for all 35 sections. Notice that sections here are named by their section ID, containing a transverse (A-E) and a longitudinal (1-7) coordinate, from Figure 8.1 and Figure 8.2.

9.1 Load Combinations

The assumed most unfavourable traffic load is chosen for each critical section, amongst the 48 load configurations. Loads applied in the considered longitudinal axis is in general found to be worst, as they generate local transverse bending moments. However, for sections B-E in the column axes S1 and S4, traffic loads located in the span are found critical. Tensile forces are here generated in the slabs by global bending moments. For section A the traffic loads are applied in the considered section to amplify the positive transverse bending moments from the self-weight.

Whether the temperature load with a heated or cooled upper surface is chosen is based on the moment contributions from the dead load and the ASR load. The case with warm upper surface and cold upper surface are named *Temp_H* and *Temp_C*, respectively, in the load combinations.

The following tables summarize the results from the finite element analyses in Abaqus. Tables containing resulting forces, load combinations and choices regarding the selection of loads are presented for each longitudinal section, 1-7. Load combinations marked with red colour are evaluated in the capacity control in Chapter 10.

9.1.1 Axis 6 (S1)

Table 9.1: Forces axis 6 (S1)

		Self-weight	Traffic	Temperature	ASR	ASR transverse
Section A	SF1 [kN/m]	707.0	-3.1	-4.9	-906.5	19.3
	SF2 [kN/m]	-91.3	-2.5	1.9	-6.0	0.2
	SF3 [kN/m]	-134.4	-0.6	-1.4	-36.5	-0.5
	SM1 [kNm/m]	29.5	2.5	3.5	-7.6	1.7
	SM2 [kNm/m]	69.7	16.3	1.4	-2.4	5.3
	SM3 [kNm/m]	-0.4	-0.5	0.0	0.1	0.3
Section B	SF1 [kN/m]	361.1	21.6	0.5	56.2	3.2
	SF2 [kN/m]	78.3	3.8	0.2	-17.9	2.1
	SF3 [kN/m]	-22.2	15.2	0.2	8.6	-0.7
	SM1 [kNm/m]	16.3	0.9	4.2	-6.9	-1.0
	SM2 [kNm/m]	23.1	1.4	4.4	-1.3	-6.4
	SM3 [kNm/m]	-1.0	1.2	0.0	0.1	-0.2
Section C	SF1 [kN/m]	493.2	66.5	4.7	366.5	-13.8
	SF2 [kN/m]	21.3	-9.1	-1.2	-30.1	6.7
	SF3 [kN/m]	67.1	35.1	0.7	34.4	4.5
	SM1 [kNm/m]	11.8	2.1	4.7	-6.6	-2.9
	SM2 [kNm/m]	8.9	3.4	6.3	-1.4	-13.5
	SM3 [kNm/m]	-0.7	1.6	0.0	0.0	-0.2
Section D	SF1 [kN/m]	511.0	79.1	5.8	432.2	-21.1
	SF2 [kN/m]	39.2	-4.1	-1.2	-34.2	1.9
	SF3 [kN/m]	-74.0	-25.0	-0.9	-33.0	1.9
	SM1 [kNm/m]	14.9	1.8	6.1	-9.1	-4.6
	SM2 [kNm/m]	7.4	-2.1	6.8	-3.1	-19.4
	SM3 [kNm/m]	0.9	2.9	0.0	0.0	-0.3
Section E	SF1 [kN/m]	291.5	40.4	4.2	457.1	-11.8
	SF2 [kN/m]	118.0	9.8	0.0	-32.6	-0.3
	SF3 [kN/m]	6.8	2.8	0.2	1.8	-0.1
	SM1 [kNm/m]	7.7	1.6	6.1	-8.6	-4.5
	SM2 [kNm/m]	-22.4	-3.8	6.8	-2.3	-18.5
	SM3 [kNm/m]	0.4	0.0	0.0	0.0	0.0

Table 9.2: Load combination axis 6 (S1)

		ULSa-TR	ULSa-TE	ULSb-TR	ULSb-TE
Section A	SF1 [kN/m]	-78.5	-79.0	-187.8	-186.6
	SF2 [kN/m]	-114.3	-108.9	-98.6	-97.6
	SF3 [kN/m]	-192.4	-193.0	-173.2	-173.0
	SM1 [kNm/m]	31.5	31.5	29.4	28.4
	SM2 [kNm/m]	105.9	84.5	93.3	86.8
	SM3 [kNm/m]	-0.8	-0.1	-0.6	-0.4
Section B	SF1 [kN/m]	504.9	475.1	446.8	438.2
	SF2 [kN/m]	79.6	74.5	67.2	65.7
	SF3 [kN/m]	3.7	-17.4	4.1	-2.0
	SM1 [kNm/m]	12.1	15.0	12.8	12.5
	SM2 [kNm/m]	20.8	23.3	20.6	20.1
	SM3 [kNm/m]	0.4	-1.3	0.3	-0.1
Section C	SF1 [kN/m]	1006.3	924.5	929.4	902.8
	SF2 [kN/m]	-10.7	-0.1	-14.0	-10.3
	SF3 [kN/m]	161.7	116.8	148.7	134.6
	SM1 [kNm/m]	6.8	8.7	8.5	7.7
	SM2 [kNm/m]	-0.2	1.6	3.1	1.8
	SM3 [kNm/m]	1.1	-1.0	1.0	0.4
Section D	SF1 [kN/m]	1101.6	1004.6	1021.7	990.0
	SF2 [kN/m]	7.5	11.6	1.0	2.7
	SF3 [kN/m]	-148.7	-117.1	-135.8	-125.8
	SM1 [kNm/m]	5.8	9.5	8.2	7.5
	SM2 [kNm/m]	-16.7	-7.2	-12.2	-11.4
	SM3 [kNm/m]	4.5	0.7	4.1	2.9
Section E	SF1 [kN/m]	837.1	784.7	788.6	772.5
	SF2 [kN/m]	116.5	102.8	96.9	92.9
	SF3 [kN/m]	13.4	9.8	12.0	10.9
	SM1 [kNm/m]	-2.0	1.8	1.4	0.7
	SM2 [kNm/m]	-51.9	-39.8	-42.4	-40.8
	SM3 [kNm/m]	0.5	0.5	0.4	0.4

Table 9.3: Assumed worst traffic load and temperature load (S1)

	Section A	Section B	Section C	Section D	Section E
Traffic	Traffic_2	Traffic_1*	Traffic_1*	Traffic_1*	Traffic_1*
Temperature	Temp_C	Temp_C	Temp_C	Temp_C	Temp_C

*Traffic load located $0.33 \cdot L_{span}$ away from the column axis in order to generate large tensile forces in the longitudinal direction.

9.1.2 Zero bending moment span 6 (S2)

Table 9.4: Forces zero bending moment span 6 (S2)

		Self-weight	Traffic	Temperature	ASR	ASR transverse
Section A	SF1 [kN/m]	17.1	-44.4	0.2	-928.0	-1.7
	SF2 [kN/m]	3.0	-3.2	0.0	0.0	0.2
	SF3 [kN/m]	-280.4	-16.4	2.3	36.0	-6.8
	SM1 [kNm/m]	12.3	1.7	3.7	-7.9	0.4
	SM2 [kNm/m]	60.0	15.1	1.4	-1.0	2.2
	SM3 [kNm/m]	-0.6	1.8	1.2	0.2	0.3
Section B	SF1 [kN/m]	74.9	-39.4	0.0	70.5	0.2
	SF2 [kN/m]	-16.5	-7.8	-0.2	-4.0	-1.3
	SF3 [kN/m]	-102.3	9.3	1.4	28.0	-5.2
	SM1 [kNm/m]	4.7	-12.5	4.2	-7.6	-1.4
	SM2 [kNm/m]	22.8	-21.1	4.2	-1.6	-6.6
	SM3 [kNm/m]	-3.2	-0.1	0.0	0.8	-0.5
Section C	SF1 [kN/m]	36.2	-94.5	0.2	395.2	0.4
	SF2 [kN/m]	7.4	9.9	0.2	-5.4	-0.2
	SF3 [kN/m]	115.7	51.8	-3.3	-9.7	-6.9
	SM1 [kNm/m]	2.4	1.9	-7.2	-6.9	-2.6
	SM2 [kNm/m]	10.3	22.1	-9.6	-1.9	-12.8
	SM3 [kNm/m]	-2.7	-1.9	0.0	0.5	-0.4
Section D	SF1 [kN/m]	34.2	-97.4	0.0	448.0	0.3
	SF2 [kN/m]	11.6	9.2	0.5	-7.2	0.2
	SF3 [kN/m]	-167.2	-53.1	2.8	26.3	6.0
	SM1 [kNm/m]	0.3	0.9	-9.3	-9.3	-3.6
	SM2 [kNm/m]	0.0	20.8	-10.7	-2.7	-17.9
	SM3 [kNm/m]	1.7	1.6	0.0	0.0	-0.5
Section E	SF1 [kN/m]	69.5	-46.2	-0.9	453.9	-2.3
	SF2 [kN/m]	-4.5	-11.2	0.9	-8.0	1.9
	SF3 [kN/m]	31.4	3.1	0.5	1.6	1.4
	SM1 [kNm/m]	-4.6	-20.2	-9.3	-9.3	-3.5
	SM2 [kNm/m]	-22.6	-33.4	-10.7	-2.7	-18.0
	SM3 [kNm/m]	0.5	0.2	0.0	0.0	0.1

Table 9.5: Load combination section with zero bending moment span 6 (S2)

		ULSa-TR	ULSa-TE	ULSb-TR	ULSb-TE
Section A	SF1 [kN/m]	-967.8	-909.8	-965.7	-947.9
	SF2 [kN/m]	-0.5	3.7	-0.6	0.6
	SF3 [kN/m]	-314.6	-290.9	-269.0	-262.5
	SM1 [kNm/m]	8.9	10.4	9.8	9.1
	SM2 [kNm/m]	89.8	71.6	80.4	74.4
	SM3 [kNm/m]	2.2	1.0	3.0	2.3
Section B	SF1 [kN/m]	101.7	156.8	98.3	114.1
	SF2 [kN/m]	-35.2	-24.5	-31.3	-28.2
	SF3 [kN/m]	-81.8	-93.4	-67.2	-70.9
	SM1 [kNm/m]	-21.1	0.6	-15.9	-10.9
	SM2 [kNm/m]	-11.5	22.2	-7.4	1.1
	SM3 [kNm/m]	-3.5	-3.4	-3.0	-3.0
Section C	SF1 [kN/m]	314.4	437.5	318.6	356.4
	SF2 [kN/m]	15.8	3.1	13.9	9.9
	SF3 [kN/m]	183.8	113.2	158.7	137.9
	SM1 [kNm/m]	-4.3	-14.0	-10.6	-11.4
	SM2 [kNm/m]	25.9	-12.4	14.5	5.6
	SM3 [kNm/m]	-5.5	-3.0	-4.9	-4.1
Section D	SF1 [kN/m]	361.0	487.6	365.6	404.6
	SF2 [kN/m]	18.3	6.8	16.0	12.3
	SF3 [kN/m]	-229.0	-157.2	-196.4	-175.1
	SM1 [kNm/m]	-11.4	-21.9	-19.0	-19.3
	SM2 [kNm/m]	6.4	-31.3	-4.2	-12.5
	SM3 [kNm/m]	3.5	1.5	3.1	2.5
Section E	SF1 [kN/m]	471.5	530.6	464.9	483.4
	SF2 [kN/m]	-25.8	-10.3	-23.3	-18.8
	SF3 [kN/m]	43.1	39.6	38.5	37.3
	SM1 [kNm/m]	-44.4	-27.4	-49.1	-41.0
	SM2 [kNm/m]	-90.1	-57.4	-92.0	-78.6
	SM3 [kNm/m]	1.0	0.7	0.9	0.8

Table 9.6: Assumed worst traffic load and temperature load (S2)

	Section A	Section B	Section C	Section D	Section E
Traffic	Traffic_5	Traffic_3	Traffic_5	Traffic_5	Traffic_1
Temperature	Temp_C	Temp_C	Temp_H	Temp_H	Temp_H

9.1.3 Mid-span between axis 6 and 7 (S3)

Table 9.7: Forces mid-span between axis 6 and 7 (S3)

		Self-weight	Traffic	Temperature	ASR	ASR transverse
Section A	SF1 [kN/m]	-366.7	-87.7	2.3	-871.9	-7.4
	SF2 [kN/m]	41.2	1.2	-0.5	-3.3	1.2
	SF3 [kN/m]	27.8	2.2	0.2	10.6	0.7
	SM1 [kNm/m]	3.1	1.4	3.7	-7.9	-0.1
	SM2 [kNm/m]	52.2	17.3	1.6	1.1	0.0
	SM3 [kNm/m]	0.1	0.8	0.0	-0.2	0.0
Section B	SF1 [kN/m]	-281.8	-55.5	0.5	-554.0	-2.1
	SF2 [kN/m]	-20.2	-4.4	0.2	11.4	-1.4
	SF3 [kN/m]	12.9	0.1	0.2	-5.2	0.9
	SM1 [kNm/m]	-3.0	-13.5	4.2	-7.9	-1.4
	SM2 [kNm/m]	21.0	-23.9	4.0	-2.0	-6.8
	SM3 [kNm/m]	0.4	1.4	0.0	-0.2	0.0
Section C	SF1 [kN/m]	-290.3	-152.3	-1.6	487.5	5.7
	SF2 [kN/m]	-16.0	19.8	0.7	16.5	-3.3
	SF3 [kN/m]	-9.1	7.4	-0.2	-8.8	0.2
	SM1 [kNm/m]	-1.4	-0.2	4.4	-7.0	-2.2
	SM2 [kNm/m]	17.8	16.9	5.6	-4.1	-11.5
	SM3 [kNm/m]	0.3	1.3	0.0	0.0	0.0
Section D	SF1 [kN/m]	-297.0	-157.9	4.2	535.6	9.8
	SF2 [kN/m]	-27.2	18.9	-1.2	21.1	-3.1
	SF3 [kN/m]	18.1	7.6	-0.5	9.9	0.4
	SM1 [kNm/m]	-6.4	-1.7	-9.3	-9.1	-3.2
	SM2 [kNm/m]	0.0	15.4	-10.7	-3.0	-17.1
	SM3 [kNm/m]	-0.1	1.2	0.0	-0.2	0.0
Section E	SF1 [kN/m]	-241.7	-104.9	3.5	525.2	8.9
	SF2 [kN/m]	-53.5	-2.7	-0.9	24.1	-3.0
	SF3 [kN/m]	0.4	0.3	0.0	2.1	0.2
	SM1 [kNm/m]	-11.1	-22.2	-9.3	-9.2	-3.2
	SM2 [kNm/m]	-23.5	-36.2	-10.7	-2.9	-17.3
	SM3 [kNm/m]	0.0	-0.2	0.0	0.0	0.0

Table 9.8: Load combination mid-span between axis 6 and 7 (S3)

		ULSa-TR	ULSa-TE	ULSb-TR	ULSb-TE
Section A	SF1 [kN/m]	-1415.0	-1298.7	-1349.4	-1314.3
	SF2 [kN/m]	46.8	44.8	40.2	39.7
	SF3 [kN/m]	46.1	43.5	41.9	41.0
	SM1 [kNm/m]	-2.6	-0.7	-0.2	-0.8
	SM2 [kNm/m]	83.6	62.8	75.4	68.4
	SM3 [kNm/m]	1.0	-0.1	0.9	0.5
Section B	SF1 [kN/m]	-957.9	-879.7	-904.1	-881.9
	SF2 [kN/m]	-19.4	-13.0	-15.3	-13.5
	SF3 [kN/m]	10.7	10.8	8.9	8.9
	SM1 [kNm/m]	-31.7	-8.6	-25.1	-19.7
	SM2 [kNm/m]	-18.1	19.3	-13.3	-3.8
	SM3 [kNm/m]	2.2	0.3	1.9	1.3
Section C	SF1 [kN/m]	-38.6	157.7	18.8	79.8
	SF2 [kN/m]	20.5	-4.5	21.5	13.6
	SF3 [kN/m]	-9.4	-19.3	-9.0	-12.0
	SM1 [kNm/m]	-11.1	-6.4	-7.3	-7.2
	SM2 [kNm/m]	26.8	10.5	27.0	20.2
	SM3 [kNm/m]	2.0	0.3	1.9	1.3
Section D	SF1 [kN/m]	-1.4	208.0	62.3	125.4
	SF2 [kN/m]	11.3	-14.4	12.5	5.0
	SF3 [kN/m]	41.0	30.6	37.1	34.1
	SM1 [kNm/m]	-21.9	-29.0	-28.2	-27.5
	SM2 [kNm/m]	-0.1	-30.8	-10.2	-16.4
	SM3 [kNm/m]	1.2	-0.3	1.1	0.7
Section E	SF1 [kN/m]	119.8	259.6	169.3	211.3
	SF2 [kN/m]	-43.9	-41.4	-36.4	-35.3
	SF3 [kN/m]	3.2	2.8	3.1	3.0
	SM1 [kNm/m]	-54.0	-34.5	-57.6	-48.7
	SM2 [kNm/m]	-94.3	-57.9	-95.7	-81.2
	SM3 [kNm/m]	-0.3	0.0	-0.2	-0.2

Table 9.9: Assumed worst traffic load and temperature load (S3)

	Section A	Section B	Section C	Section D	Section E
Traffic	Traffic_5	Traffic_4	Traffic_5	Traffic_5	Traffic_1
Temperature	Temp_C	Temp_C	Temp_C	Temp_H	Temp_H

9.1.4 Axis 9 (S4)

Table 9.10: Forces axis 9 (S4)

		Self-weight	Traffic	Temperature	ASR	ASR transverse
Section A	SF1 [kN/m]	807.9	-4.1	17.2	-867.3	14.9
	SF2 [kN/m]	-91.0	-5.5	-0.7	27.8	-4.0
	SF3 [kN/m]	-167.6	1.5	-4.7	-62.1	-3.5
	SM1 [kNm/m]	36.2	1.9	4.0	-8.6	0.3
	SM2 [kNm/m]	89.7	14.1	1.2	-2.6	-0.3
	SM3 [kNm/m]	-0.1	0.6	0.0	-0.1	0.1
Section B	SF1 [kN/m]	412.0	26.0	15.8	18.8	1.9
	SF2 [kN/m]	90.1	3.5	0.9	30.4	0.7
	SF3 [kN/m]	-36.4	12.9	2.1	-77.3	-1.4
	SM1 [kNm/m]	20.6	1.1	4.7	-8.3	-1.8
	SM2 [kNm/m]	32.5	1.4	4.2	-1.6	-8.8
	SM3 [kNm/m]	-2.1	1.4	0.0	-0.5	-0.2
Section C	SF1 [kN/m]	549.3	75.4	29.6	276.0	-15.0
	SF2 [kN/m]	30.3	-10.7	-2.3	49.5	4.1
	SF3 [kN/m]	79.7	36.5	7.5	-101.0	-3.6
	SM1 [kNm/m]	13.1	2.4	5.4	-7.9	-3.3
	SM2 [kNm/m]	8.8	4.3	6.5	-1.0	-14.7
	SM3 [kNm/m]	-1.6	1.5	0.0	0.2	-0.1
Section D	SF1 [kN/m]	560.8	88.5	31.5	318.9	-18.8
	SF2 [kN/m]	43.1	-8.6	-2.1	55.8	3.8
	SF3 [kN/m]	-101.9	-24.7	-7.9	11.8	2.9
	SM1 [kNm/m]	14.9	1.8	6.8	-10.9	-3.8
	SM2 [kNm/m]	2.1	-2.6	7.2	-2.5	-16.5
	SM3 [kNm/m]	0.6	2.7	0.0	-0.5	-0.1
Section E	SF1 [kN/m]	323.8	49.5	21.4	355.1	-11.1
	SF2 [kN/m]	130.8	7.1	2.1	43.8	0.6
	SF3 [kN/m]	-11.6	2.7	-1.2	-1.8	0.3
	SM1 [kNm/m]	7.5	1.5	6.8	-10.5	-3.7
	SM2 [kNm/m]	-27.1	-4.0	7.0	-1.8	-16.2
	SM3 [kNm/m]	0.4	0.0	0.0	0.1	0.0

Table 9.11: Load combination axis 9 (S4)

		ULSa-TR	ULSa-TE	ULSb-TR	ULSb-TE
Section A	SF1 [kN/m]	70.9	93.9	-35.6	-34.0
	SF2 [kN/m]	-88.6	-81.5	-74.4	-72.2
	SF3 [kN/m]	-256.2	-263.0	-235.1	-235.7
	SM1 [kNm/m]	36.0	37.3	33.3	32.6
	SM2 [kNm/m]	120.0	101.4	104.7	99.0
	SM3 [kNm/m]	0.7	-0.1	0.6	0.4
Section B	SF1 [kN/m]	530.9	510.3	476.6	466.2
	SF2 [kN/m]	139.6	135.6	126.1	124.7
	SF3 [kN/m]	-102.5	-118.5	-97.9	-103.1
	SM1 [kNm/m]	15.1	18.3	15.5	15.1
	SM2 [kNm/m]	28.9	31.2	27.1	26.6
	SM3 [kNm/m]	-1.2	-3.1	-1.1	-1.7
Section C	SF1 [kN/m]	990.7	922.3	924.5	894.3
	SF2 [kN/m]	74.5	86.1	69.2	73.5
	SF3 [kN/m]	34.5	-5.5	24.9	10.3
	SM1 [kNm/m]	7.0	9.2	9.1	8.1
	SM2 [kNm/m]	0.0	0.9	3.5	1.8
	SM3 [kNm/m]	0.2	-1.7	0.3	-0.3
Section D	SF1 [kN/m]	1060.1	976.5	992.3	956.9
	SF2 [kN/m]	98.0	107.1	90.7	94.1
	SF3 [kN/m]	-134.6	-110.4	-123.2	-113.3
	SM1 [kNm/m]	4.8	9.2	7.8	7.0
	SM2 [kNm/m]	-20.0	-9.4	-14.2	-13.2
	SM3 [kNm/m]	3.6	0.1	3.2	2.2
Section E	SF1 [kN/m]	780.7	737.8	744.3	724.5
	SF2 [kN/m]	204.1	196.9	185.4	182.6
	SF3 [kN/m]	-11.3	-16.0	-10.8	-11.9
	SM1 [kNm/m]	-3.6	1.2	0.5	-0.1
	SM2 [kNm/m]	-54.4	-42.2	-44.3	-42.7
	SM3 [kNm/m]	0.6	0.6	0.5	0.5

Table 9.12: Assumed worst traffic load and temperature load (S4)

	Section A	Section B	Section C	Section D	Section E
Traffic	Traffic_2	Traffic_1*	Traffic_1*	Traffic_1*	Traffic_1*
Temperature	Temp_C	Temp_C	Temp_C	Temp_C	Temp_C

*Traffic load located $0.42 \cdot L_{span}$ away from the column axis in order to generate large tensile forces in the longitudinal direction.

9.1.5 Section with max field moment from self-weight span 9 (S5)

Table 9.13: Forces in section with max field moment (SM1) from self-weight (S5)

		Self-weight	Traffic	Temperature	ASR	ASR transverse
Section A	SF1 [kN/m]	-586.3	-99.5	-45.4	-535.1	-6.0
	SF2 [kN/m]	47.5	2.5	4.2	23.4	0.9
	SF3 [kN/m]	12.2	-0.4	-13.5	-293.8	0.9
	SM1 [kNm/m]	-0.5	0.9	3.0	-6.3	-0.8
	SM2 [kNm/m]	57.6	15.1	1.6	0.7	-3.2
	SM3 [kNm/m]	1.0	-0.9	-0.2	0.1	0.1
Section B	SF1 [kN/m]	-495.3	-108.1	79.0	-381.0	2.3
	SF2 [kN/m]	-16.7	2.0	-6.1	81.2	-1.6
	SF3 [kN/m]	10.5	-6.1	7.0	-343.2	0.9
	SM1 [kNm/m]	-5.9	-14.4	-5.1	-5.7	-1.6
	SM2 [kNm/m]	26.3	-24.1	-6.5	-0.5	-8.6
	SM3 [kNm/m]	1.9	0.2	0.0	0.7	0.2
Section C	SF1 [kN/m]	-490.6	-174.0	-53.1	427.6	7.8
	SF2 [kN/m]	-17.3	24.3	5.4	121.4	-3.5
	SF3 [kN/m]	1.5	-11.3	9.1	-331.3	0.6
	SM1 [kNm/m]	-3.7	-0.7	3.5	-3.5	-2.2
	SM2 [kNm/m]	22.3	16.9	5.1	-1.5	-12.3
	SM3 [kNm/m]	1.3	1.2	0.0	1.3	0.1
Section D	SF1 [kN/m]	-500.3	-181.4	91.8	365.1	11.4
	SF2 [kN/m]	-31.9	23.3	-8.2	155.3	-4.1
	SF3 [kN/m]	14.3	9.4	18.6	-79.4	0.7
	SM1 [kNm/m]	-11.2	-2.3	-7.2	-4.9	-2.8
	SM2 [kNm/m]	-3.6	15.6	-9.8	-1.7	-15.6
	SM3 [kNm/m]	0.8	-1.1	-0.2	-0.3	0.0
Section E	SF1 [kN/m]	-440.9	-128.3	90.9	305.6	11.1
	SF2 [kN/m]	-60.2	0.9	-5.4	172.6	-3.7
	SF3 [kN/m]	2.8	0.3	4.2	16.2	0.1
	SM1 [kNm/m]	-15.8	-22.9	-7.2	-4.9	-2.8
	SM2 [kNm/m]	-27.4	-37.4	-9.8	-1.5	-15.7
	SM3 [kNm/m]	0.1	0.2	0.0	0.1	0.0

Table 9.14: Load combination max field moment (SM1) from self-weight span 9 (S5)

		ULSa-TR	ULSa-TE	ULSb-TR	ULSb-TE
Section A	SF1 [kN/m]	-1344.7	-1260.8	-1283.1	-1243.3
	SF2 [kN/m]	82.2	83.1	78.2	77.2
	SF3 [kN/m]	-279.4	-292.4	-292.0	-291.8
	SM1 [kNm/m]	-6.5	-4.6	-4.1	-4.5
	SM2 [kNm/m]	83.4	65.4	74.5	68.5
	SM3 [kNm/m]	0.2	1.1	-0.1	0.3
Section B	SF1 [kN/m]	-1088.8	-869.3	-940.5	-897.3
	SF2 [kN/m]	63.0	54.3	60.5	59.7
	SF3 [kN/m]	-338.2	-323.2	-333.5	-331.1
	SM1 [kNm/m]	-32.8	-19.2	-34.6	-28.8
	SM2 [kNm/m]	-10.2	14.6	-16.9	-7.3
	SM3 [kNm/m]	3.3	3.1	3.0	3.0
Section C	SF1 [kN/m]	-355.0	-181.9	-306.5	-236.9
	SF2 [kN/m]	129.6	103.4	134.0	124.3
	SF3 [kN/m]	-343.7	-319.9	-335.5	-331.0
	SM1 [kNm/m]	-10.9	-6.5	-7.4	-7.2
	SM2 [kNm/m]	33.8	17.0	32.9	26.1
	SM3 [kNm/m]	4.5	2.9	4.1	3.7
Section D	SF1 [kN/m]	-434.7	-107.0	-268.0	-195.5
	SF2 [kN/m]	144.8	106.4	140.7	131.4
	SF3 [kN/m]	-50.0	-43.6	-38.2	-42.0
	SM1 [kNm/m]	-23.6	-27.8	-27.4	-26.5
	SM2 [kNm/m]	-1.2	-31.2	-10.0	-16.2
	SM3 [kNm/m]	-0.8	0.4	-1.0	-0.6
Section E	SF1 [kN/m]	-357.1	-99.5	-205.5	-154.1
	SF2 [kN/m]	100.8	94.3	105.5	105.1
	SF3 [kN/m]	19.9	23.7	22.8	22.7
	SM1 [kNm/m]	-55.6	-33.1	-56.8	-47.6
	SM2 [kNm/m]	-97.3	-58.5	-97.3	-82.3
	SM3 [kNm/m]	0.5	0.2	0.4	0.4

Table 9.15: Assumed worst traffic load and temperature load (S5)

	Section A	Section B	Section C	Section D	Section E
Traffic	Traffic_5	Traffic_3	Traffic_5	Traffic_5	Traffic_1
Temperature	Temp_C	Temp_H	Temp_C	Temp_H	Temp_H

9.1.6 Section with large in-plane shear forces from ASR (S6)

Table 9.16: Forces in section with max in-plane shear forces (SF3) from ASR (S6)

		Self-weight	Traffic	Temperature	ASR	ASR transverse
Section A	SF1 [kN/m]	-412.1	-46.2	-79.7	-253.1	-6.2
	SF2 [kN/m]	34.9	-1.7	13.7	-229.8	1.9
	SF3 [kN/m]	233.4	16.7	-3.0	-314.0	5.5
	SM1 [kNm/m]	6.5	0.1	2.1	-1.9	-0.5
	SM2 [kNm/m]	75.5	9.2	0.9	5.3	-1.7
	SM3 [kNm/m]	1.3	0.3	0.0	-0.1	0.3
Section B	SF1 [kN/m]	-288.2	-47.1	-56.6	-264.9	2.2
	SF2 [kN/m]	-25.3	-15.5	-18.9	-206.8	1.1
	SF3 [kN/m]	121.7	-19.2	-13.5	-450.5	5.9
	SM1 [kNm/m]	-2.7	-12.7	2.6	-2.3	-1.8
	SM2 [kNm/m]	30.2	-22.5	3.5	1.6	-8.8
	SM3 [kNm/m]	7.0	-1.0	-0.2	0.1	0.7
Section C	SF1 [kN/m]	-283.9	-126.5	139.1	269.6	8.5
	SF2 [kN/m]	7.7	9.5	-19.1	-208.4	-0.3
	SF3 [kN/m]	-73.4	-47.2	-4.4	-382.5	5.9
	SM1 [kNm/m]	-3.3	2.5	-4.7	-2.6	-2.6
	SM2 [kNm/m]	7.1	27.1	-9.6	-3.8	-14.1
	SM3 [kNm/m]	4.3	1.6	0.5	1.1	0.3
Section D	SF1 [kN/m]	-286.3	-131.3	148.4	92.4	10.5
	SF2 [kN/m]	15.5	8.3	-17.7	-292.9	0.6
	SF3 [kN/m]	143.7	48.4	1.9	-83.5	-3.1
	SM1 [kNm/m]	-8.1	1.4	-6.1	-2.4	-3.0
	SM2 [kNm/m]	-6.9	26.3	-11.0	-0.7	-16.2
	SM3 [kNm/m]	0.0	-1.3	-0.2	-0.7	0.1
Section E	SF1 [kN/m]	-222.2	-56.2	96.9	33.9	7.9
	SF2 [kN/m]	-12.1	-22.9	36.3	-325.5	2.6
	SF3 [kN/m]	32.5	4.5	21.7	17.9	1.0
	SM1 [kNm/m]	-12.5	-20.7	-5.8	-2.2	-3.0
	SM2 [kNm/m]	-28.9	-37.9	-9.8	-0.5	-15.7
	SM3 [kNm/m]	0.1	0.4	0.0	0.1	0.0

Table 9.17: Load combination section with large in-plane shear forces (SF3) from ASR (S6)

		ULSa-TR	ULSa-TE	ULSb-TR	ULSb-TE
Section A	SF1 [kN/m]	-797.9	-812.9	-790.6	-772.1
	SF2 [kN/m]	-190.1	-174.0	-184.0	-183.4
	SF3 [kN/m]	-16.7	-43.1	-57.5	-64.2
	SM1 [kNm/m]	5.2	7.2	5.9	5.9
	SM2 [kNm/m]	103.3	91.4	90.9	87.2
	SM3 [kNm/m]	2.1	1.7	1.9	1.7
Section B	SF1 [kN/m]	-660.1	-650.7	-652.7	-633.9
	SF2 [kN/m]	-256.5	-253.7	-264.7	-258.5
	SF3 [kN/m]	-331.5	-318.2	-356.8	-349.1
	SM1 [kNm/m]	-25.0	-4.6	-20.0	-14.9
	SM2 [kNm/m]	-4.0	31.0	-1.2	7.8
	SM3 [kNm/m]	7.5	8.6	6.4	6.8
Section C	SF1 [kN/m]	-212.8	90.7	-46.3	4.3
	SF2 [kN/m]	-187.5	-219.0	-204.9	-208.7
	SF3 [kN/m]	-522.4	-465.4	-510.2	-491.3
	SM1 [kNm/m]	-5.7	-13.7	-9.2	-10.2
	SM2 [kNm/m]	25.5	-19.3	14.1	3.2
	SM3 [kNm/m]	8.4	6.8	8.0	7.4
Section D	SF1 [kN/m]	-397.0	-77.9	-222.2	-169.7
	SF2 [kN/m]	-263.7	-292.2	-281.0	-284.3
	SF3 [kN/m]	141.6	80.5	116.7	97.3
	SM1 [kNm/m]	-12.9	-20.8	-16.7	-17.2
	SM2 [kNm/m]	9.4	-35.8	-1.0	-11.5
	SM3 [kNm/m]	-2.3	-0.8	-2.3	-1.8
Section E	SF1 [kN/m]	-286.8	-116.8	-170.3	-147.8
	SF2 [kN/m]	-366.6	-300.5	-333.4	-324.2
	SF3 [kN/m]	62.1	77.9	74.1	72.3
	SM1 [kNm/m]	-46.5	-25.4	-47.2	-38.9
	SM2 [kNm/m]	-98.7	-59.2	-98.4	-83.2
	SM3 [kNm/m]	0.7	0.2	0.7	0.5

Table 9.18: Assumed worst traffic load and temperature load (S6)

	Section A	Section B	Section C	Section D	Section E
Traffic	Traffic_2	Traffic_3	Traffic_5	Traffic_5	Traffic_1
Temperature	Temp_C	Temp_C	Temp_H	Temp_H	Temp_H

9.1.7 Axis 10 (S7)

Table 9.19: Forces axis 10 (S7)

		Self-weight	Traffic	Temperature	ASR	ASR transverse
Section A	SF1 [kN/m]	-123.2	-6.4	134.7	49.6	-2.3
	SF2 [kN/m]	-226.1	-15.9	55.7	116.1	-6.3
	SF3 [kN/m]	217.3	16.7	-99.0	-116.4	4.3
	SM1 [kNm/m]	11.7	-0.7	-0.7	-0.1	0.2
	SM2 [kNm/m]	94.7	-5.2	1.9	4.6	0.7
	SM3 [kNm/m]	-1.1	-1.2	0.9	0.2	0.6
Section B	SF1 [kN/m]	-36.3	-1.9	-8.9	74.2	0.4
	SF2 [kN/m]	109.4	18.1	21.9	-599.1	2.8
	SF3 [kN/m]	48.7	-3.5	4.9	-253.3	1.9
	SM1 [kNm/m]	-1.1	0.2	0.7	-0.5	-0.6
	SM2 [kNm/m]	33.1	-9.6	3.7	1.6	-9.2
	SM3 [kNm/m]	9.2	-2.1	-0.7	-0.6	1.0
Section C	SF1 [kN/m]	-67.8	-24.9	145.6	51.9	3.6
	SF2 [kN/m]	3.5	-108.1	60.8	-998.0	10.8
	SF3 [kN/m]	-102.7	-55.0	106.9	-75.9	5.5
	SM1 [kNm/m]	-2.7	2.9	-2.3	-0.2	-2.0
	SM2 [kNm/m]	-9.1	15.6	-8.6	-0.3	-15.1
	SM3 [kNm/m]	5.4	2.3	-0.7	0.7	-0.3
Section D	SF1 [kN/m]	-68.3	-24.4	153.1	35.5	4.0
	SF2 [kN/m]	28.2	-99.9	54.5	-1073.8	11.1
	SF3 [kN/m]	121.4	-54.0	-111.8	-12.9	-5.4
	SM1 [kNm/m]	-1.1	2.9	-2.3	-0.1	-1.8
	SM2 [kNm/m]	-2.9	16.8	-8.2	1.0	-15.1
	SM3 [kNm/m]	1.0	-2.3	1.4	-0.4	1.1
Section E	SF1 [kN/m]	-26.1	-2.5	14.9	-0.6	1.0
	SF2 [kN/m]	184.7	26.1	-45.9	-1075.9	4.8
	SF3 [kN/m]	15.8	2.0	8.2	0.6	0.6
	SM1 [kNm/m]	-3.3	0.2	-1.4	-0.3	-0.9
	SM2 [kNm/m]	-30.9	-21.7	-10.3	-0.2	-16.2
	SM3 [kNm/m]	0.5	0.5	-0.5	0.0	-0.3

Table 9.20: Load combination axis 10 (S7)

		ULSa-TR	ULSa-TE	ULSb-TR	ULSb-TE
Section A	SF1 [kN/m]	-103.3	40.3	24.2	26.7
	SF2 [kN/m]	-172.5	-94.5	-90.8	-84.5
	SF3 [kN/m]	161.2	38.8	46.0	39.3
	SM1 [kNm/m]	12.6	12.9	10.4	10.7
	SM2 [kNm/m]	106.9	116.1	95.3	97.3
	SM3 [kNm/m]	-2.1	0.5	-1.0	-0.5
Section B	SF1 [kN/m]	30.4	24.0	28.9	29.7
	SF2 [kN/m]	-447.0	-448.6	-447.7	-454.9
	SF3 [kN/m]	-199.9	-190.5	-203.0	-201.6
	SM1 [kNm/m]	-2.1	-1.7	-1.4	-1.5
	SM2 [kNm/m]	18.0	34.2	17.0	20.8
	SM3 [kNm/m]	8.3	10.3	6.5	7.4
Section C	SF1 [kN/m]	-54.8	123.2	74.3	84.3
	SF2 [kN/m]	-1123.7	-922.4	-1064.8	-1021.5
	SF3 [kN/m]	-260.0	-81.6	-153.5	-131.5
	SM1 [kNm/m]	-1.5	-7.6	-3.3	-4.4
	SM2 [kNm/m]	-5.6	-34.5	-12.7	-18.9
	SM3 [kNm/m]	9.6	5.9	8.0	7.1
Section D	SF1 [kN/m]	-70.8	114.0	64.4	74.1
	SF2 [kN/m]	-1160.1	-975.7	-1110.8	-1070.8
	SF3 [kN/m]	51.1	9.5	-51.2	-29.6
	SM1 [kNm/m]	0.6	-5.5	-1.4	-2.5
	SM2 [kNm/m]	4.4	-25.6	-3.4	-10.1
	SM3 [kNm/m]	-1.1	3.2	0.1	1.0
Section E	SF1 [kN/m]	-32.9	-14.7	-16.8	-15.8
	SF2 [kN/m]	-824.8	-904.6	-891.8	-902.2
	SF3 [kN/m]	22.0	27.5	25.9	25.1
	SM1 [kNm/m]	-4.7	-6.4	-5.4	-5.5
	SM2 [kNm/m]	-80.1	-62.2	-81.5	-72.9
	SM3 [kNm/m]	0.9	-0.2	0.4	0.2

Table 9.21: Assumed worst traffic load and temperature load (S7)

	Section A	Section B	Section C	Section D	Section E
Traffic	Traffic_2	Traffic_3	Traffic_5	Traffic_5	Traffic_1
Temperature	temp_H	temp_C	temp_H	temp_H	temp_H

9.2 Reinforcement

The amount of reinforcement is important for the capacity and affect the utilization ratios to a great extent. Table 9.22 and Table 9.23 contain the amounts of longitudinal and transverse reinforcement, respectively, for all 35 sections. Amounts are based on the original drawings in Appendix A.

Generally, the plates have small amounts of longitudinal reinforcement in all sections of the bridge. However, large amounts of additional reinforcement is located in the plates near the beams in the columns axes. Elgeseter Bridge is designed to have its bearing through T-beams consisting of the beams themselves and the nearby parts of the plates. Additional reinforcement is placed in the plates close to the beams, in sections A, C and D, to absorb the great tensile forces due to the global bending of the superstructure.

The need for additional longitudinal reinforcement in the plates is greatest near the columns axis. Global bending of the bridge causes tensile forces in the upper parts of the T-beams in these sections. Original drawings give amounts of longitudinal reinforcement only in sections above the column axis and in the mid-span. It is assumed that the section corresponding to zero bending moment in the beams, section 2, has the same amount of reinforcement as sections in the column axis, sections 1 and 4. The additional reinforcement is assumed to extend further out in the plates than the considered 1 m wide elements in sections A, C and D, both over columns and in the point of zero bending moment.

However, the additional longitudinal reinforcement does not reach sections B and E, located in the middle of the plates. Table 9.22 shows small amounts of upper and lower reinforcement in the mid-plates, making these sections vulnerable to tensile forces and positive bending moments. Section E is even observed to have no upper reinforcement at all and is therefore among the most critical sections of the bridge.

The amount of longitudinal reinforcement in sections 5, 6 and 7 is assumed to be the same as in the mid-span, section 3. Common for these four sections is that the T-beams, and generally the superstructure, are exposed to negative bending moments from the vertical loads, resulting in compressive forces in the plate. No additional reinforcement was therefore initially needed in upper parts of the T-beams.

Table 9.22: Reinforcement in the longitudinal direction

Section		1	2	3	4	5	6	7
A	Upper reinforcement [mm^2/m]	4243	4243	221	4243	221	221	221
	Lower reinforcement [mm^2/m]	442	442	442	442	442	442	442
B	Upper reinforcement [mm^2/m]	221	221	221	221	221	221	221
	Lower reinforcement [mm^2/m]	442	442	442	442	442	442	442
C	Upper reinforcement [mm^2/m]	4243	4243	221	4243	221	221	221
	Lower reinforcement [mm^2/m]	442	442	442	442	442	442	442
D	Upper reinforcement [mm^2/m]*	4685	4685	664	4685	664	664	664
	Lower reinforcement [mm^2/m]	781	781	781	781	781	781	781
E	Upper reinforcement [mm^2/m]	0	0	0	0	0	0	0
	Lower reinforcement [mm^2/m]	781	781	781	781	781	781	781

*Reinforcement located in the middle of the cross-section, below the tram rails.

The transverse reinforcement is constant along the bridge, and values from Table 9.23 are therefore assumed to be valid for all sections 1-7. However, the reinforcement varies to a great extent over the width of the bridge. Similar to the longitudinal reinforcement, the intensity of transverse reinforcement is increased in parts of the plate that are exposed to tension due to global bending. Tensile forces from transverse bending moments, SM2, typically appear in upper parts of the slabs near the beams and in lower parts in the mid-plates. Section E is also in the transverse direction observed to have no upper reinforcement and is therefore critical. The transverse reinforcement consists of $\phi 16$.

Table 9.23: Reinforcement in the transverse direction

Section		
A	Upper reinforcement [mm^2/m]	1835
	Lower reinforcement [mm^2/m]	709
B	Upper reinforcement [mm^2/m]	643
	Lower reinforcement [mm^2/m]	804
C	Upper reinforcement [mm^2/m]	1166
	Lower reinforcement [mm^2/m]	804
D	Upper reinforcement [mm^2/m]*	766
	Lower reinforcement [mm^2/m]	1539
E	Upper reinforcement [mm^2/m]	0
	Lower reinforcement [mm^2/m]	1915

*Reinforcement located in the middle of the cross-section, below the tram rails.

Chapter 10

Capacity Control in ULS

The capacity control is performed in the ultimate limit state (ULS) for the plates between the beams. The critical sections considered in the capacity control are presented in Section 8.1.

The superstructure is modelled with shell elements in the analysis. A shell is an element subjected to a combination of in-plane forces, bending moments and transverse shear. Common practice is to control the capacity for transverse shear separately. The capacity control is conducted by the Iteration Method where in-plane forces and bending moments are considered simultaneously [1].

10.1 Capacity Control by the Iteration Method

The Iteration Method is a general design method for capacity control of a shell section with given geometry and amounts of reinforcement. M. Hailemichael has developed a program where the Iteration Method is implemented as part of his master's thesis [3]. This program is used in this study, and input parameters are customized to fit the capacity control for Elgeseter Bridge.

The initial strain from ASR in the cross-section is not included in the capacity control. The inner pre-tension effect is assumed to have a small contribution to the capacity. Furthermore, implementing this initial strain in the program is a complicated process, and it is therefore neglected in the program.

10.1.1 Principals in the Iteration Method

This method controls the capacity iteratively. The curvatures and strains are calculated corresponding to the internal stresses in equilibrium with the external section forces. The shell section is divided into n layers, and the equilibrium is iteratively controlled for each layer.

The section forces from Abaqus are presented by the external load vector in Equation (10.1).

$$\mathbf{R} = \begin{bmatrix} N_x \\ N_y \\ N_{xy} \\ M_x \\ M_y \\ M_{xy} \end{bmatrix} \quad (10.1)$$

A general strain vector, $\boldsymbol{\varepsilon}_t$, including both the strains, $\boldsymbol{\varepsilon}_m$, and the curvatures, $\boldsymbol{\kappa}_m$, in the middle plane of the shell element is defined by Equation (10.2).

$$\boldsymbol{\varepsilon}_t = \begin{bmatrix} \boldsymbol{\varepsilon}_m \\ \boldsymbol{\kappa}_m \end{bmatrix} = \begin{bmatrix} \varepsilon_{xm} \\ \varepsilon_{ym} \\ \gamma_{xym} \\ \kappa_x \\ \kappa_y \\ \kappa_{xy} \end{bmatrix} \quad (10.2)$$

The process is based on Kirchhoff's hypothesis, including linear strain distribution over the thickness of the section, which means that the out of plane normal stresses are neglected. This limitation prevents the Iteration Method to be used in analysis with disturbed regions, or complex joints [40].

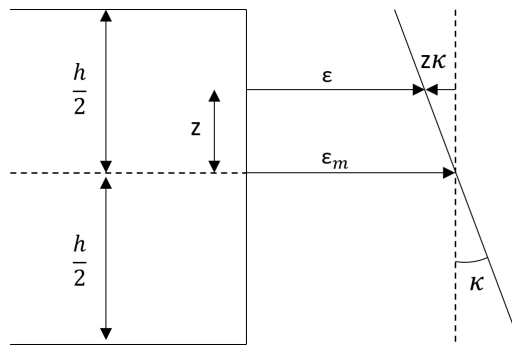


Figure 10.1: Strain distribution in a shell section

Figure 10.1 gives the strain in different heights of the shell section expressed by Equation (10.3).

$$\boldsymbol{\varepsilon} = \begin{bmatrix} \varepsilon_x \\ \varepsilon_y \\ \gamma_{xy} \end{bmatrix} = \boldsymbol{\varepsilon}_m = -z \cdot \boldsymbol{\kappa} = \mathbf{A} \cdot \boldsymbol{\varepsilon}_t = \begin{bmatrix} 1 & 0 & 0 & -z & 0 & 0 \\ 0 & 1 & 0 & 0 & -z & 0 \\ 0 & 0 & 1 & 0 & 0 & -z \end{bmatrix} \cdot \begin{bmatrix} \varepsilon_{xm} \\ \varepsilon_{ym} \\ \gamma_{xym} \\ \kappa_x \\ \kappa_y \\ \kappa_{xy} \end{bmatrix} \quad (10.3)$$

Stiffness matrix based on virtual work:

The principle of virtual work is used to establish the material stiffness matrix \mathbf{K} . A virtual displacement vector is expressed as:

$$\delta \mathbf{r} = a \cdot \delta \boldsymbol{\varepsilon}_t \quad (10.4)$$

The external virtual work and internal virtual work are determined by Equations (10.5) and (10.6), respectively.

$$A_y = \delta \mathbf{r}^T a \mathbf{R} \quad (10.5)$$

$$A_i = \int_V \delta \boldsymbol{\varepsilon}_t^T \boldsymbol{\sigma} dV \quad (10.6)$$

where a is the length of the shell element, $a\mathbf{R}$ is the total external load and V is the volume of the shell element.

The stiffness matrix can be expressed by setting the external virtual work equal to the internal virtual work.

$$A_y = A_i:$$

$$a^2 \delta \boldsymbol{\varepsilon}_t^T \mathbf{R} = \int_V \delta \boldsymbol{\varepsilon}_t^T \mathbf{C} \boldsymbol{\varepsilon} dV = \int_V \delta \boldsymbol{\varepsilon}_t^T \mathbf{A}^T \mathbf{C} \mathbf{A} \boldsymbol{\varepsilon}_t dV = a^2 \delta \boldsymbol{\varepsilon}_t^T \int_{-h/2}^{h/2} \mathbf{A}^T \mathbf{C} \mathbf{A} dz \cdot \boldsymbol{\varepsilon}_t$$

Thus, the equilibrium of the shell element is expressed by Equation (10.7).

$$\mathbf{R} = \int_{-h/2}^{h/2} \mathbf{A}^T \mathbf{C} \mathbf{A} dz \cdot \boldsymbol{\varepsilon}_t = \mathbf{K} \boldsymbol{\varepsilon}_t \quad (10.7)$$

where

$$\mathbf{K} = \int_{-h/2}^{h/2} \mathbf{A}^T \mathbf{C} \mathbf{A} dz \quad (10.8)$$

By conducting a congruence multiplication of the integrand, the stiffness matrix is given by Equation (10.9).

$$\mathbf{K} = \int_{-h/2}^{h/2} \begin{bmatrix} \mathbf{C} & -z\mathbf{C} \\ -z\mathbf{C} & \mathbf{C} \end{bmatrix} dz \quad (10.9)$$

After choosing a suitable material behaviour expressed by \mathbf{C} , the strains and curvature at the middle plane of the shell section can be determined by Equation (10.7). The strain distribution and directions of the principal stresses will vary over the thickness of the shell section. Hence, an exact solution of Equation (10.9) will not be possible. Numerical integration over the thickness is necessary, where the shell section is divided into n layers with thickness $\Delta h = h/n$. The reinforcement is defined as separate layers. Furthermore, the stresses and strains are assumed to be constant in each layer [1].

Material model:

Hooke's law for plane stress is valid for a homogeneous, linear elastic, isotropic material expressed by Equation (10.10).

$$\boldsymbol{\sigma} = \mathbf{C} \boldsymbol{\varepsilon} = \begin{bmatrix} 1 & \nu & 0 \\ \nu & 1 & 0 \\ 0 & 0 & (1-\nu)/2 \end{bmatrix} \boldsymbol{\varepsilon} \quad (10.10)$$

where ν is the poisson's ratio. Equation (10.10) is not valid for non-linear materials due to anisotropic behaviour induced from stresses as shown in Figure 10.2.

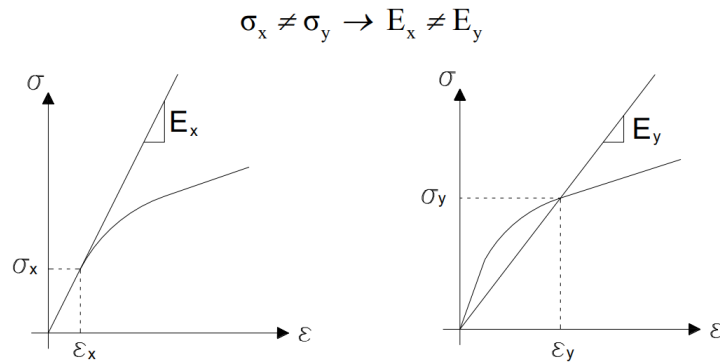


Figure 10.2: Anisotropic material behaviour [40]

Concrete:

An orthotropic material model in the principal directions for the concrete is chosen in order to include cracking when exposed to tension and non-linear behaviour in compression. Thus, the model is only valid in the local principal directions and must be transformed to the global xy -coordinate system. The material model for the concrete is given by Equation (10.11).

$$\boldsymbol{\sigma}_p = \begin{bmatrix} \sigma_1 \\ \sigma_2 \\ \sigma_3 \end{bmatrix} = \frac{1}{1-\nu^2} \begin{bmatrix} E_{11} & \nu E_{12} & 0 \\ \nu E_{12} & E_{22} & 0 \\ 0 & 0 & \frac{(1-\nu)E_{12}}{2} \end{bmatrix} = \mathbf{C}_p \boldsymbol{\varepsilon}_p \quad (10.11)$$

where p represent the principal directions and $E_{12} = 0.5(E_{11} + E_{22})$.

The Young's modulus's E_{11} and E_{22} are the secant modulus's in the two principal directions. These values are equal for a linear elastic problem, resulting in Equation (10.11) becomes Equation (10.10).

It is assumed that the effects in the two principal directions are uncoupled for capacity calculations in the ultimate limit state, resulting in a Poisson's ratio equal to zero. The failure curve in the principal directions is illustrated in Figure, assuming zero tensile capacity of the concrete.

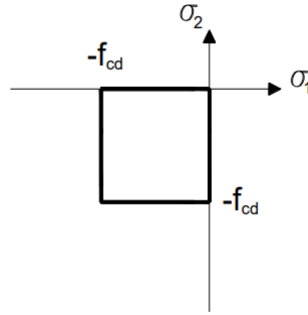


Figure 10.3: Biaxial failure curve for concrete [1]

Reinforcement:

Assuming the reinforcement is placed in the global x- and y directions, the stress-strain relationship can be expressed by Equation (10.12).

$$\boldsymbol{\sigma}_s = \begin{bmatrix} \sigma_{sx} \\ \sigma_{sy} \\ \tau_{sxy} \end{bmatrix} = \begin{bmatrix} E_{sx} & 0 & 0 \\ 0 & E_{sy} & 0 \\ 0 & 0 & 0 \end{bmatrix} \begin{bmatrix} \varepsilon_x \\ \varepsilon_y \\ \gamma_{xy} \end{bmatrix} = \mathbf{C}_s \boldsymbol{\varepsilon} \quad (10.12)$$

where E_{sx} and E_{sy} are the secant modulus for the reinforcement in the two directions, for two one-dimensional stress-strain relationships.

Step by step procedure in the Iteration Method:

The procedure in the Iteration Method can be summed up with the following steps [1]:

1. Determine the external load vector \mathbf{R} , extracted from the FEM analysis.
2. Calculate the initial stiffness matrix for linear elastic, isotropic concrete and linear elastic reinforcement.

Concrete:

$$\mathbf{K}_{c0} = \sum_{i=1}^n \Delta h \mathbf{A}_i^T \mathbf{C}_{0i} \mathbf{A}_i = \Delta h \sum_{i=1}^n \begin{bmatrix} \mathbf{C}_{0i} & -z_i \mathbf{C}_{0i} \\ -z_i \mathbf{C}_{0i} & z_i^2 \mathbf{C}_{0i} \end{bmatrix}$$

Reinforcement:

$$\mathbf{K}_{s0} = \sum_{j=1}^m (A_{sxj} \begin{bmatrix} \mathbf{C}_{0sxj} & -z_j \mathbf{C}_{0sxj} \\ -z_j \mathbf{C}_{0sxj} & z_j^2 \mathbf{C}_{0sxj} \end{bmatrix} + A_{syj} \begin{bmatrix} \mathbf{C}_{0syj} & -z_j \mathbf{C}_{0syj} \\ -z_j \mathbf{C}_{0syj} & z_j^2 \mathbf{C}_{0syj} \end{bmatrix})$$

$$\mathbf{K}_0 = \mathbf{K}_{c0} + \mathbf{K}_{s0}$$

3. Calculate strains and curvatures in the middle plane of the shell:

$$\boldsymbol{\varepsilon}_{t0} = \mathbf{K}_0^{-1} \mathbf{R}$$

4. Find the strains in each layer for both the concrete and the reinforcement, referred to global coordinate system:

$$\boldsymbol{\varepsilon}_{0i} = \mathbf{A}_i \boldsymbol{\varepsilon}_{t0}$$

5. Determine the principal strains and the directions for the concrete layers:

$$\boldsymbol{\varepsilon}_{p0i} = \mathbf{T}_{\varepsilon i} \boldsymbol{\varepsilon}_{0i}$$

where $\mathbf{T}_{\varepsilon i}$ is the strain-transformation matrix from global to local principal directions.

6. Find the principal stresses in each layer:

The principal stresses $\boldsymbol{\sigma}_{p0i}$, depends on the stress-strain relationship. This is where the non-linear material behaviour is taken into account.

7. Transformation of the principal stresses to global coordinate system for each layer:

Concrete:

$$\boldsymbol{\sigma}_{0i} = \mathbf{T}_{\varepsilon i}^T \boldsymbol{\sigma}_{p0i} \quad \mathbf{T}_{\varepsilon}^T = \mathbf{T}_{\sigma}^{-1} \quad \text{due to orthogonality}$$

Reinforcement:

$$\boldsymbol{\sigma}_{s0j} = \mathbf{C}_{s0j} \boldsymbol{\varepsilon}_{0j}$$

8. Calculate the internal load vector as the sum of the concrete and reinforcement contributions:

$$S_0 = \Delta h \sum_{i=1}^n \begin{bmatrix} \sigma_{0i} \\ -z_i \sigma_{0i} \end{bmatrix} + \sum_{j=1}^m \begin{bmatrix} A_{sxj} \cdot \sigma_{sx0} \\ A_{syj} \cdot \sigma_{sy0} \\ 0 \\ -z_j \cdot A_{sxj} \cdot \sigma_{sx0} \\ -z_j \cdot A_{syj} \cdot \sigma_{sy0} \\ 0 \end{bmatrix}$$

9. Calculate the maximum relative deviation between the internal and external load vector:

$$\text{Maxdiff} = \left| \frac{R_k - S_{0k}}{R_k} \right| ; \quad \text{for } k=1,2, \dots,6$$

10. Control the convergence against a chosen convergence criteria, for instance $\beta = 0.01$:

- If $\text{Maxdiff} \leq \beta$, convergence is achieved and the iteration is finished.
- If $\text{Maxdiff} > \beta$, calculate new secant modulus's in the principal directions for each concrete and reinforcement layer.

→ New material matrices: C_{p1i} ; $i=1, \dots, n$

11. Transformation of local material matrices to global coordinate system:

$$C_{1i} = T_{\epsilon i}^T C_{p1i} T_{\epsilon i}$$

Return to step 2 and repeat steps 2-11 until the chosen convergence is achieved.

The Iteration process is visualized in Figure 10.4.

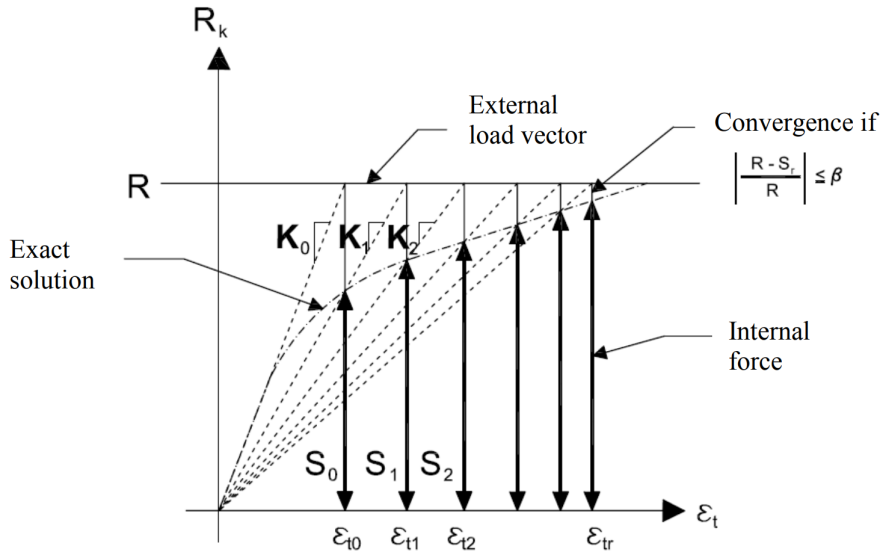


Figure 10.4: Iteration Method [40]

10.1.2 Input to the Program

The input parameters to the program are shown in Figure 10.5. The x-axis corresponds to the longitudinal direction of the bridge. Bending moments are defined with opposite signs compared to the sign convention from Abaqus, shown in Figure 7.6. Positive bending moments in the program correspond to tensile stresses in the lower part of the element. This is included by inserting M_x , M_y and M_{xy} with opposite sign in the capacity program.

The α -values consider the angle between the longitudinal- and transverse reinforcement in each layer. As the reinforcement in Elgeseter Bridge is placed as an orthogonal grid, both α_1 and α_2 is set to 0 degrees. n is the number of layers, β is the convergence criteria, and $maxIt$ is the maximum number of iterations. Chosen values for these parameters are shown in Figure 10.5. The design compressive strength of the concrete is calculated by Equation (10.13) in the capacity program. A compressive strength of 12 MPa is obtained by using $f_{ck} = 25$ MPa, $\alpha = 0.672$ and $\gamma_s = 1.4$. It is normal to assume that the two principal stress directions are uncoupled for capacity calculations in ULS, leading to a Poisson's ratio, ν , equal to zero [1].

$$f_{cd} = \alpha \cdot \frac{f_{ck}}{\gamma_s} \quad (10.13)$$

The screenshot shows the 'Shell Input' window with the following input fields:

- Forces:** Nx, Ny, Nxy, Mx, My, Mxy (all in kN/m).
- Geometry:** h (mm), c1 (mm), c2 (mm).
- Iteration:** n (100), β (0.01), maxIt (1000).
- Reinforcement:** Asx1, Asx2, Asy1, Asy2 (mm²/m); Esx1, Esx2, Esy1, Esy2 (N/mm²); α1, α2 (deg); f_{vk} (340 N/mm²); γ_s (1.25); ε_{ud} (0.01).
- Concrete:** Concrete model (parabola - rectangle); f_{ck} (25 N/mm²); γ_c (1.4); v (0).

A 'Calculate' button is located below the input fields. At the bottom, a 3D diagram shows a rectangular plate with dimensions 1m by 1m and height h. The diagram illustrates the internal force vectors: normal forces (N_x, N_y), shear forces (V_x, V_y), and bending moments (M_{xy}) acting on the plate. A coordinate system (x, y, z) is also shown.

Figure 10.5: Input parameters to the Iteration Method

The values c_1 and c_2 are the distances from the centre of gravity of the reinforcement layer to the closest surface for the lower and upper part, respectively. These distances are calculated by the following equation:

$$c = \frac{\sum(A_{s,i} \cdot y_{s,i})}{\sum A_{s,i}} \quad (10.14)$$

where $A_{s,i}$ is the considered reinforcement layer and $y_{s,i}$ is the distance from the free surface to the centre of gravity of the reinforcement.

Figure 10.6 shows the reinforcement for a typical outer beam in a column axis. As described in Section 4.4, the transverse reinforcement in the plate has a cover equal to 33 mm and a diameter of 16 mm. This results in a distance of 49 mm to the distribution reinforcement in the longitudinal direction, as these tendons are located at the inside of the transverse reinforcement. The beams have a cover of 50 mm, which is the distance to the stirrups ($\phi 13$). Hence, the distance to the additional longitudinal reinforcement is 63 mm from the free surface. Table 10.1a and Table 10.1b summarize the cover for the lower and upper reinforcement, in

addition to the heights used in the capacity control. It is used a full height also in section D, because the cavity from the removed tram rail is recast. The amounts of reinforcement are presented in Table 9.22 and Table 9.23.

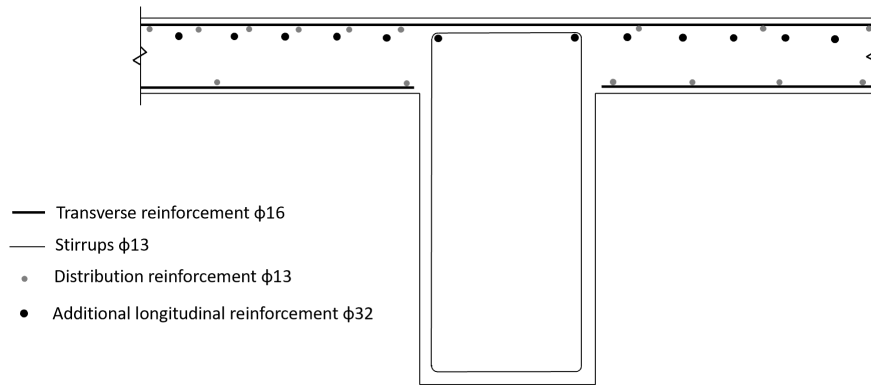


Figure 10.6: Reinforcement types in the plate

Table 10.1: Height and cover used for the different sections

(a) S1,S2,S4				(b) S3 and S5-S7			
Section	c1 [mm]	c2 [mm]	h [mm]	Section	c1 [mm]	c2 [mm]	h [mm]
A	47	67	255	A	47	43	255
B	46	45	280	B	46	45	280
C	46	70	290	C	46	43	290
D	53	99	370	D	53	154	370
E	45	0	380	E	45	0	380

According to NS3473 [23] Section 11.3.6, a simplified stress-strain relation can be used in the capacity control for the reinforcement, here reproduced as Figure 10.7. This relation is used in the program, resulting in a design Young's modulus of 160000 MPa. In comparison, bridges today are designed with a characteristic Young's modulus, in this case equal to 200000 MPa.

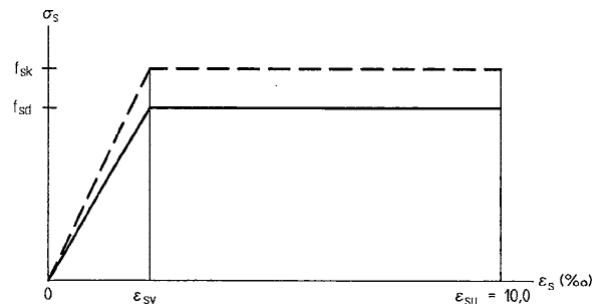


Figure 10.7: Simplified strain-stress relation reinforcement [23]

10.1.3 Output from the Program

Yielding in the reinforcement or compressive failure in the concrete:

From a converged solution in the Iteration Method, the strain level in the reinforcement and the stress in the concrete can be used to evaluate the utilization of the shell section. The critical load combinations are verified against both yielding and failure in the reinforcement and the compressive strength of the concrete. Figure 10.8 illustrates how the utilization ratios are estimated when considering yielding in the reinforcement as a failure criterion. The external section forces, P_{Ed} , are scaled down to a value P_s , by a scaling factor SF_1 , such that all utilization ratios for both materials are below 1.0:

$$P_s = SF_1 \cdot P_{Ed} \quad (10.15)$$

The capacity control for the scaled loads, P_s , results in utilization ratios below 1.0 given as UR_{SF1} . The resulting utilization ratio is obtained by assuming a linear relation also after yielding or failure in the concrete has occurred. Therefore, the resulting utilization ratio is expressed by the utilization ratio of the most critical component:

$$UR_1 = \frac{UR_{SF1}}{SF_1} \quad (10.16)$$

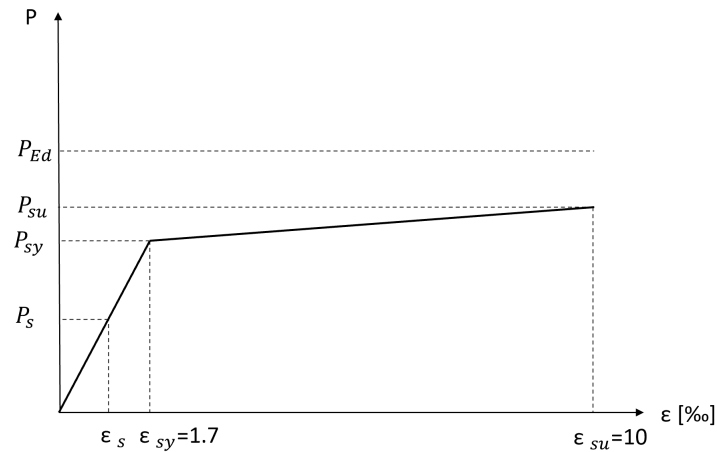


Figure 10.8: Strain development in the reinforcement

Failure strain in the reinforcement or compressive failure in the concrete:

Sections with $UR_1 > 1.0$ are verified considering either failure strain in the reinforcement or compressive failure in the concrete. The area between P_{sy} and P_{su} describes yielding in minimum one reinforcement layer. P_{su} is the maximum load the section can resist before failure in one reinforcement layer or failure in the concrete occurs. The solution from the Iteration Method does not converge for

loads larger than P_{su} as the failure capacity is exceeded. This load level corresponds to a utilization ratio of 1.0 in the most utilized component. P_{Ed} is scaled down by a scaling factor SF_2 until the solution converges.

$$P_{su} = SF_2 \cdot P_{Ed} \quad (10.17)$$

The resulting utilization ratio UR_2 is either limited by the ultimate failure strain of the reinforcement or exceedance of the compressive strength in the concrete. The final utilization ratio is obtained as:

$$UR_2 = \frac{1.0}{SF_2} \quad (10.18)$$

Reduced compressive strength of the concrete:

Some sections are exposed to high compressive forces. According to section 6.5 in EC2 [25], the maximum compressive strength in the concrete should be reduced by Equation (10.19) if the section exhibit tension in the direction normal to the compressive force.

$$\sigma_{Rd,max} = 0.6 \cdot \nu' \cdot f_{cd} \quad (10.19)$$

where

$$\nu' = 1 - \frac{f_{ck}}{250} \quad (10.20)$$

This limitation reduces the capacity of the concrete by 46%, which can be decisive for the capacity of a cross-section. The design values for the reinforcement and concrete used in the capacity control are shown in Table 10.2.

The capacity program does not include the reduction of the compressive strength of the concrete in the iteration process. Implementing this limitation is a complicated and time-consuming process. Reduction of the capacity is however considered by comparing the maximum compressive stress occurring in the shell section with the reduced design compressive strength from Equation (10.19). Even though this simplification does not give the exact utilization, it perceives the reduction of compressive strength in the concrete exposed to both compression and tension.

The utilization of a shell section regarding the concrete is based on the design compressive strength, f_{cd} . A utilization ratio of 1.0 in the concrete is obtained when one of the n layers reaches a stress level equal to the compressive strength. The outermost layer is typically most utilized.

Table 10.2: Design resistance ULS

Property	Sign	Value
Yielding strain reinforcement	ϵ_{sy}	1.7‰
Failure strain reinforcement	ϵ_{su}	10‰
Design compressive strength concrete	f_{cd}	12 MPa
Reduced design compressive strength concrete	$\sigma_{Rd,max}$	6.48 MPa

10.1.4 Results from the Iteration Method

Utilization of critical sections concerning yielding in reinforcement:

Table 10.3 shows the utilization in all critical sections when yielding in the reinforcement is considered as the failure criterion. It is observed that some of the sections also exceed the compressive strength of the concrete. Utilization of the reinforcement in sections where the concrete is the limitation is therefore shown in Table 10.4. UR_{sx1} and UR_{sx2} are the utilization ratios in the longitudinal reinforcement for the lower and upper layer, respectively. It is equivalent for the reinforcement in the transverse direction. UR_c corresponds to the utilization ratios of the compressive strength of the concrete, while $UR_{c,red}$ corresponds to the reduced compressive strength of the concrete.

Some sections have yielding in more than one reinforcement layer, as Table 10.3 illustrates. Yielding in the reinforcement may result in formation of plastic hinges in the cross-section. What happens with the different layers after this point is somewhat uncertain, as forces will redistribute. Nevertheless, this indicates the most utilized reinforcement layers. Cracking of the concrete will also result in a smaller height of the compression zone, which will increase the compressive stresses in the section.

Table 10.3: Utilization of critical sections wrt. yielding in the reinforcement and compressive failure of the concrete

Section	Load combination	Utilization					
		URsx1	URsx2	URsy1	URsy2	URc	URc.red
1A	ULSa-TR	0.06	0.29	0.29	1.31	1.36	-
1B	ULSa-TR	1.58	5.26	0.04	0.84	0.27	0.51
1C	ULSa-TR	3.27	0.69	0.68	0.29	0.56	1.04
1D	ULSa-TR	2.09	0.59	0.55	0.18	0.13	0.25
1E	ULSa-TR	-	-	-	-	-	-
2A	ULSa-TR	0.19	0.03	0.22	1.23	1.13	-
2B	ULSa-TE	0.73	2.11	0.05	1.06	0.32	0.58
2C	ULSa-TE	2.15	0.35	0.75	0.16	0.66	-
2D	ULSa-TE	1.42	0.30	0.57	0.13	0.37	-
2E	ULSa-TE	-	-	-	-	-	-
3A	ULSa-TR	0.87	0.31	0.24	0.97	0.73	-
3B	ULSa-TR	0.08	0.25	0.34	0.04	0.48	-
3C	ULSa-TE	0.95	0.83	0.02	0.20	0.08	0.16
3D	ULSa-TE	0.89	0.39	0.29	0.09	0.24	-
3E	ULSa-TE	1.59	-	0.34	-	0.87	1.61
4A	ULSa-TR	0.01	0.43	0.30	1.56	1.52	-
4B	ULSa-TR	1.71	6.25	0.24	1.84	0.24	0.45
4C	ULSa-TR	3.48	0.64	0.38	0.17	0.79	1.47
4D	ULSa-TR	2.02	0.57	0.62	0.24	0.14	0.27
4E	ULSa-TR	-	-	-	-	-	-
5A	ULSa-TR	0.23	0.24	0.17	1.04	0.84	-
5B	ULSa-TE	0.01	0.15	0.24	0.82	0.41	0.76
5C	ULSa-TR	0.57	0.23	0.46	1.01	0.32	0.60
5D	ULSa-TE	0.29	0.08	0.40	0.15	0.26	-
5E	ULSa-TR	0.19	-	0.72	-	0.44	-
6A	ULSa-TR	0.17	0.14	0.40	0.98	0.89	-
6B	ULSa-TR	0.19	0.18	0.26	0.03	0.46	-
6C	ULSa-TE	2.26	1.58	1.55	0.39	0.38	0.70
6D	ULSa-TE	0.25	0.07	0.11	0.02	0.26	-
6E	ULSa-TR	0.20	-	0.37	-	0.51	-
7A	ULSa-TE	0.20	1.56	0.29	1.21	1.23	-
7B	ULSa-TE	0.66	0.41	0.07	0.18	0.40	0.73
7C	ULSa-TR	0.32	0.02	0.13	0.18	0.34	0.63
7D	ULSa-TE	0.26	0.33	0.08	0.13	0.31	0.58
7E	ULSa-TR	0.01	-	0.05	-	0.46	-

Table 10.4: Utilization of the reinforcement wrt. yielding when failure in the concrete occurs

Section	Load combination	Utilization			
		UR _{sx1}	UR _{sx2}	UR _{sy1}	UR _{sy2}
1A	ULSa-TR	0.044	0.213	0.213	0.963
2A	ULSa-TR	0.168	0.027	0.195	1.088
4A	ULSa-TR	0.006	0.283	0.197	1.026
7A	ULSa-TE	0.163	1.268	0.236	0.984

Utilization of critical sections concerning ultimate failure in the cross-section:

Table 10.5 shows the utilization ratios of the cross-sections based on the ultimate failure strain of the reinforcement and crushing of the concrete. The *utilization* in the table concerns the ratio between external forces and the capacity. The utilization is obtained as one of the criteria in the *Failure limitation* reaches 1.0. *URs* and *URc* correspond to the utilization of the reinforcement and concrete, respectively. *URc.red* corresponds to the utilization of the reduced compressive strength when the failure limitation is reached. Reduced compressive strength values are not used as a failure limitation due to the simplification in the program. However, it highlights the sections where the compressive strength of the concrete might be particularly critical.

Table 10.5: Utilization of critical sections concerning ultimate failure in the cross-section

Section	Load combination	Utilization UR	Failure limitation		URc.red
			UR _s	UR _c	
1A	ULSa-TR	1.26	0.37	1.0	-
1B	ULSa-TR	4.44	1.0	0.45	-
1C	ULSa-TR	1.82	0.91	1.0	1.85
1D	ULSa-TR	1.18	0.95	1.0	1.85
2A	ULSa-TR	1.18	0.58	1.0	-
2B	ULSa-TE	1.55	1.0	0.48	-
2C	ULSa-TE	1.29	0.77	1.0	-
2D	ULSa-TE	0.85	0.82	1.0	-
3E	ULSa-TE	1.57	1.0	0.84	1.55
4A	ULSa-TR	1.48	0.46	1.0	-
4B	ULSa-TR	5.08	1.0	0.50	-
4C	ULSa-TR	1.72	0.89	1.0	1.83
4D	ULSa-TR	1.16	0.90	1.0	1.82
5A	ULSa-TR	0.99	0.91	1.0	-
5C	ULSa-TR	0.93	1.0	0.69	1.27
6C	ULSa-TE	2.15	1.0	0.21	-
7A	ULSa-TE	1.21	0.98	1.0	-

for both layers. All the reinforcement within a layer is assumed to yield if the layer is cracked. Hence, the utilization ratio will be the same for the reinforcement in the two directions. This gives an estimate of the most utilized reinforcement in each layer of the shell element. Only sections where the reinforcement yields are verified.

Principal of the Membrane Method:

Positive forces from Abaqus are shown in Figure 10.10a. These are in the Membrane Method treated as equivalent membrane forces as shown in Figure 10.10b.

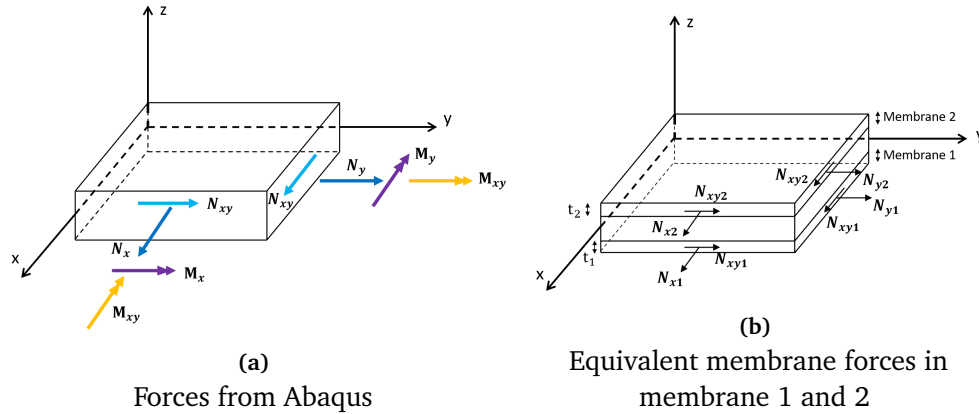


Figure 10.10: Principals Membrane Method

The internal lever arm is given by the following equation:

$$z = h - 0.5(t_1 + t_2) \tag{10.21}$$

where h is the height of the shell section.

Forces in membrane 1 and 2 are given by Equations (10.22) and (10.23), respectively,

$$n_{i1} = k_1 \cdot N_i - \frac{M_i}{z} \quad ; \quad \text{for } i = x, y, xy \tag{10.22}$$

$$n_{i2} = k_2 \cdot N_i + \frac{M_i}{z} \quad ; \quad \text{for } i = x, y, xy \tag{10.23}$$

where

$$k_1 = \frac{h - t_2}{2h - t_1 - t_2} \quad ; \quad k_2 = 1 - k_1$$

The following procedure can be used to determine the thicknesses of membrane 1 and 2:

1. Begin with $t_1 = t_2 = h/2 \rightarrow k_1 = k_2 = 0.5$
2. Calculate the membrane forces in each layer by Equations (10.22) and (10.23).
3. Determine the largest principal force in each layer for a homogeneous, isotropic, linear elastic material:

$$n_{11}^i = \frac{n_{xi} + n_{yi}}{2} + \sqrt{\left(\frac{n_{xi} - n_{yi}}{2}\right)^2 + n_{xyi}^2} \quad ; \quad i=1,2$$

If $n_{11}^i > 0$: The membrane is cracked and the tensile forces must be taken by the reinforcement.

4. The thickness of the layer is dependent of whether the layer is cracked or not, leading to the following cases:

- Both membranes are uncracked:

$$t_1 = t_2 = h/2$$

- Both membranes are cracked:

$$t_1 = 2c_1 \quad ; \quad t_2 = 2c_2$$

- One membrane is cracked and one is uncracked:

Cracked layer 1: $t_1 = 2c_1$; uncracked layer 2: $t_2 = h/2$

$$k_1 = \frac{0.25h}{0.75h - c_1} \quad ; \quad k_2 = 1 - k_1$$

where c is the distance from the free surface to the axis of gravity of the reinforcement in the current layer.

5. If a membrane is cracked; calculate new membrane forces according to Equations (10.22) and (10.23).

The two membranes are controlled separately using the compression field theory. It is assumed yielding in the reinforcement for both directions if the membrane layer is cracked. The crack angle is calculated by Equation (10.24).

$$\tan^2 \phi + \left(\frac{N_x}{N_{xy}} - \frac{N_y}{N_{xy}} \cdot \frac{A_{sx}}{A_{sy}} \right) \cdot \tan \phi - \frac{A_{sx}}{A_{sy}} = 0 \quad (10.24)$$

The internal forces in each membrane are calculated from the compression field theory. Utilization of the reinforcement in the Membrane Method is verified by

the yielding stress.

Verification of the capacity program:

The deviation between results provided from the Membrane Method and the Iteration Method is shown in Table 10.6. As_1 and As_2 correspond to the reinforcement in the lower and upper layer, respectively. The correspondence between the two methods is considered good for sections where both the upper and lower parts are assumed cracked, as shown in section 1B and 1D. However, the deviation is observed to be larger in sections where one layer is assumed uncracked, like in section 2A and 7A. The reinforcement located in the uncracked layer is exposed to compressive strains and will therefore not be utilized, as illustrated by "-" in Table 10.6. Detailed calculations are shown in Appendix D.

Table 10.6: Deviation between Iteration Method and Membrane Method

Section	Load combination	Deviation [%]	
		As_1	As_2
1B	ULSa-TR	0.1	1.3
1D	ULSa-TR	6.2	4.4
2A	ULSa-TR	-	19.1
7A	ULSa-TE	-	20.6

Equilibrium between external and internal forces in the Iteration Method is obtained by optimizing the strain distribution in an iterative manner. In contrast, the Membrane Method considers the two layers independently with uniform strains corresponding to the strain value in the middle of each layer. Hence, the strain compatibility is not included. Comparing the utilization of the concrete will therefore be inconvenient. However, the Iteration Method is considered to give more reliable results than the Membrane Method. The verification of the capacity program is therefore assumed to be satisfactory, despite the observed deviations in some sections between the two methods.

Chapter 11

Discussion

This chapter discusses interesting aspects regarding the thesis and results obtained from the capacity control. Critical sections are referred to by their section-ID, illustrated in Figure 8.1 and Figure 8.2.

11.1 ASR Effects

In this thesis, the impact of ASR has shown a significant influence on the capacity of the bridge, mainly caused by additional load effects. In order to determine these loads effects, the expansion of the bridge must be assumed. Based on measured expansions in the bridge and its estimated future development, a total elongation of 200 mm is assumed due to ASR. Uncertainties are related to the distribution of the expansion in the bridge. The outer beams and the plates are observed to be more exposed to ASR than the inner parts. The strain distribution used to model the ASR expansions along the whole bridge is based on the measured total elongation and is assumed to be constant in the longitudinal direction. However, the actual expansion may vary locally in the cross-section and along the bridge due to different access to humidity and variation in aggregates. Furthermore, if the concrete is cracked because of external loads or other degradation mechanisms, conditions for increased ASR development are present, as discussed in Chapter 2.

Only the concrete expands when a reinforced concrete structure is exposed to ASR. The reinforcement prevents some free expansion, generating tension in the reinforcement and compression in the concrete. The internal load effects from ASR can be treated as a pre-tension effect in the reinforcement. Yielding in the reinforcement occurs for smaller tensile strains because of the initial state. Including the initial strain will probably result in a smaller capacity in some sections. However, the pre-tension effect is assumed to have a small impact on the total capacity. Due to the many uncertainties regarding ASR and the lack of ability to control the initial strain in the capacity program, the internal load effects are not included in the capacity control.

In order to calculate the equivalent temperature loads from ASR, internal restraining contributions from the reinforcement must be considered for each element. Evaluating the amount of reinforcement in all the shell elements would have been a comprehensive and time-consuming process. The ASR loads in the longitudinal direction are therefore based on Aas-Jakobsen's report regarding Elgeseter Bridge from 2020 [17]. Transforming the equivalent temperature loads from the frame model to a shell model was a significant part of the modelling process in this thesis. Results from the Abaqus model indicate that the ASR loads are implemented correctly. Aas-Jakobsen's loads are based on a total elongation of 200 mm in the bridge, and the Abaqus model resulted in a total elongation of 200.8 mm.

ASR in the transverse direction is included as an individual load model in the analysis. The resulting forces from transverse ASR are in most cases observed to be small compared to contributions from other loads. Considerable transverse bending moments are however observed especially in sections C, D and E. The negative bending moments are observed to be beneficial in sections D and E, as they provide compression forces in upper parts containing small amounts of reinforcement. However, including ASR in the capacity control is considered unfavourable in most cases due to the much greater effects from the longitudinal expansions.

Stress-dependent expansion of concrete is not included in the analysis. As discussed in Section 2.1, it is proposed by some researchers that the ASR expansion might stop if the compressive stresses are sufficiently large in the same direction as the expansion. Less expansion of the outer parts would result in smaller axial forces both in the inner and outer parts.

11.2 Modelled Stiffness

The Abaqus model is made as close to the reality as possible. However, several simplifications have been conducted during the establishment of the model. Some properties of the bridge are even unknown, and assumptions have been necessary to accomplish a finite element analysis.

Elgeseter Bridge is in this thesis modelled only in stage I, even though several wide cracks have been observed in the beams and columns. None of the performed inspections has so far reported any cracks of considerable size in the plates. However, resulting forces from the stage I FEA indicate that several parts of the plate might be in a cracked state. Potential cracks in upper parts of the plate can be hard to spot as the concrete is hidden under the wearing course.

Stage I means non-cracked cross-sections where the concrete is assumed to have tensile strength. A stage I section generally absorbs greater forces than a stage II section as it is stiffer. Thus, establishing an uncracked stage I model can be con-

sidered somehow conservative regarding the calculation of dimensioning forces.

Stage II might be assumed to represent the stiffness of sections with the largest observed cracks in the beams. Cracked sections of stage II have reduced stiffness and are consequently more flexible. Sections with yielded reinforcement even experience a plastic behaviour. Introducing cracks and plastic hinges reduces the global restraint moment and consequently also the axial forces in the plate. However, a larger global curvature generates more significant bending moments in the plate.

Non-linearities like cracks can be modelled in different ways by reducing the stiffness either of specific areas where cracks are observed or by an all-over reduction. Uncertainties are related to the diversity of cracks and the depth of the already observed cracks. The actual stiffness is probably varying between stage I and stage II, both in the transverse direction and along the bridge. One reasonably accurate approach would probably be to generally use stage I stiffness and implement stage II stiffness in the cracked areas.

11.3 Modelled Mesh and Loads

Choosing between different load models and load locations is challenging when modelling with shell elements. The Iteration Method includes six forces and the amounts of upper and lower reinforcement in both directions. Determining the critical combination of all six force contributions from all five loads is therefore difficult. A load can e.g. generate an unfavourable contribution to the axial force in the longitudinal direction, and at the same time, give a favourable bending moment reducing tensile forces in areas of less reinforcement. However, in most sections, the critical case is obtained by combining loads generating large tensile forces either by axial forces or by bending moments.

Element sizes are chosen with regard to Aas-Jakobsen's frame model from their report in 2020 [17]. Using the same element lengths is favourable as it makes it possible to implement their already calculated ASR loads in the shell model. The resulting mesh contains relatively large elements, but it is considered sufficiently fine to represent the global responses in the bridge. Nevertheless, desired concentrated load effects in the plates might not be accurately reproduced. Reduced integration provides the resulting forces only in one integration point, giving a relatively rough solution. Abaqus models including traffic loads even have individually designed meshes, and integration points are consequently not coinciding in different models. Conservative results are secured by combining forces from the assumed most critical elements nearby the considered sections.

Traffic loads applied in Abaqus contain simplifications and modifications, as described and justified in Section 7.4. The many load models and rules given in R412 [28] regarding the traffic load open for an infinite number of traffic load configurations. Modelled load configurations are thus based on subjective choices, and some critical load combinations might therefore be missed. However, the tables from Chapter 9, including forces from Abaqus, show that contributions generated from traffic loads become relatively small compared to forces obtained from the self-weight and ASR. Simplifications regarding the traffic loads are considered to have a small impact on the capacity control.

Whether or not the temperature load should be included in combination with ASR in Elgeseter Bridge may be discussed. The current load situation, including ASR, probably have introduced plastic hinges and, consequently areas of reduced stiffness. A decreased bending stiffness implies a reduced restraint moment from temperature loads, as the two factors are directly related to each other. Including the full temperature effect in the stage I model is not entirely correct and will probably overestimate the bending moments. It is still decided to model the vertically varying temperature gradient conducting stage I-stiffness due to the above-mentioned uncertainties regarding the actual stiffness of the bridge.

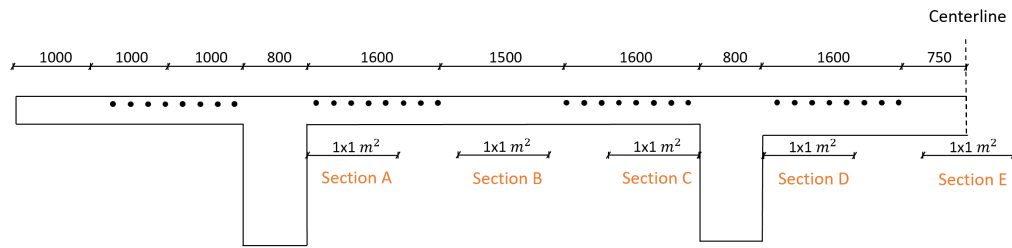
11.4 Capacity Control

The finite element analysis is performed with shell elements to describe the effects of simultaneously acting forces. Using the Iteration Method allows capacity control of a shell section considering both directions at the same time. Conducting the control using shell elements gives a local verification of the capacity. Only the reinforcement in the critical section is included to take the external forces. In reality, some of the external forces will distribute to the nearby reinforcement. Large amounts of reinforcement provide increased stiffness, which attract forces. The utilization ratios might be too conservative in some cases as redistribution of forces is not included in the capacity control.

However, high utilization ratios can not always be explained by redistribution of forces. Elements in section 2, the axis of zero bending moment, are assumed to contain the same large amounts of reinforcement as sections in the column axes. The total amount of longitudinal reinforcement in the plates decreases from sections in the column axes to the mid-spans as the reinforced T-beams narrow in. Less forces will redistribute from the mid-plate sections as the distance to the additional reinforcement gets larger.

The resulting utilization ratios in section B and section E in the column axes, S1 and S4, are particularly affected by the lack of redistribution in the local capacity control. As revealed in Section 10.1.4, the utilization ratios in these areas are par-

ticularly high. The fields of additional longitudinal reinforcement in the column axes extend approximately 1.6 meters to each side of the beams. As shown in Figure 11.1, only a 1.5 m wide part in the middle of the plates is designed without this additional upper reinforcement. Some of the large tensile forces are expected to redistribute to the nearby areas with larger amounts of reinforcement.



• Additional reinforcement $\phi 32$

Figure 11.1: Additional longitudinal reinforcement in the plates in the column axes

The most exceeded sections are located along the column axes. Global curvature induced by the vertical loads causes large tensile forces in the longitudinal reinforcement in the plates. The simply supported end in axis 10 and the pinned connection between columns and beams in axis 9, allow larger global curvature than a typical column axis between more restrained spans. The most significant tensile forces generated by the vertical loads are consequently found in the northernmost column axis. Tensile forces are amplified by ASR in mid-sections and counteracted in outer parts.

The highest utilization ratios from the capacity control are found in the plate between the inner and outer beams, section B, in the column axes. When considering yielding in the reinforcement as the limit, the utilization ratio is 5.26 in the typical column axis (S1B) and 6.25 in the northernmost column axis (S4B). The upper longitudinal reinforcement is most exposed and yields first. The tensile forces in section B are observed to be smaller than in sections C, D and E. However, section B contains small amounts of reinforcement and is therefore particularly critical. When considering ultimate failure strain, the utilization ratios are 4.44 and 5.08 in sections 1 and 4, respectively. The upper longitudinal reinforcement is still decisive.

Capacity controls are not performed in section E close to the column axes where large longitudinal tensile forces are present. Moment equilibrium cannot be obtained in these elements due to the lack of upper reinforcement, and no convergence is consequently achieved in the capacity program. However, comparison with section B, which is calculated to have the highest utilization ratio in the plate, indicates that section E in the column axes is even more critical. The longitudinal

tensile force is 65.8% larger in section 1E than in section 1B and 47.1% larger in section 4E than in section 4B. No compression fields are generated in upper parts of the cross-section, as longitudinal bending moments in sections 1E and 4E are small. The resulting forces thus indicate that the full height of the cross-section is in tension and that significant cracks should be present, particularly in the upper parts of the plate. An inspection of the concrete below the wearing course in sections 1E and 4E could be interesting, even though only minor cracks are observed from below. Crack growth in lower parts might be prohibited by the reinforcement, which is non existing in upper parts.

Furthermore, also section C is highly utilized in the column axes. The upper part of the plate contains 9.6 times more longitudinal reinforcement than the lower part. Large tensile forces and small amounts of reinforcement cause yielding in the lower reinforcement layer. The utilization ratios evaluating yielding is 3.27 in a typical column axis (S1C), and 3.48 in the northernmost column axis (S4C). The concrete is observed to be decisive when ultimate failure strain in the reinforcement is evaluated. The utilization ratios are calculated to be 1.82 and 1.72 in a typical column axis and in the last column axis.

The resulting forces are nearly the same for section C and D in the column axes. However, the higher amount of longitudinal reinforcement in the lower part in section D result in smaller utilization ratios in this section. Elgeseter Bridge was initially designed with tram rails in section D. In 1985, the tram rails were removed and the cavity in the plate was recast [16]. Calculations in the capacity control are conducted using the full height. A possible lack of compatibility between the old and new concrete might result in lower capacity in this section.

The utilization is, according to Table 10.3, in several sections limited by the compressive strength of the concrete if the ultimate failure strain in the reinforcement is evaluated. The strain in the reinforcement increases rapidly for a slight change in external loads after yielding has occurred. Figure 11.2 shows how the strains increase both in the reinforcement and in the concrete, as the ultimate failure strain is considered compared to yielding. Changing the limit of the reinforcement from yielding to ultimate failure opens for higher utilization of the compressive strength in the concrete. Table 10.5 shows that the reinforcement is highly utilized also in sections where concrete failure is decisive. This implies that a possible failure in the bridge for all the considered cases will occur as a ductile fracture, warned by large deformations.

The Iteration Method is conducted using 100 layers over the height of the cross-section. The stiffness is calculated in detail as the contribution from each layer is included. A utilization ratio of 1.0 for the concrete is obtained when the compressive stress level in one of the layers reaches the compressive strength, f_{cd} . The outermost layer is often exposed to the largest strains and will therefore usually

be decisive. The compressive strength limit corresponds to a strain level of 2‰ , even though the concrete in reality reaches failure when the strain exceeds 3.5‰ . This indicates that the concrete can withstand a slight increase in external loads before failure is obtained and that the concrete capacity might be underestimated. The additional capacity is however assumed to be small, as explained in the above section. Evaluating the capacity of the concrete with respect to the compressive strength is therefore considered to be sufficiently accurate.

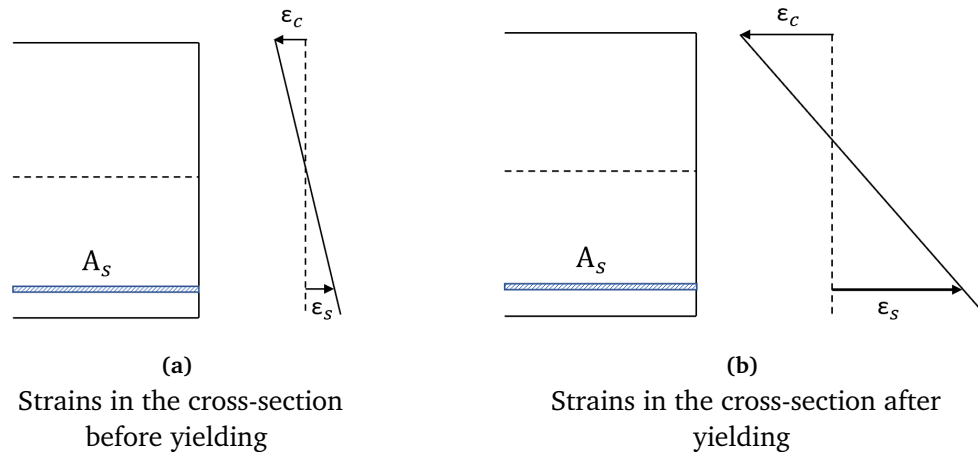


Figure 11.2: Strains in the cross-section before and after yielding in the reinforcement

The largest compressive force in the bridge is observed in section 3A, in the mid-spans, where both the ASR load and the self-weight generate compression in the plate. The compressive strength of the concrete is found sufficient, with a utilization ratio of 0.73. Sections 1A, 2A, 4A and 7A are nevertheless observed to have exceeded compressive capacity due to large bending moments in the transverse direction caused by the self-weight of the pedestrian lane. Section 4A is most critical among these sections with a utilization ratio of 1.52 in the concrete, when yielding is considered. Results from the capacity program show that the exceedance of the compressive strength is obtained easier by bending moments compared to pure compression, as the capacity is evaluated in the most critical layer. Pure compressive forces, like in the mid-spans, are distributed to all 100 layers in the capacity control, and are therefore not decisive. The large transverse bending moment also causes yielding in the reinforcement in these sections. Typical for section A is that the concrete fails in compression before the reinforcement reach the ultimate failure strain.

The last column in Table 10.5 and Table 10.5 show the utilization ratios of the concrete with regard to the reduced compressive strength. The reduced compressive strength is not included in the equilibrium within the iteration process and should therefore not be emphasized too much. Nevertheless, these results enlighten that

the concrete might be particularly critical in sections with combined compression and tension. Observed delamination in the bridge deck also indicates that the compression capacity in the concrete might be lower than assumed.

Section 6 is included in the capacity control because this is where the most significant in-plane shear forces due to ASR appear. Section C is critical due to the large in-plane shear force, combined with a tensile force in the longitudinal direction. In-plane shear forces contribute to stresses in the reinforcement in both directions. The reinforcement in the longitudinal direction has the highest utilization ratio due to tensile forces combined with a smaller amount of reinforcement. The utilization ratio is 2.26 when yielding strain is evaluated and 2.15 when evaluating failure strain of the reinforcement. Worth noticing is the small difference in capacity between yielding and failure strain. This indicates that a slight increase in external load results in a large increase in the strain of the reinforcement.

Furthermore, also the largest observed transverse compressive force originates from the earlier mentioned build-up of axial forces due to the ASR load. Concentrated forces appear along the northernmost simply supported end of the bridge. The most exposed concrete, in section 7E, only have a utilization ratio of 0.46. Thus, the transverse compression capacity is found sufficient.

Table 10.3, containing the utilization ratios, shows that a rather unexpected yielding is obtained in the longitudinal reinforcement in section 7A. Further investigation revealed that the reason is the concentrated and significant axial forces generated by the temperature load, earlier mentioned in Section 8.4. Significant axial forces combined with small amounts of reinforcement makes this section critical. The utilization ratio is 1.56 if yielding is considered and 1.21 if the ultimate failure strain in the reinforcement is considered. Ultimate failure in the cross-section is observed to occur almost simultaneously for the concrete and the reinforcement.

Uncertainties are related to the cover of the reinforcement in the plates. The cover is chosen to be 33 mm for the transverse reinforcement, even though NS427 states that a cover of 15 mm should have been used. The choice of cover is based on earlier master's theses and core samples from the bridge and is the best possible estimate. A smaller cover will result in a larger effective height of the cross-section, which will be favourable for the capacity calculations. The cover used in this thesis might therefore be too conservative in some cases.

11.5 The Capacity Program

The program used in the capacity control is developed by M. Hailemichael during his master's thesis [3]. The collaboration has been beneficial for both parties, as

results provided during the capacity control in this thesis has been useful feedback to the further development of the program. The program has even been customized to show the result parameters desired in this thesis. However, since the program development is ongoing, uncertainties are related to the results, even though the Iteration Method is known as a reliable method. The implemented code behind the interface of the program is not verified in this thesis. However, provided results are found satisfactory compared to results from hand calculations by the less accurate Membrane Method. The program is also simply verified as the sections found to have the highest utilization coincide with the sections expected to be most critical.

Chapter 12

Conclusion

The scope of this thesis was to study the plates of Elgeseter Bridge, especially concerning the effects due to alkali-silica reactions. ASR loads were calculated according to the Norwegian Public Road Administration's "ASR - Guidance for structural analysis", whereas the other loads were calculated according to Handbook R412. A shell model was established in Abaqus to analyse the bridge. The external loads were evaluated by implementing the loads in separate models. The capacity control in the ultimate limit state was conducted using the Iteration Method, including material properties according to NS3473:2003.

Loads due to ASR were implemented in the analysis as temperature loads corresponding to a total elongation of 200 mm. The outer parts of the bridge are assumed to expand more than the inner parts due to higher access to humidity. The inner parts restrain the expansion and generate compressive and tensile forces in the outer and inner parts, respectively. Furthermore, a gradient expansion is assumed over the height of the cross-section as a result of higher ASR in upper parts. External restraints from the columns prevent the upward deflection of the cross-section and induce restraint moments in the structure.

This thesis has not included the possible reduction of ASR expansion in directions with compressive stresses, nor the adverse effects ASR may have on the material properties of concrete.

Plate sections along column axes are generally exposed to the most significant tensile forces. Sections in the mid-plate are particularly vulnerable, as they contain small amounts of reinforcement. Results from the capacity control showed that the most critical sections are found in the column axes in the middle of the plate between the outer and inner beams (section B). If yielding in the reinforcement is considered as the failure criterion, the utilization ratio is 5.26 in a typical column axis (S1B) and 6.25 in the northernmost column axis (S4B).

The ULS failure capacity control considers either ultimate failure strain in the

reinforcement or failure of the compressive strength in the concrete. The capacity in the mid-plate sections between outer and inner beams is still limited by the longitudinal reinforcement, even though a reinforcement strain limit of 10‰ is considered. The utilization ratio is 4.44 in a typical column axis (S1B) and 5.08 in the northernmost column axis (S4B).

The mid-plate between the inner beams (section E) is designed without upper reinforcement. Axial tensile forces occur in both upper and lower parts of the plate along the column axes (S1E and S4E). Moment equilibrium cannot be achieved due to the lack of upper reinforcement, and no convergence is therefore obtained in the Iteration Method. The exceedance of the capacity is however assumed to be larger than for the above-mentioned mid-plate between outer and inner beams (Section B), considering the more significant tensile forces and the single layer of reinforcement.

The capacity of sections in the outer transition zone to the inner beams is highly exceeded along the bridge (section C). If yielding in the reinforcement is considered as the failure criterion, the utilization ratio is 3.27 in a typical column axis (S1C) and 3.48 in the northernmost column axis (S4C). However, when the failure strain of the reinforcement is controlled, these sections have utilization ratios of 1.82 and 1.72, respectively, limited by the compressive strength in the concrete. The capacity control considering ultimate failure strain reveals that several sections reach failure in the concrete just before failure strain is obtained in the reinforcement.

The capacity in the plate nearby the outer beams are exceeded in most of the considered cases along the bridge (section A). The highest utilization occurs in the northernmost column axis (S4A). The transverse reinforcement limits the capacity with a utilization ratio of 1.56 when yielding in the reinforcement is evaluated. When evaluating ultimate failure strain, the utilization ratio is 1.48, limited by the concrete compressive strength.

The compressive capacity of the concrete is found satisfactory in mid-span sections, where the most significant compressive forces are observed. The most utilized concrete amongst the mid-span sections is located close to the outer beam in the axis of maximum bending moment (S5A), with a utilization ratio of 0.84. Sufficient compressive strength is also found at the northern end support, where significant transverse axial forces generated from ASR appear. The highest observed utilization ratio in the inner plate is 0.46.

Large in-plane shear forces due to ASR occur in the span 3-4 meters from the simply supported end. The combination of in-plane shear forces and tensile forces is critical for the plate section near the outside of the inner beams (S6C). The longitudinal reinforcement has a utilization ratio of 2.26 with yielding as the

failure limit and 2.15 considering ultimate failure strain.

No sign of considerable cracks is observed in the plates, even though inspections have revealed wide cracks in both beams and columns. However, the magnitude of forces obtained from the uncracked analysis indicates that also significant parts of the plate might be in a cracked state. Performing a non-linear analysis where cracks are taken into account would probably give more accurate results. However, a full non-linear analysis is time-consuming and contains several uncertainties.

The capacity control resulted in high exceedance of the capacity several places in the plate. Yielding in the reinforcement is detected in 17 of the 32 controlled sections. Among these, 14 sections even have exceeded capacity when failure strain in the reinforcement is considered as the failure criterion. The capacity control reveals that 9 sections reach failure in the concrete before failure strain is obtained in the reinforcement. Even though redistribution of forces might reduce the utilization ratios in local sections, this study shows that the plates of Elgeseter Bridge are highly utilized. Sections with exceeded capacity should be carefully considered in further investigation of the bridge.

Bibliography

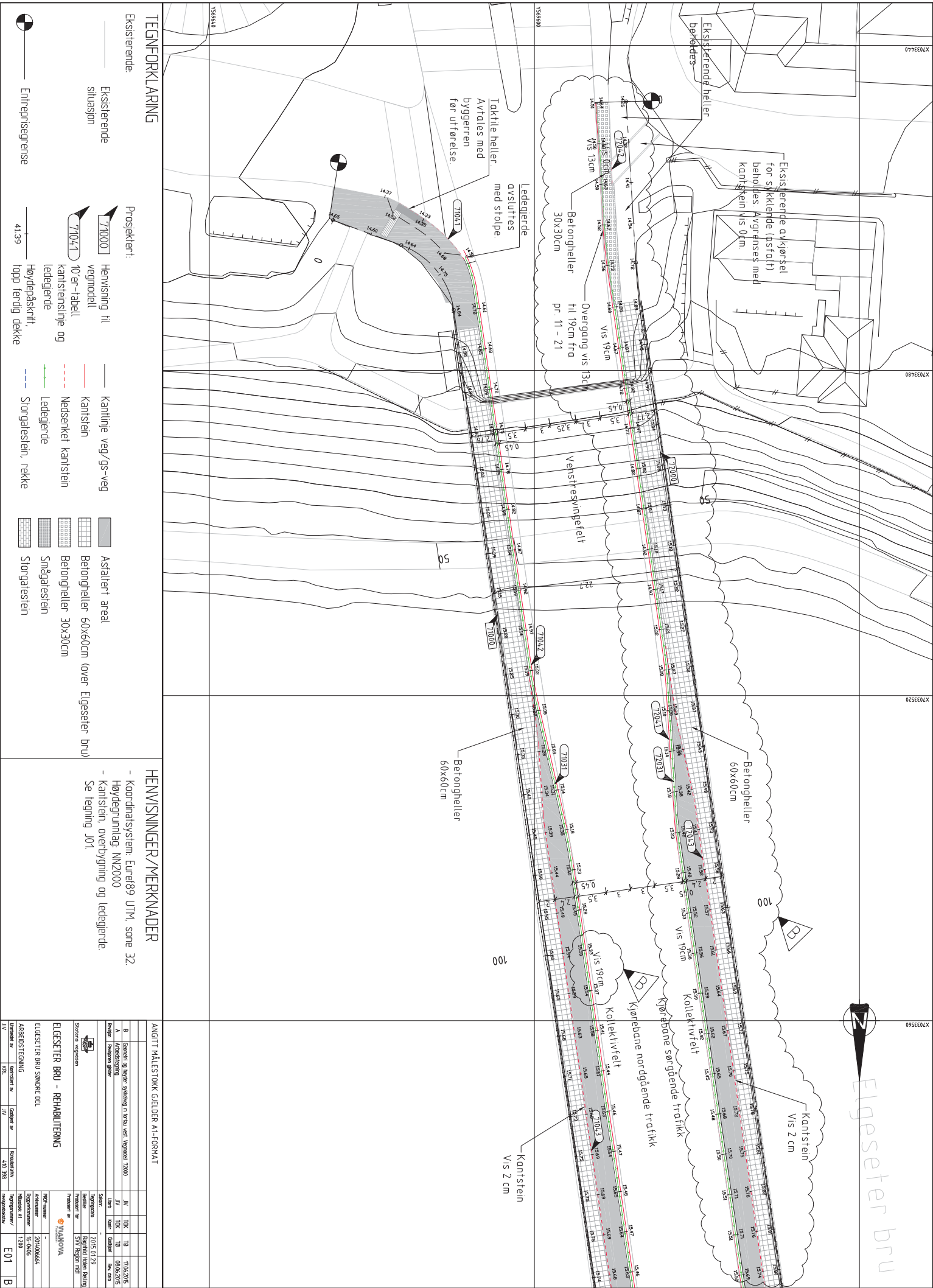
- [1] S. I. Sørensen, *Betongkonstruksjoner, Beregning og dimensjonering etter Eurokode 2*. Fagbokforlaget, 2013.
- [2] S. Jacobsen, M. Maage, S. Smepllass, K. Kjellsen, E. Sellevold, J. Lindgård, R. Cepuritis, R. Myrdal, Ø. Bjøntegaard and M. Geiker, *Concrete Technology*. 2016.
- [3] M. M. Hailemichael, 'Non-linear cross-sectional analysis of concrete shells,' 2021.
- [4] S. S. Kongshaug, O. Oseland, T. Kanstad, M. A. Hendriks, E. Rodum and G. Markeset, *Experimental investigation of ASR-affected concrete - the influence of uniaxial loading on the evolution of mechanical properties, expansion and damage indices*, Oslo Metropolitan University, 2020.
- [5] H. Stemland, E. Rodum and H. Johansen, *Alkalireaksjoner - Veiledning for konstruktiv analyse*, Statens Vegvesen, Etatsprogrammet Varige konstruksjoner 2012-2015, 2016.
- [6] I. Fernandes and M. Broekmans, 'Alkali-silica reactions: An overview. part i,' 2013.
- [7] Byggforskserien. (2007). 'Alkalireaksjoner i betong. skademekanisme og regelverk ved nybygging,' [Online]. Available: https://www.byggforsk.no/dokument/299/alkalireaksjoner_i_betong_skademekanisme_og_regelverk_ved_nybygging.
- [8] R. A. Barbosa, S. G. Hansen, K. K. Hansen, L. C. Hoang and B. Grelk, *Influence of alkali-silica reaction and crack orientation on the uniaxial compressive strength of concrete cores from slab bridges*, Construction and Building Materials, 2018.
- [9] G. Giaccio, M. C. Torrijos, J. Tobes, O. Batic and R. Zerbino, 'Development of alkali-silica reaction under compressive loading and its effects on concrete behavior,' vol. 106, pp. 223–230, 2009.
- [10] B. Gautam, D. Panesar, S. Sheikh and F. Vecchio, 'Effect of multiaxial stresses on alkali-silica reaction damage of concrete,' *ACI Materials Journal*, vol. 114, 2017.

- [11] L. Sanchez, B. Fournier, M. Jolin and J. Bastien, 'Evaluation of the stiffness damage test (sdt) as a tool for assessing damage in concrete due to asr: Test loading and output responses for concretes incorporating fine or coarse reactive aggregates,' *Cement and Concrete Research*, vol. 56, pp. 213–229, 2014.
- [12] K. A. Olsen and P. Christiansen. (2017). 'Elgeseter bru 1912 og 2017,' [Online]. Available: <https://www.adressa.no/pluss/magasin/2017/10/23/Elgeseter-bru-1912-og-2017-15447456.ece?rs4901821611214413077&t=1>.
- [13] T. Bratberg. (1996). 'Trondheim byleksikon,' [Online]. Available: https://www.nb.no/items/URN:NBN:no-nb_digibok_2008080104041?page=7&searchText=elgeseter%20bru.
- [14] E. V. Thorenfeldt, *SVV 339 - Alkaliereaksjoner - Karbonfiberforsøk Elgeseter bru, 16-0406 Elgeseter bru (2013)*, 2015.
- [15] Riksantikvaren. (2008). 'Elgeseter bru,' [Online]. Available: <https://kulturminnesok.no/minne/?queryString=https://data.kulturminne.no/askeladden/lokalitet/110549>.
- [16] Aas-Jakobsen and Statens Vegvesen, *Rapport fra spesialinspeksjon 2012, 16-0406 Elgeseter bru*, 2013.
- [17] Aas-Jakobsen, *Beregningsrapport Elgeseter bru, 11752-35-03 Klassifisering for Bk10/50*, 2020.
- [18] E. Rodum, B. M. Pedersen and R. H. Relling, *Field and laboratory examinations of an ASR-affected bridge - Variation in crack extent and water content*, 2016.
- [19] H. Johansen, *Klassifisering av Elgeseter bru 2020 Beregningsforutsetninger*, Vegdirektoratet Bruseksjonen, 2019.
- [20] K. O. Nordhaug and K. M. Stemland, 'Beregning av bru med alkaliereaksjoner,' 2018.
- [21] E. S. Christensen and S. F. Sande, 'Evaluation of externally reinforced bridge exposed to alkali-silica reactions,' 2020.
- [22] European Commission. (2021). 'About the EN Eurocodes,' [Online]. Available: <https://eurocodes.jrc.ec.europa.eu/showpage.php?id=1>.
- [23] Standard Norge, *NS 3473:2003 Concrete structures - Design and detailing rules*. 2003.
- [24] Standard Norge, *Eurocode 1: Actions on structures - Part 1-1: General actions - Densities, self-weight, imposed loads for buildings*. 2019.
- [25] Standard Norge, *Eurocode 2: Design of concrete structures - Part 1-1: General rules and rules for buildings*. 2018.
- [26] Standard Norge, *NS-EN 1991-1-5:2003+NA:2008*. 2003.

- [27] *Håndbok N400 - Bruprosjektering*. The Norwegian Public Road Administration, 2015.
- [28] *Håndbok R412 - Bruklassifisering*. The Norwegian Public Road Administration, 2014.
- [29] G. Kjellmark, *Bestemmelse av trykkfasthet utborede kjerner Elgeseter bru*, Sintef (Table distributed by co-supervisor K. Stemland), 2015.
- [30] I. Lyse and N. J. Wiig, *Betong: uarmert og armert*. F. Bruns bokhandels forlag, Trondheim, 1957.
- [31] K. Stemland, *E-mail correspondance regarding core samples from Elgeseter Bridge*, NTNU - Department of Structural Engineering, Apr. 2021.
- [32] Scanscot Technology. (2021). 'Simulia abaqus,' [Online]. Available: https://scanscot.com/products/simulia/abaqus/?gclid=CjwKCAjw9r-DBhBxEiwA9qYUpbNLYtXFIq_I6anf6ypdbzAbnKPBFC1Cww2xxR3vGsgCkbg9JlEnRxoCKzoQAvD_BwE.
- [33] C. Obbink-Huizer. (2019). "units in abaqus," [Online]. Available: <https://info.simuleon.com/blog/units-in-abaqus>.
- [34] Dassault Systèmes Simulia Corporation. (2017). "performance of continuum and shell elements for linear analysis of bending problems," [Online]. Available: <https://abaqus-docs.mit.edu/2017/English/SIMACAEBMKRefMap/simabmk-c-linbending.htm>.
- [35] M. Hendriks, *Conversation regarding Elgeseter Bridge*, NTNU - Department of Structural Engineering, 2021.
- [36] E. Zellerer, *Durchlaufträger. Schnittgrößen für Kragarmbelastung. Ergänzungsband zu "Durchlaufträger-Schnittgrößen" 2. Auflage*. Berlin-München: Wilhelm Ernst & Sohn, 1969.
- [37] H. Johansen, *SVV 668 - Beregningveiledning for etteroppspente betongbruer*, Statens Vegvesen, 2017.
- [38] H. Johansen, *Klassifisering av Elgeseter bru, Vedlegg: Resultater fra Aas-Jakobsen's analyser*, Statens Vegvesen, 2021.
- [39] A. Fucher, *Einflussfelder elastischer Platten*. Wien: Springer-Verlag, 1964.
- [40] *Compendium TKT4222 Concrete Structures 3*. Department of Structural Engineering NTNU.

Appendix A

Drawings



TEGNFORKLARING

Ekstisterende:

Ekstisterende situasjon

Entreprisegrense

Prosjekter:

710001

Henvisning til vegmodell

71041

10'er-tabel kantstenslinje og ledegjerde

Høydepriskrift, topp ferdig dekke

41.39

Kantlinje veg/gs-veg

Kantstein

Nedsenket kantstein

Ledegjerde

Storgatestein, rekke

Astaltert areal

Betongheller 60x60cm (over Elgeseter bru)

Betongheller 30x30cm

Smågatestein

Storgatestein

HENVISNINGER/MERKNADER

- Koordinatsystem: Euref89 UTM, zone 32.
- Høydegrunnlag: NN2000
- Kantstein overbygning og ledegjerde. Se tegning J01

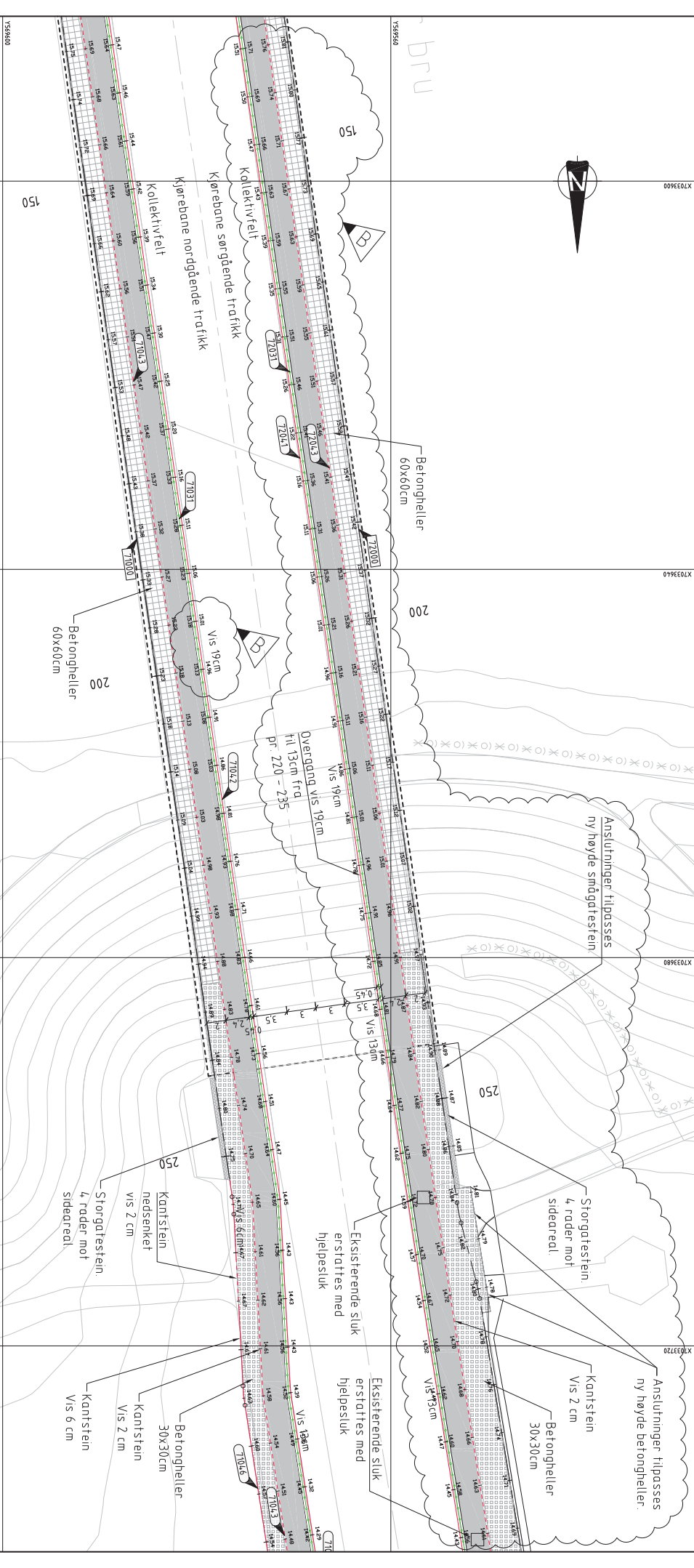
ANGITT MÅLSTOKK GJELDER A1-FORMAT

ARBEDS-TEGNING		Tegnet av		Tegnet av		Tegningsno.	
B	Generell og detalj utvalgt i henhold til Vegvesen 12000	JV	TKK	IB	TKK	18	1716/2015
A	Prosjektplan	JV	TKK	IB	TKK	18	1716/2015
Revusert	Revisjon nr. 1	JV	TKK	IB	TKK	18	1716/2015
Revusert	Revisjon nr. 2	JV	TKK	IB	TKK	18	1716/2015
Revusert	Revisjon nr. 3	JV	TKK	IB	TKK	18	1716/2015
Revusert	Revisjon nr. 4	JV	TKK	IB	TKK	18	1716/2015
Revusert	Revisjon nr. 5	JV	TKK	IB	TKK	18	1716/2015
Revusert	Revisjon nr. 6	JV	TKK	IB	TKK	18	1716/2015
Revusert	Revisjon nr. 7	JV	TKK	IB	TKK	18	1716/2015
Revusert	Revisjon nr. 8	JV	TKK	IB	TKK	18	1716/2015
Revusert	Revisjon nr. 9	JV	TKK	IB	TKK	18	1716/2015
Revusert	Revisjon nr. 10	JV	TKK	IB	TKK	18	1716/2015
Revusert	Revisjon nr. 11	JV	TKK	IB	TKK	18	1716/2015
Revusert	Revisjon nr. 12	JV	TKK	IB	TKK	18	1716/2015
Revusert	Revisjon nr. 13	JV	TKK	IB	TKK	18	1716/2015
Revusert	Revisjon nr. 14	JV	TKK	IB	TKK	18	1716/2015
Revusert	Revisjon nr. 15	JV	TKK	IB	TKK	18	1716/2015
Revusert	Revisjon nr. 16	JV	TKK	IB	TKK	18	1716/2015
Revusert	Revisjon nr. 17	JV	TKK	IB	TKK	18	1716/2015
Revusert	Revisjon nr. 18	JV	TKK	IB	TKK	18	1716/2015
Revusert	Revisjon nr. 19	JV	TKK	IB	TKK	18	1716/2015
Revusert	Revisjon nr. 20	JV	TKK	IB	TKK	18	1716/2015
Revusert	Revisjon nr. 21	JV	TKK	IB	TKK	18	1716/2015
Revusert	Revisjon nr. 22	JV	TKK	IB	TKK	18	1716/2015
Revusert	Revisjon nr. 23	JV	TKK	IB	TKK	18	1716/2015
Revusert	Revisjon nr. 24	JV	TKK	IB	TKK	18	1716/2015
Revusert	Revisjon nr. 25	JV	TKK	IB	TKK	18	1716/2015
Revusert	Revisjon nr. 26	JV	TKK	IB	TKK	18	1716/2015
Revusert	Revisjon nr. 27	JV	TKK	IB	TKK	18	1716/2015
Revusert	Revisjon nr. 28	JV	TKK	IB	TKK	18	1716/2015
Revusert	Revisjon nr. 29	JV	TKK	IB	TKK	18	1716/2015
Revusert	Revisjon nr. 30	JV	TKK	IB	TKK	18	1716/2015
Revusert	Revisjon nr. 31	JV	TKK	IB	TKK	18	1716/2015
Revusert	Revisjon nr. 32	JV	TKK	IB	TKK	18	1716/2015
Revusert	Revisjon nr. 33	JV	TKK	IB	TKK	18	1716/2015
Revusert	Revisjon nr. 34	JV	TKK	IB	TKK	18	1716/2015
Revusert	Revisjon nr. 35	JV	TKK	IB	TKK	18	1716/2015
Revusert	Revisjon nr. 36	JV	TKK	IB	TKK	18	1716/2015
Revusert	Revisjon nr. 37	JV	TKK	IB	TKK	18	1716/2015
Revusert	Revisjon nr. 38	JV	TKK	IB	TKK	18	1716/2015
Revusert	Revisjon nr. 39	JV	TKK	IB	TKK	18	1716/2015
Revusert	Revisjon nr. 40	JV	TKK	IB	TKK	18	1716/2015
Revusert	Revisjon nr. 41	JV	TKK	IB	TKK	18	1716/2015
Revusert	Revisjon nr. 42	JV	TKK	IB	TKK	18	1716/2015
Revusert	Revisjon nr. 43	JV	TKK	IB	TKK	18	1716/2015
Revusert	Revisjon nr. 44	JV	TKK	IB	TKK	18	1716/2015
Revusert	Revisjon nr. 45	JV	TKK	IB	TKK	18	1716/2015
Revusert	Revisjon nr. 46	JV	TKK	IB	TKK	18	1716/2015
Revusert	Revisjon nr. 47	JV	TKK	IB	TKK	18	1716/2015
Revusert	Revisjon nr. 48	JV	TKK	IB	TKK	18	1716/2015
Revusert	Revisjon nr. 49	JV	TKK	IB	TKK	18	1716/2015
Revusert	Revisjon nr. 50	JV	TKK	IB	TKK	18	1716/2015
Revusert	Revisjon nr. 51	JV	TKK	IB	TKK	18	1716/2015
Revusert	Revisjon nr. 52	JV	TKK	IB	TKK	18	1716/2015
Revusert	Revisjon nr. 53	JV	TKK	IB	TKK	18	1716/2015
Revusert	Revisjon nr. 54	JV	TKK	IB	TKK	18	1716/2015
Revusert	Revisjon nr. 55	JV	TKK	IB	TKK	18	1716/2015
Revusert	Revisjon nr. 56	JV	TKK	IB	TKK	18	1716/2015
Revusert	Revisjon nr. 57	JV	TKK	IB	TKK	18	1716/2015
Revusert	Revisjon nr. 58	JV	TKK	IB	TKK	18	1716/2015
Revusert	Revisjon nr. 59	JV	TKK	IB	TKK	18	1716/2015
Revusert	Revisjon nr. 60	JV	TKK	IB	TKK	18	1716/2015
Revusert	Revisjon nr. 61	JV	TKK	IB	TKK	18	1716/2015
Revusert	Revisjon nr. 62	JV	TKK	IB	TKK	18	1716/2015
Revusert	Revisjon nr. 63	JV	TKK	IB	TKK	18	1716/2015
Revusert	Revisjon nr. 64	JV	TKK	IB	TKK	18	1716/2015
Revusert	Revisjon nr. 65	JV	TKK	IB	TKK	18	1716/2015
Revusert	Revisjon nr. 66	JV	TKK	IB	TKK	18	1716/2015
Revusert	Revisjon nr. 67	JV	TKK	IB	TKK	18	1716/2015
Revusert	Revisjon nr. 68	JV	TKK	IB	TKK	18	1716/2015
Revusert	Revisjon nr. 69	JV	TKK	IB	TKK	18	1716/2015
Revusert	Revisjon nr. 70	JV	TKK	IB	TKK	18	1716/2015
Revusert	Revisjon nr. 71	JV	TKK	IB	TKK	18	1716/2015
Revusert	Revisjon nr. 72	JV	TKK	IB	TKK	18	1716/2015
Revusert	Revisjon nr. 73	JV	TKK	IB	TKK	18	1716/2015
Revusert	Revisjon nr. 74	JV	TKK	IB	TKK	18	1716/2015
Revusert	Revisjon nr. 75	JV	TKK	IB	TKK	18	1716/2015
Revusert	Revisjon nr. 76	JV	TKK	IB	TKK	18	1716/2015
Revusert	Revisjon nr. 77	JV	TKK	IB	TKK	18	1716/2015
Revusert	Revisjon nr. 78	JV	TKK	IB	TKK	18	1716/2015
Revusert	Revisjon nr. 79	JV	TKK	IB	TKK	18	1716/2015
Revusert	Revisjon nr. 80	JV	TKK	IB	TKK	18	1716/2015
Revusert	Revisjon nr. 81	JV	TKK	IB	TKK	18	1716/2015
Revusert	Revisjon nr. 82	JV	TKK	IB	TKK	18	1716/2015
Revusert	Revisjon nr. 83	JV	TKK	IB	TKK	18	1716/2015
Revusert	Revisjon nr. 84	JV	TKK	IB	TKK	18	1716/2015
Revusert	Revisjon nr. 85	JV	TKK	IB	TKK	18	1716/2015
Revusert	Revisjon nr. 86	JV	TKK	IB	TKK	18	1716/2015
Revusert	Revisjon nr. 87	JV	TKK	IB	TKK	18	1716/2015
Revusert	Revisjon nr. 88	JV	TKK	IB	TKK	18	1716/2015
Revusert	Revisjon nr. 89	JV	TKK	IB	TKK	18	1716/2015
Revusert	Revisjon nr. 90	JV	TKK	IB	TKK	18	1716/2015
Revusert	Revisjon nr. 91	JV	TKK	IB	TKK	18	1716/2015
Revusert	Revisjon nr. 92	JV	TKK	IB	TKK	18	1716/2015
Revusert	Revisjon nr. 93	JV	TKK	IB	TKK	18	1716/2015
Revusert	Revisjon nr. 94	JV	TKK	IB	TKK	18	1716/2015
Revusert	Revisjon nr. 95	JV	TKK	IB	TKK	18	1716/2015
Revusert	Revisjon nr. 96	JV	TKK	IB	TKK	18	1716/2015
Revusert	Revisjon nr. 97	JV	TKK	IB	TKK	18	1716/2015
Revusert	Revisjon nr. 98	JV	TKK	IB	TKK	18	1716/2015
Revusert	Revisjon nr. 99	JV	TKK	IB	TKK	18	1716/2015
Revusert	Revisjon nr. 100	JV	TKK	IB	TKK	18	1716/2015
Revusert	Revisjon nr. 101	JV	TKK	IB	TKK	18	1716/2015
Revusert	Revisjon nr. 102	JV	TKK	IB	TKK	18	1716/2015
Revusert	Revisjon nr. 103	JV	TKK	IB	TKK	18	1716/2015
Revusert	Revisjon nr. 104	JV	TKK	IB	TKK	18	1716/2015
Revusert	Revisjon nr. 105	JV	TKK	IB	TKK	18	1716/2015
Revusert	Revisjon nr. 106	JV	TKK	IB	TKK	18	1716/2015
Revusert	Revisjon nr. 107	JV	TKK	IB	TKK	18	1716/2015
Revusert	Revisjon nr. 108	JV	TKK	IB	TKK	18	1716/2015
Revusert	Revisjon nr. 109	JV	TKK	IB	TKK	18	1716/2015
Revusert	Revisjon nr. 110	JV	TKK	IB	TKK	18	1716/2015
Revusert	Revisjon nr. 111	JV	TKK	IB	TKK	18	1716/2015
Revusert	Revisjon nr. 112	JV	TKK	IB	TKK	18	1716/2015
Revusert	Revisjon nr. 113	JV	TKK	IB	TKK	18	1716/2015
Revusert	Revisjon nr. 114	JV	TKK	IB	TKK	18	1716/2015
Revusert	Revisjon nr. 115	JV	TKK	IB	TKK	18	1716/2015
Revusert	Revisjon nr. 116	JV	TKK	IB	TKK	18	1716/2015
Revusert	Revisjon nr. 117	JV	TKK	IB	TKK	18	1716/2015
Revusert	Revisjon nr. 118	JV	TKK	IB	TKK	18	1716/2015
Revusert	Revisjon nr. 119	JV	TKK	IB	TKK	18	1716/2015
Revusert	Revisjon nr. 120	JV	TKK	IB	TKK	18	1716/2015

Elgeseter bru



009E60LX
099E60LX
089E60LX
079E60LX



TEGNFORKLARING

Existierende:

- Existierende situasjon

Prosjekter:

- Henvisning til vegmodell
- 10'er-tabell
- kantsteinstipe og ledeggerde
- Høydepåskrift, topp ferdig dekke
- 4139
- Kantlinje veg/gs-veg
- Kantstein
- Nedsenket kantstein
- Ledeggerde
- Storgatestein, rekke
- Asfaltert areal
- Betongheller 60x60cm (over Elgeseter bru)
- Betongheller 30x30cm
- Smågatestein
- Storgatestein

HENVISNINGER/MERKNADER

- Koordinatsystem: EUREF89 UTM, zone 32.
- Høydegrunnlag: NN2000
- Kantstein, overbygning og ledeggerde. Se tegning J01

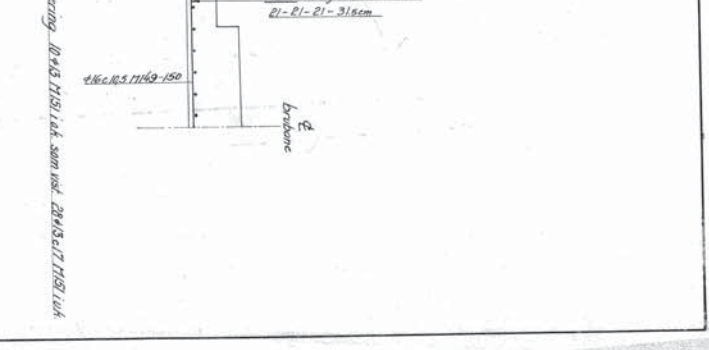
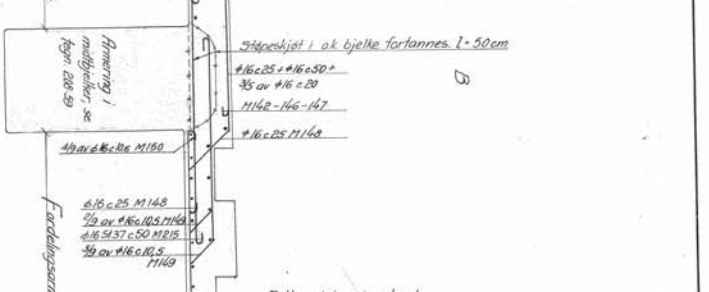
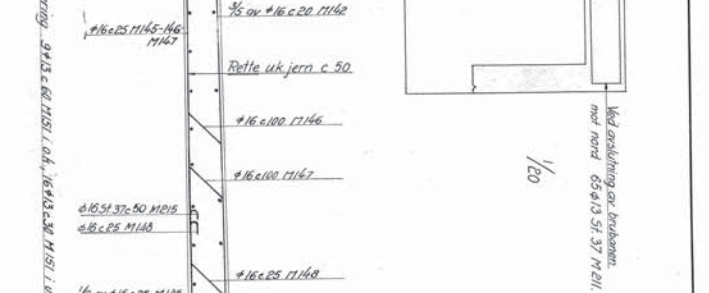
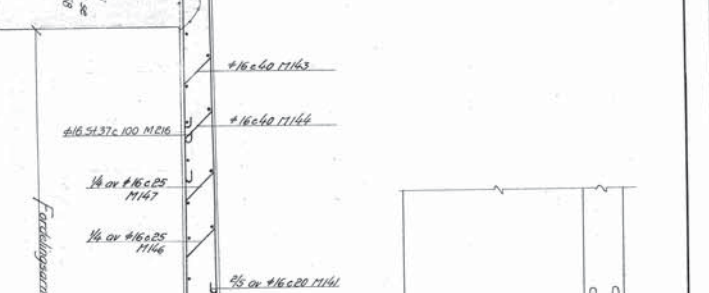
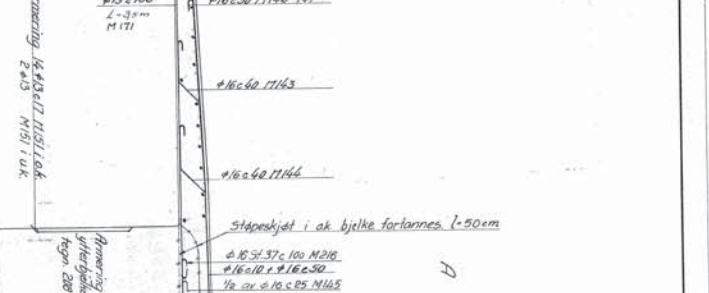
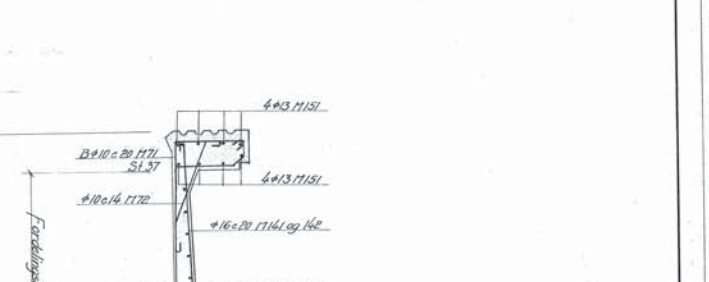
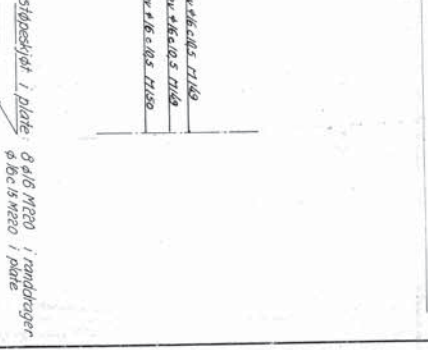
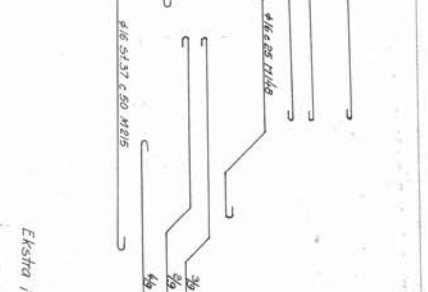
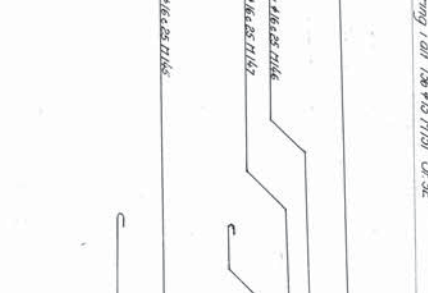
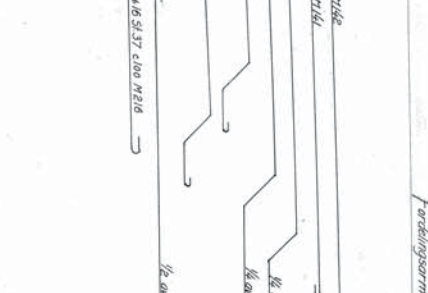
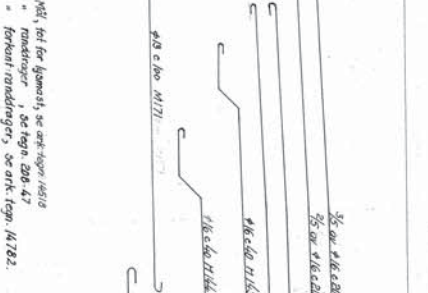
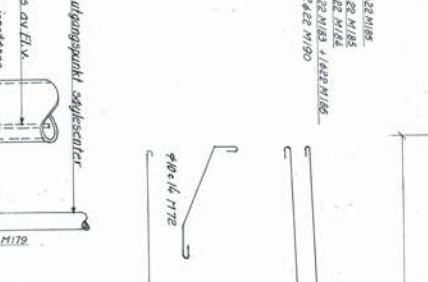
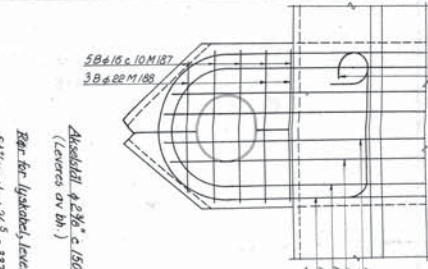
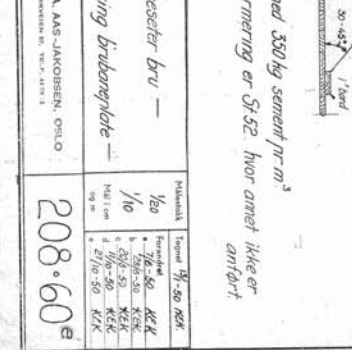
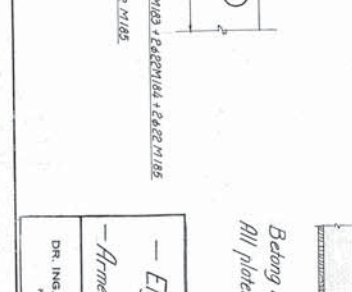
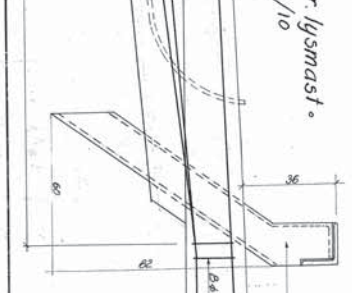
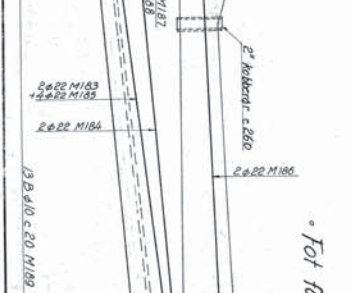
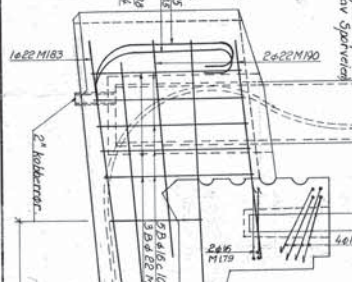
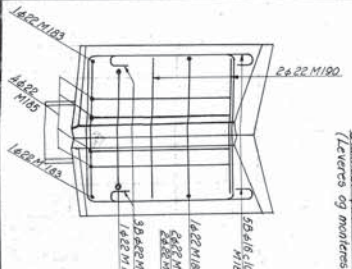
ANGITT MÅLSTOKK GJELDER A1-FORMAT

ARBETSDOKUMENT		Tegning nr.		Egetegnet nr.		Hvertegningsnummer		Egetegnet nr.	
E02		E02		E02		E02		E02	
E02		E02		E02		E02		E02	

B	Grunntegning			JV	TKK	18	17/06/2015
A	Revisjon			JV	TKK	18	06/06/2015
Revisjon nr.		Revisjon dato		Revisjon av		Revisjon av	
1		23.01.2015		Revisjon av		SVT/Revisjon med	
1		23.01.2015		Revisjon av		SVT/Revisjon med	
1		23.01.2015		Revisjon av		SVT/Revisjon med	

ELGESETER BRU - REHABILITERING		Egetegnet nr.		Hvertegningsnummer		Egetegnet nr.	
E02		E02		E02		E02	
E02		E02		E02		E02	

ARBETSDOKUMENT		Tegning nr.		Egetegnet nr.		Hvertegningsnummer		Egetegnet nr.	
E02		E02		E02		E02		E02	
E02		E02		E02		E02		E02	



Åkselstift ϕ 230 c 150, afgangs punkt søjlesædler
(Læres af bh.)

Mål, bet for lysmast, se ark. tegn. 14510
* randskærer i se. tegn. 230-47
* forskant randskærer, se ark. tegn. 14702.

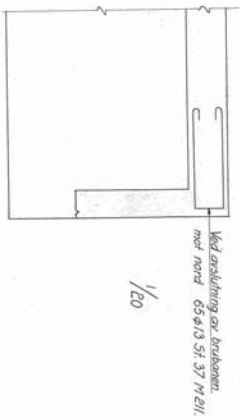
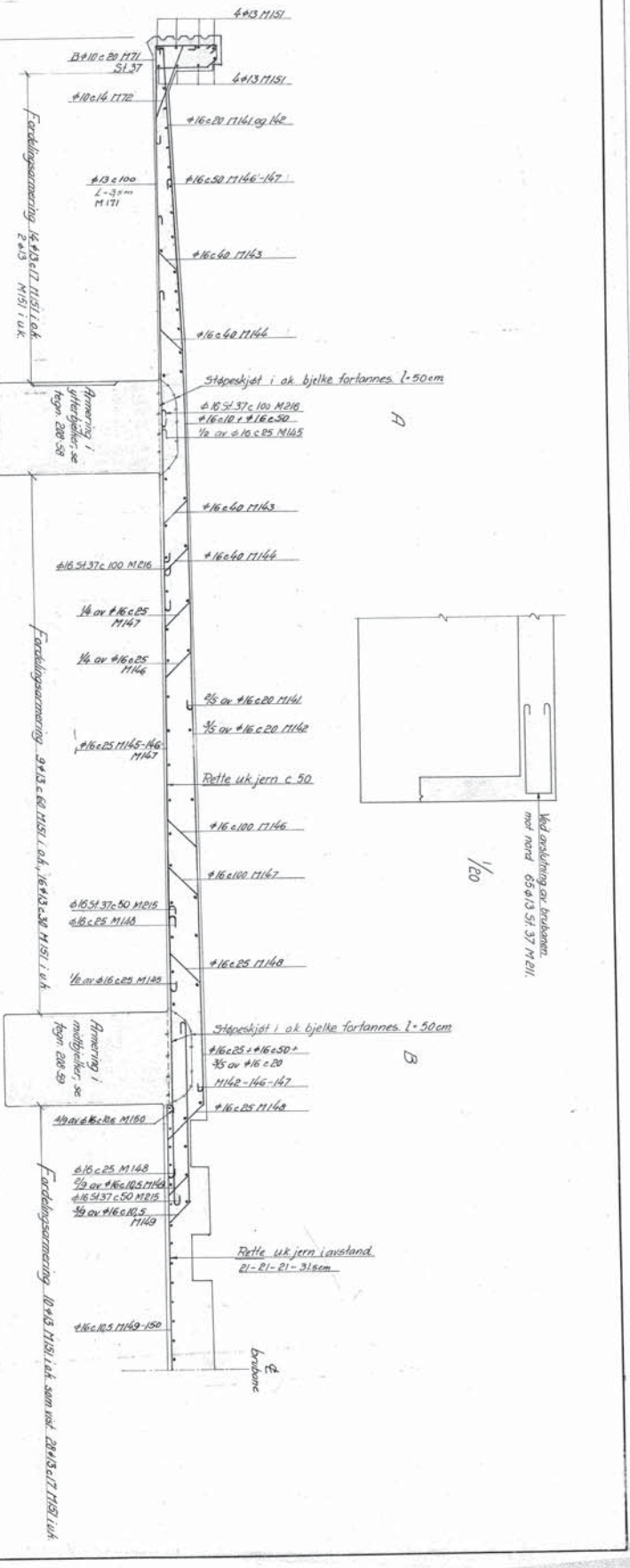
Fot for lysmast.
1/10

Belæg med 350 kg sement pr m²
Alle platerørning er St-52 hvor andet ikke er
angivet

Ekstra i støbeskjet i plade: ϕ 16 M200 i randskærer
 ϕ 16 c 15 M200 i plade

Ejerskaber bru		Armering båndmateriale	
Mængde	150	Armering	208.60€
1/10			
27/10-50	K/K		
27/10-50	K/K		
27/10-50	K/K		

DR. ING. A. AAS-JACOBSEN, OSLO



1/20

B

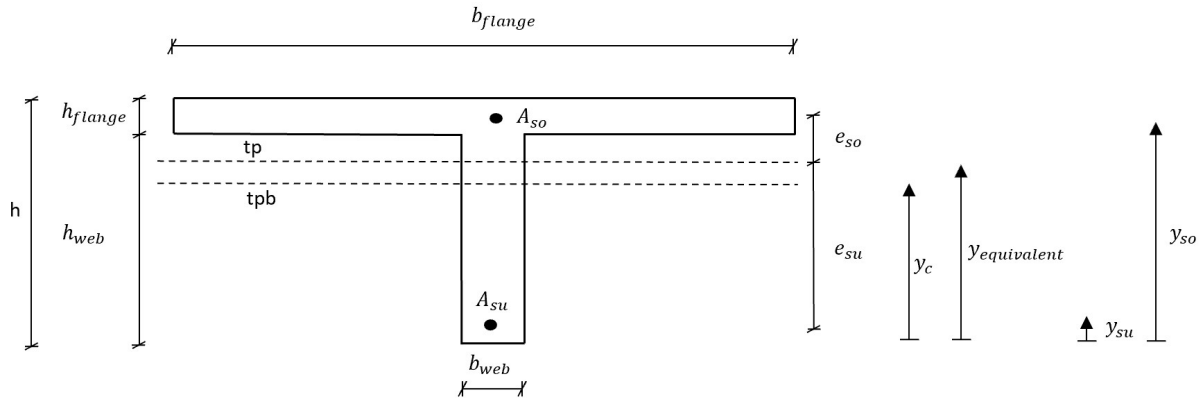
betonen

Appendix B

Verification of ASR Loads from Aas-Jakobsen

Verification of ASR loads from Aas-Jakobsen

The process of calculating the ASR loads is shown by an example in Aas-Jakobsen's report. However, the formulas for the different strain contributions are not shown in detail. Aas-Jakobsen's ASR loads are verified by calculating the loads according to "Elgeseter bru - Beregningsforutsetninger" from the Norwegian Public Road Administration. Furthermore, the comparison is made with kelvin instead of degrees, as degrees is not defined in Mathcad.



1. Calculating cross-section parameters

Aas-Jakobsen used a Young's modulus equal to 160000 MPa for the reinforcement. The same value is used in this verification in order to compare the results.

$$h := 1710 \text{ mm}$$

$$E_{c,long} := 10000 \text{ MPa}$$

$$h_{flange} := 280 \text{ mm}$$

$$E_s := 160000 \text{ MPa}$$

$$h_{web} := 1430 \text{ mm}$$

$$\alpha := 1 \cdot 10^{-5} \text{ K}^{-1}$$

$$b_{flange} := 5500 \text{ mm}$$

$$b_{web} := 800 \text{ mm}$$

$$A_{su} := 4825 \text{ mm}^2$$

$$y_c := 1206 \text{ mm}$$

$$A_{so} := 25635 \text{ mm}^2$$

$$y_{su} := 49 \text{ mm}$$

$$A_{s,total} := A_{su} + A_{so} = 30460 \text{ mm}^2$$

$$y_{so} := 1597 \text{ mm}$$

$$A_c := h_{flange} \cdot b_{flange} + h_{web} \cdot b_{web} = 2684000 \text{ mm}^2$$

$$I_c := 6.85 \cdot 10^{11} \text{ mm}^4$$

$$\eta := \frac{E_s}{E_{c,long}} = 16$$

$$A_{equivalent} := A_c + (\eta - 1) \cdot A_{s,total} = 3140900 \text{ mm}^2$$

$$y'_{equivalent} := \frac{A_c \cdot y_c + (\eta - 1) \cdot A_{su} \cdot y_{su} + (\eta - 1) \cdot A_{so} \cdot y_{so}}{A_{equivalent}} = 1227.2 \text{ mm}$$

$$I_{equivalent} := I_c + A_c \cdot (y_{equivalent} - y_c)^2 + (\eta - 1) \left(A_{su} \cdot (y_{equivalent} - y_{su})^2 + A_{so} \cdot (y_{equivalent} - y_{so})^2 \right) = (8.393 \cdot 10^{11}) \text{ mm}^4$$

2. Contributions from the free expansion

$$\varepsilon_{free.top} := 1.35 \cdot 10^{-3}$$

Free strain at top edge

$$\varepsilon_{free.bottom} := 9 \cdot 10^{-4}$$

Free strain at bottom edge

$$\kappa_{free} := \frac{\varepsilon_{free.top} - \varepsilon_{free.bottom}}{h} = (2.632 \cdot 10^{-7}) \frac{1}{\text{mm}}$$

Curvature due to free expansion

$$\varepsilon_{free.tpb} := \varepsilon_{free.bottom} + \kappa_{free} \cdot y_c = 1.22 \cdot 10^{-3}$$

Free strain in axis of gravity of concrete-only section

$$\varepsilon_{free.su} := \varepsilon_{free.bottom} + \kappa_{free} \cdot y_{su} = 9.13 \cdot 10^{-4}$$

Free strain at lower reinforcement layer

$$\varepsilon_{free.so} := \varepsilon_{free.bottom} + \kappa_{free} \cdot y_{so} = 1.32 \cdot 10^{-3}$$

Free strain at top reinforcement layer

$$\Delta T_{N,free} := \frac{\varepsilon_{free.tpb}}{\alpha} = 121.74 \text{ K}$$

$$\Delta T_{M,free} := \frac{\kappa_{free}}{\alpha} = 26.32 \frac{\text{K}}{\text{m}}$$

Values from Aas-Jakobsen:

$$\Delta T_{N,free.Aas.Jakobsen} := 121.74 \text{ K}$$

$$\Delta T_{M,free.Aas.Jakobsen} := 26.32 \frac{\text{K}}{\text{m}}$$

Deviation:

$$\frac{\Delta T_{N,free}}{\Delta T_{N,free.Aas.Jakobsen}} = 1$$

$$\frac{\Delta T_{M,free}}{\Delta T_{M,free.Aas.Jakobsen}} = 1$$

3. Contributions from the reinforcement

$$F_{su} := \varepsilon_{free.su} \cdot E_s \cdot A_{su} = 704.75 \text{ kN}$$

$$F_{so} := \varepsilon_{free.so} \cdot E_s \cdot A_{so} = 5415.19 \text{ kN}$$

$$N_{reinforcement} := F_{su} + F_{so} = 6119.95 \text{ kN}$$

$$e_{su} := y_{equivalent} - y_{su} = 1178.21 \text{ mm}$$

$$e_{so} := y_{so} - y_{equivalent} = 369.79 \text{ mm}$$

$$M_{reinforcement} := F_{su} \cdot e_{su} - F_{so} \cdot e_{so} = -1172.15 \text{ kN} \cdot \text{m}$$

$$\varepsilon_{reinforcement.tpb} := \frac{-N_{reinforcement}}{E_{c.long} \cdot A_{equivalent}} = -1.948 \cdot 10^{-4}$$

$$\kappa_{reinforcement} := \frac{M_{reinforcement}}{E_{c.long} \cdot I_{equivalent}} = -1.397 \cdot 10^{-7} \frac{1}{\text{mm}}$$

$$\Delta T_{N.reinforcement} := \frac{\varepsilon_{reinforcement.tpb}}{\alpha} = -19.48 \text{ K}$$

$$\Delta T_{M.reinforcement} := \frac{\kappa_{reinforcement}}{\alpha} = -13.97 \frac{\text{K}}{\text{m}}$$

Values from Aas-Jakobsen:

$$\Delta T_{N.reinforcement.Aas.Jakobsen} := -18.99 \text{ K}$$

$$\Delta T_{M.reinforcement.Aas.Jakobsen} := -13.71 \frac{\text{K}}{\text{m}}$$

Deviation:

$$\frac{\Delta T_{N.reinforcement}}{\Delta T_{N.reinforcement.Aas.Jakobsen}} = 1.026$$

$$\frac{\Delta T_{M.reinforcement}}{\Delta T_{M.reinforcement.Aas.Jakobsen}} = 1.019$$

4. Resulting ASR loads

$$\Delta T_{N.ASR} := \Delta T_{N.free} + \Delta T_{N.reinforcement} = 102.25 \text{ K}$$

$$\Delta T_{M.ASR} := \Delta T_{M.free} + \Delta T_{M.reinforcement} = 12.35 \frac{\text{K}}{\text{m}}$$

Values from Aas-Jakobsen:

$$\Delta T_{N.ASR.Aas.Jakobsen} := \Delta T_{N.free.Aas.Jakobsen} + \Delta T_{N.reinforcement.Aas.Jakobsen} = 102.75 \text{ K}$$

$$\Delta T_{M.ASR.Aas.Jakobsen} := \Delta T_{M.free.Aas.Jakobsen} + \Delta T_{M.reinforcement.Aas.Jakobsen} = 12.61 \frac{\text{K}}{\text{m}}$$

Deviation:

$$\frac{\Delta T_{N.ASR}}{\Delta T_{N.ASR.Aas.Jakobsen}} = 0.995$$

$$\frac{\Delta T_{M.ASR}}{\Delta T_{M.ASR.Aas.Jakobsen}} = 0.979$$

The axial strain results in a deviation equal to 0.5%, whereas the gradient has a deviation equal to 2.1%.

Appendix C

Verification of Bending Moment due to Self-Weight

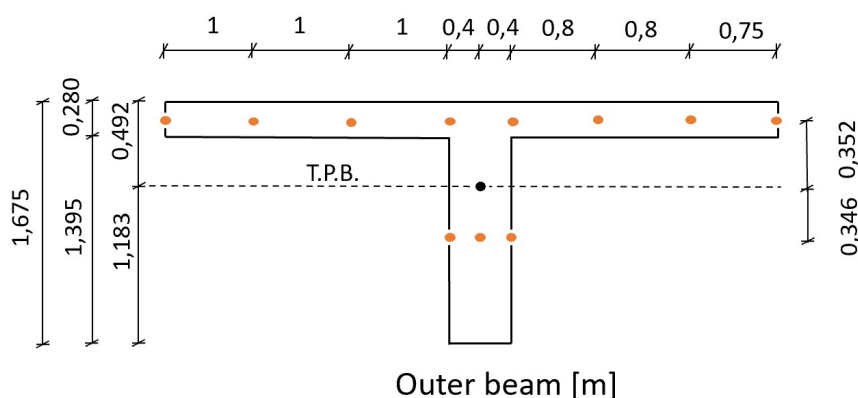
Verification of bending moment due to self-weight

Bending moment and axial forces are extracted from the integration points corresponding to the centre of each element and are summarized from left to right. The total bending moment from Aas-Jakobsen are the sum of the contributions from self-weight and super-self-weight. These values are extracted from the report "Klassifisering av Elgeseter bru 2021, Vedlegg: Resultater fra Aas-Jakobsens analyser".

Verification of self-weight in axis 9

The bending moment is calculated in the longitudinal direction for the outer- and inner beam in axis 9 about the axis of gravity (T.P.B.). The elements have a length of 1,25 meters. Therefore, the bending moment is calculated at 0,625 meters from the columns axis towards the city from axis 9 (corresponding to the integration point).

Outer beam axis 9



Contributions from the plate:

Bending moment in the longitudinal direction (SM1):

$$SM1_{P1} := 16.6 \frac{kN \cdot m}{m} \cdot 1 m = 16.6 kN \cdot m$$

$$SM1_{P2} := 23.1 \frac{kN \cdot m}{m} \cdot 1 m = 23.1 kN \cdot m$$

$$SM1_{P3} := 32.13 \frac{kN \cdot m}{m} \cdot 1 m = 32.13 kN \cdot m$$

$$SM1_{P4} := 34.05 \frac{kN \cdot m}{m} \cdot 0.8 m = 27.24 kN \cdot m$$

$$SM1_{P5} := 26.73 \frac{kN \cdot m}{m} \cdot 0.8 m = 21.384 kN \cdot m$$

$$SM1_{P6} := 19.60 \frac{kN \cdot m}{m} \cdot 0.75 m = 14.7 kN \cdot m$$

$$M_{Plate.SM1} := SM1_{P1} + SM1_{P2} + SM1_{P3} + SM1_{P4} + SM1_{P5} + SM1_{P6} = 135.15 kN \cdot m$$

Axial force in the longitudinal direction (SF1):

$$SF1_{P1} := 196.39 \frac{kN}{m} \cdot 1 m = 196.39 kN$$

$$SF1_{P2} := 371.73 \frac{kN}{m} \cdot 1 m = 371.73 kN$$

$$SF1_{P3} := 715.32 \frac{kN}{m} \cdot 1 \text{ m} = 715.32 \text{ kN}$$

$$SF1_{P4} := 792.78 \frac{kN}{m} \cdot 0.8 \text{ m} = 634.22 \text{ kN}$$

$$SF1_{P5} := 521.25 \frac{kN}{m} \cdot 0.8 \text{ m} = 417 \text{ kN}$$

$$SF1_{P6} := 411.38 \frac{kN}{m} \cdot 0.75 \text{ m} = 308.54 \text{ kN}$$

$$arm_{Plate} := 0.352 \text{ m}$$

$$M_{Plate.SF1} := (SF1_{P1} + SF1_{P2} + SF1_{P3} + SF1_{P4} + SF1_{P5} + SF1_{P6}) \cdot arm_{Plate} = 930.41 \text{ kN} \cdot \text{m}$$

Contributions from the beam:

Bending moment in the longitudinal direction (SM1):

$$SM1_{B1} := 3330.1 \frac{kN \cdot m}{m} \cdot 0.4 \text{ m} = 1332.04 \text{ kN} \cdot \text{m}$$

$$SM1_{B2} := 3326.73 \frac{kN \cdot m}{m} \cdot 0.4 \text{ m} = 1330.69 \text{ kN} \cdot \text{m}$$

$$M_{Beam.SM1} := SM1_{B1} + SM1_{B2} = 2662.73 \text{ kN} \cdot \text{m}$$

Axial force in the longitudinal direction (SF1):

$$SF1_{B1} := -3674.03 \frac{kN}{m} \cdot 0.4 \text{ m} = -1469.61 \text{ kN}$$

$$SF1_{B2} := -3588.9 \frac{kN}{m} \cdot 0.4 \text{ m} = -1435.56 \text{ kN}$$

$$arm_{Beam} := -0.3455 \text{ m}$$

$$M_{Beam.SF1} := (SF1_{B1} + SF1_{B2}) \cdot arm_{Beam} = 1003.74 \text{ kN} \cdot \text{m}$$

Total bending moment:

$$M_{Tot} := M_{Plate.SM1} + M_{Plate.SF1} + M_{Beam.SM1} + M_{Beam.SF1} = 4732 \text{ kN} \cdot \text{m}$$

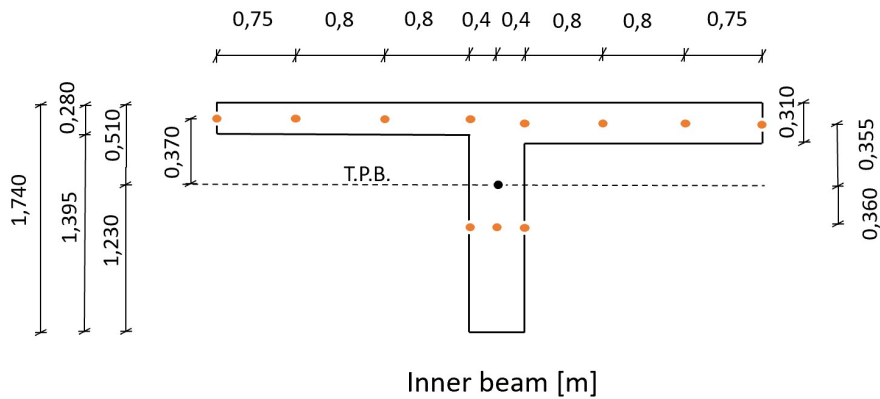
Corresponding bending moment from Aas-Jakobsen:

$$M_{Aas.Jakobsen} := 4800 \text{ kN} \cdot \text{m}$$

Deviation:

$$\frac{M_{Aas.Jakobsen}}{M_{Tot}} = 1.014$$

Inner beam axis 9



Contributions from the plate 280mm:

Bending moment in the longitudinal direction (SM1):

$$SM1_{P1.280} := 15.7 \frac{kN \cdot m}{m} \cdot 0.75 \text{ m} = 11.78 \text{ kN} \cdot m$$

$$SM1_{P2.280} := 14.19 \frac{kN \cdot m}{m} \cdot 0.8 \text{ m} = 11.35 \text{ kN} \cdot m$$

$$SM1_{P3.280} := 13.47 \frac{kN \cdot m}{m} \cdot 0.8 \text{ m} = 10.78 \text{ kN} \cdot m$$

$$M_{Plate.280.SM1} := SM1_{P1.280} + SM1_{P2.280} + SM1_{P3.280} = 33.9 \text{ kN} \cdot m$$

Axial force in the longitudinal direction (SF1):

$$SF1_{P1.280} := 380.13 \frac{kN}{m} \cdot 0.75 \text{ m} = 285.1 \text{ kN}$$

$$SF1_{P2.280} := 416.85 \frac{kN}{m} \cdot 0.8 \text{ m} = 333.48 \text{ kN}$$

$$SF1_{P3.280} := 567.04 \frac{kN}{m} \cdot 0.8 \text{ m} = 453.63 \text{ kN}$$

$$arm_{Plate.280} := 0.370 \text{ m}$$

$$M_{Plate.280.SF1} := (SF1_{P1.280} + SF1_{P2.280} + SF1_{P3.280}) \cdot arm_{Plate.280} = 396.72 \text{ kN} \cdot m$$

Contributions from the plate 310mm:

Bending moment in the longitudinal direction (SM1):

$$SM1_{P1.310} := 16.15 \frac{kN \cdot m}{m} \cdot 0.8 \text{ m} = 12.92 \text{ kN} \cdot m$$

$$SM1_{P2.310} := 11.85 \frac{kN \cdot m}{m} \cdot 0.8 \text{ m} = 9.48 \text{ kN} \cdot m$$

$$SM1_{P3.310} := 8.6 \frac{kN \cdot m}{m} \cdot 0.75 m = 6.45 kN \cdot m$$

$$M_{Plate.310.SM1} := SM1_{P1.310} + SM1_{P2.310} + SM1_{P3.310} = 28.85 kN \cdot m$$

Axial force in the longitudinal direction (SF1):

$$SF1_{P1.310} := 581.51 \frac{kN}{m} \cdot 0.8 m = 465.21 kN$$

$$SF1_{P2.310} := 401.33 \frac{kN}{m} \cdot 0.8 m = 321.06 kN$$

$$SF1_{P3.310} := 337.47 \frac{kN}{m} \cdot 0.75 m = 253.1 kN$$

$$arm_{Plate.310} := 0.355 m$$

$$M_{Plate.310.SF1} := (SF1_{P1.310} + SF1_{P2.310} + SF1_{P3.310}) \cdot arm_{Plate.310} = 368.98 kN \cdot m$$

Contributions from the beam:

Bending moment in the longitudinal direction (SM1):

$$SM1_{B1} := 2309.03 \frac{kN \cdot m}{m} \cdot 0.4 m = 923.61 kN \cdot m$$

$$SM1_{B2} := 2327.51 \frac{kN \cdot m}{m} \cdot 0.4 m = 931 kN \cdot m$$

$$M_{Beam.SM1} := SM1_{B1} + SM1_{B2} = 1854.62 kN \cdot m$$

Axial force in the longitudinal direction (SF1):

$$SF1_{B1} := -2260.3 \frac{kN}{m} \cdot 0.4 m = -904.12 kN$$

$$SF1_{B2} := -2363.73 \frac{kN}{m} \cdot 0.4 m = -945.49 kN$$

$$arm_{Beam} := -0.360 m$$

$$M_{Beam.SF1} := (SF1_{B1} + SF1_{B2}) \cdot arm_{Beam} = 665.86 kN \cdot m$$

Total bending moment:

$$M_{Tot} := M_{Plate.280.SM1} + M_{Plate.280.SF1} + M_{Plate.310.SM1} + M_{Plate.310.SF1} + M_{Beam.SM1} + M_{Beam.SF1} = 3349 kN \cdot m$$

Corresponding bending moment from Aas-Jakobsen:

$$M_{Aas.Jakobsen} := 3400 kN \cdot m$$

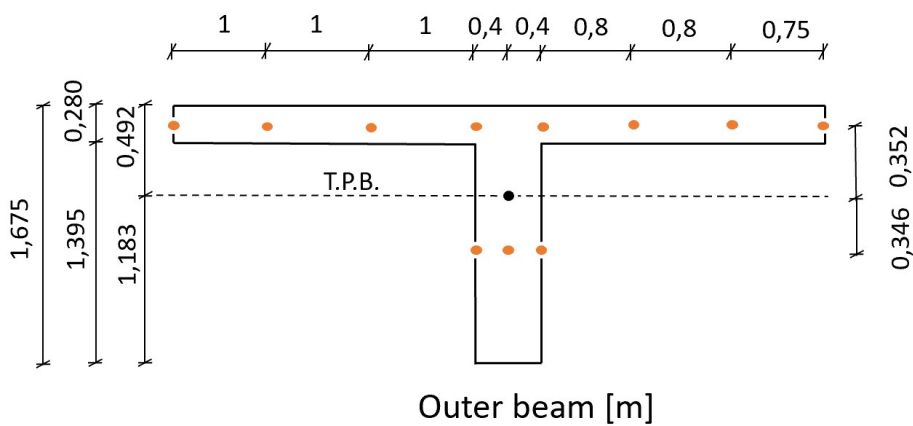
Deviation:

$$\frac{M_{Aas.Jakobsen}}{M_{Tot}} = 1.015$$

Verification of self-weight in axis 8

The bending moment is calculated in the longitudinal direction for the outer- and inner beam in axis 8 about the axis of gravity (T.P). The elements have a length of 1,25 meters. Therefore, the bending moment is calculated at 0,625 meters from the columns axis towards the city from axis 8 (corresponding to the integration point).

Outer beam axis 8



Contributions from the plate:

Bending moment in the longitudinal direction (SM1):

$$SM1_{P1} := 17.04 \frac{kN \cdot m}{m} \cdot 1 \text{ m} = 17.04 \text{ kN} \cdot m$$

$$SM1_{P2} := 23.5 \frac{kN \cdot m}{m} \cdot 1 \text{ m} = 23.5 \text{ kN} \cdot m$$

$$SM1_{P3} := 31.85 \frac{kN \cdot m}{m} \cdot 1 \text{ m} = 31.85 \text{ kN} \cdot m$$

$$SM1_{P4} := 29.37 \frac{kN \cdot m}{m} \cdot 0.8 \text{ m} = 23.496 \text{ kN} \cdot m$$

$$SM1_{P5} := 22.18 \frac{kN \cdot m}{m} \cdot 0.8 \text{ m} = 17.744 \text{ kN} \cdot m$$

$$SM1_{P6} := 16.08 \frac{kN \cdot m}{m} \cdot 0.75 \text{ m} = 12.06 \text{ kN} \cdot m$$

$$M_{Plate.SM1} := SM1_{P1} + SM1_{P2} + SM1_{P3} + SM1_{P4} + SM1_{P5} + SM1_{P6} = 125.69 \text{ kN} \cdot m$$

Axial force in the longitudinal direction (SF1):

$$SF1_{P1} := 184.19 \frac{kN}{m} \cdot 1 \text{ m} = 184.19 \text{ kN}$$

$$SF1_{P2} := 342.25 \frac{kN}{m} \cdot 1 \text{ m} = 342.25 \text{ kN}$$

$$SF1_{P3} := 654.46 \frac{kN}{m} \cdot 1 \text{ m} = 654.46 \text{ kN}$$

$$SF1_{P4} := 693.62 \frac{kN}{m} \cdot 0.8 \text{ m} = 554.9 \text{ kN}$$

$$SF1_{P5} := 450.02 \frac{kN}{m} \cdot 0.8 \text{ m} = 360.016 \text{ kN}$$

$$SF1_{P6} := 350.60 \frac{kN}{m} \cdot 0.75 \text{ m} = 262.95 \text{ kN}$$

$$arm_{Plate} := 0.352 \text{ m}$$

$$M_{Plate.SF1} := (SF1_{P1} + SF1_{P2} + SF1_{P3} + SF1_{P4} + SF1_{P5} + SF1_{P6}) \cdot arm_{Plate} = 830.28 \text{ kN} \cdot \text{m}$$

Contributions from the beam:

Bending moment in the longitudinal direction (SM1):

$$SM1_{B1} := 2925.05 \frac{kN \cdot m}{m} \cdot 0.4 \text{ m} = 1170.02 \text{ kN} \cdot \text{m}$$

$$SM1_{B2} := 3023.52 \frac{kN \cdot m}{m} \cdot 0.4 \text{ m} = 1209.41 \text{ kN} \cdot \text{m}$$

$$M_{Beam.SM1} := SM1_{B1} + SM1_{B2} = 2379.43 \text{ kN} \cdot \text{m}$$

Axial force in the longitudinal direction (SF1):

$$SF1_{B1} := -3034.63 \frac{kN}{m} \cdot 0.4 \text{ m} = -1213.85 \text{ kN}$$

$$SF1_{B2} := -3418.35 \frac{kN}{m} \cdot 0.4 \text{ m} = -1367.34 \text{ kN}$$

$$arm_{Beam} := -0.3455 \text{ m}$$

$$M_{Beam.SF1} := (SF1_{B1} + SF1_{B2}) \cdot arm_{Beam} = 891.8 \text{ kN} \cdot \text{m}$$

Total moment:

$$M_{Tot} := M_{Plate.SM1} + M_{Plate.SF1} + M_{Beam.SM1} + M_{Beam.SF1} = 4227 \text{ kN} \cdot \text{m}$$

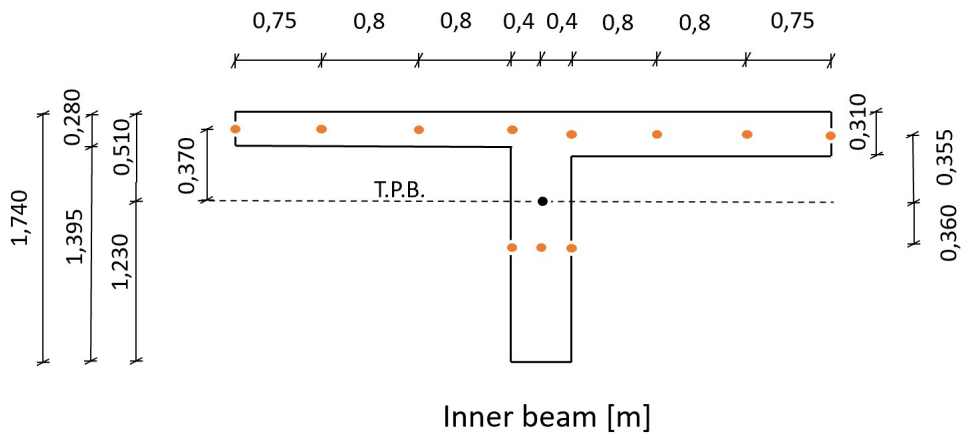
Corresponding moment from Aas-Jakobsen:

$$M_{Aas.Jakobsen} := 3975 \text{ kN} \cdot \text{m}$$

Deviation:

$$\frac{M_{Aas.Jakobsen}}{M_{Tot}} = 0.94$$

Inner beam axis 8



Contributions from the plate 280mm:

Moment in the longitudinal direction (SM1):

$$SM1_{P1,280} := 12.73 \frac{kN \cdot m}{m} \cdot 0.75 \text{ m} = 9.55 \text{ kN} \cdot m$$

$$SM1_{P2,280} := 11.62 \frac{kN \cdot m}{m} \cdot 0.8 \text{ m} = 9.3 \text{ kN} \cdot m$$

$$SM1_{P3,280} := 11.50 \frac{kN \cdot m}{m} \cdot 0.8 \text{ m} = 9.2 \text{ kN} \cdot m$$

$$M_{Plate.280.SM1} := SM1_{P1,280} + SM1_{P2,280} + SM1_{P3,280} = 28.04 \text{ kN} \cdot m$$

Axial force in the longitudinal direction (SF1):

$$SF1_{P1,280} := 319.85 \frac{kN}{m} \cdot 0.75 \text{ m} = 239.89 \text{ kN}$$

$$SF1_{P2,280} := 348.25 \frac{kN}{m} \cdot 0.8 \text{ m} = 278.6 \text{ kN}$$

$$SF1_{P3,280} := 475.77 \frac{kN}{m} \cdot 0.8 \text{ m} = 380.62 \text{ kN}$$

$$arm_{Plate.280} := 0.370 \text{ m}$$

$$M_{Plate.280.SF1} := (SF1_{P1,280} + SF1_{P2,280} + SF1_{P3,280}) \cdot arm_{Plate.280} = 332.67 \text{ kN} \cdot m$$

Contributions from the plate 310mm:

Moment in the longitudinal direction (SM1):

$$SM1_{P1,310} := 14.39 \frac{kN \cdot m}{m} \cdot 0.8 \text{ m} = 11.512 \text{ kN} \cdot m$$

$$SM1_{P2.310} := 10.38 \frac{kN \cdot m}{m} \cdot 0.8 \text{ m} = 8.304 \text{ kN} \cdot m$$

$$SM1_{P3.310} := 7.26 \frac{kN \cdot m}{m} \cdot 0.75 \text{ m} = 5.445 \text{ kN} \cdot m$$

$$M_{Plate.310.SM1} := SM1_{P1.310} + SM1_{P2.310} + SM1_{P3.310} = 25.261 \text{ kN} \cdot m$$

Axial force in the longitudinal direction (SF1):

$$SF1_{P1.310} := 492.19 \frac{kN}{m} \cdot 0.8 \text{ m} = 393.75 \text{ kN}$$

$$SF1_{P2.310} := 333.96 \frac{kN}{m} \cdot 0.8 \text{ m} = 267.17 \text{ kN}$$

$$SF1_{P3.310} := 278.36 \frac{kN}{m} \cdot 0.75 \text{ m} = 208.77 \text{ kN}$$

$$arm_{Plate.310} := 0.355 \text{ m}$$

$$M_{Plate.310.SF1} := (SF1_{P1.310} + SF1_{P2.310} + SF1_{P3.310}) \cdot arm_{Plate.310} = 308.74 \text{ kN} \cdot m$$

Contributions from the beam:

Moment in the longitudinal direction (SM1):

$$SM1_{B1} := 1960.46 \frac{kN \cdot m}{m} \cdot 0.4 \text{ m} = 784.18 \text{ kN} \cdot m$$

$$SM1_{B2} := 1947.40 \frac{kN \cdot m}{m} \cdot 0.4 \text{ m} = 778.96 \text{ kN} \cdot m$$

$$M_{Beam.SM1} := SM1_{B1} + SM1_{B2} = 1563.14 \text{ kN} \cdot m$$

Axial force in the longitudinal direction (SF1):

$$SF1_{B1} := -1946.67 \frac{kN}{m} \cdot 0.4 \text{ m} = -778.67 \text{ kN}$$

$$SF1_{B2} := -1918.97 \frac{kN}{m} \cdot 0.4 \text{ m} = -767.59 \text{ kN}$$

$$arm_{Beam} := -0.360 \text{ m}$$

$$M_{Beam.SF1} := (SF1_{B1} + SF1_{B2}) \cdot arm_{Beam} = 556.65 \text{ kN} \cdot m$$

Total moment:

$$M_{Tot} := M_{Plate.280.SM1} + M_{Plate.280.SF1} + M_{Plate.310.SM1} + M_{Plate.310.SF1} + M_{Beam.SM1} + M_{Beam.SF1} = 2815 \text{ kN} \cdot m$$

Corresponding moment from Aas-Jakobsen:

$$M_{Aas.Jakobsen} := 2750 \text{ kN} \cdot m$$

Deviation:

$$\frac{M_{Aas.Jakobsen}}{M_{Tot}} = 0.977$$

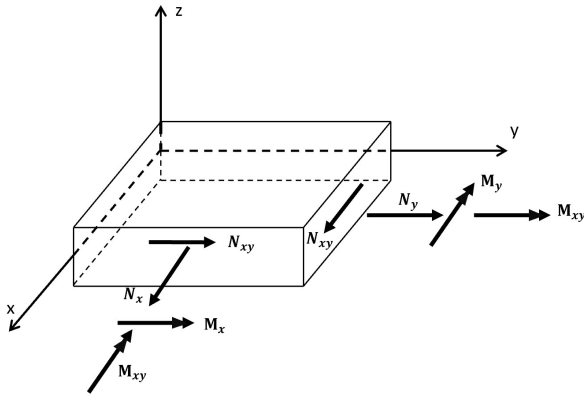
The extracted bending moments from Aas-Jakobsen's report are approximate because they are taken from a coarse moment diagram. However, the deviation indicates that the shell model is transferring the self-weight correctly.

Appendix D

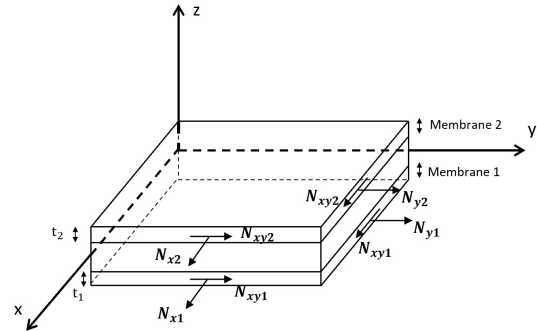
Verification of the Iteration Method by the Membrane Method

Verification of the capacity program using the Membrane Method

Figure a) shows the positive forces action on an element extracted from Abaqus. Important to notice is that the Membrane Method has the same sign-convention as forces from Abaqus, while the Iteration Method has opposite signs for the moments. Moments in the Membrane Method increase the membrane forces in membrane 2 and decrease the forces in membrane 1. The equivalent membrane forces are shown in Figure b).



a) Forces from Abaqus



b) Equivalent membrane forces in layer 1 and layer 2

Capacity control Column axis 6, section B (S1B), ULSa-TE

Cross-section parameters:

$h := 280 \text{ mm}$	Height at the critical section
$c_1 := 46 \text{ mm}$	Distance from bottom surface to centre reinforcement layer
$c_2 := 45 \text{ mm}$	Distance from top surface to centre reinforcement layer
$A_{sx1} := 442 \frac{\text{mm}^2}{\text{m}}$	$A_{sx2} := 221 \frac{\text{mm}^2}{\text{m}}$ Longitudinal reinforcement in the two membrane layers
$A_{sy1} := 804 \frac{\text{mm}^2}{\text{m}}$	$A_{sy2} := 643 \frac{\text{mm}^2}{\text{m}}$ Transverse reinforcement in the two membrane layers

External section forces:

$n_x := 504.9 \frac{\text{kN}}{\text{m}}$	$m_x := 12.1 \text{ kN} \cdot \frac{\text{m}}{\text{m}}$
$n_y := 79.6 \frac{\text{kN}}{\text{m}}$	$m_y := 20.8 \text{ kN} \cdot \frac{\text{m}}{\text{m}}$
$n_{xy} := 3.7 \frac{\text{kN}}{\text{m}}$	$m_{xy} := 0.4 \text{ kN} \cdot \frac{\text{m}}{\text{m}}$

Procedure:

1. Assume uncracked:

$$t_1 := \frac{h}{2} \quad ; \quad t_2 := \frac{h}{2} \quad ; \quad k_1 := 0.5 \quad ; \quad k_2 := 0.5 \quad ; \quad z := h - \frac{(t_1 + t_2)}{2} = 0.14 \text{ m}$$

2. Membrane forces in each layer:

$$\begin{aligned} n_{x1} &:= k_1 \cdot n_x - \frac{m_x}{z} = 166 \frac{kN}{m} & n_{x2} &:= k_2 \cdot n_x + \frac{m_x}{z} = 339 \frac{kN}{m} \\ n_{y1} &:= k_1 \cdot n_y - \frac{m_y}{z} = -109 \frac{kN}{m} & n_{y2} &:= k_2 \cdot n_y + \frac{m_y}{z} = 188 \frac{kN}{m} \\ n_{xy1} &:= k_1 \cdot n_{xy} - \frac{m_{xy}}{z} = -1 \frac{kN}{m} & n_{xy2} &:= k_2 \cdot n_{xy} + \frac{m_{xy}}{z} = 5 \frac{kN}{m} \end{aligned}$$

3. Largest principal membrane force in each layer:

$$\begin{aligned} n_{11} &:= \frac{n_{x1} + n_{y1}}{2} + \sqrt{\left(\frac{n_{x1} - n_{y1}}{2}\right)^2 + n_{xy1}^2} = 166 \frac{kN}{m} & \text{--> membrane 1 is cracked!} \\ n_{21} &:= \frac{n_{x2} + n_{y2}}{2} + \sqrt{\left(\frac{n_{x2} - n_{y2}}{2}\right)^2 + n_{xy2}^2} = 339 \frac{kN}{m} & \text{--> membrane 2 is cracked!} \end{aligned}$$

4. New thickness in each layer:

$$\begin{aligned} t_1 &:= 2 \cdot c_1 = 0.092 \text{ m} & ; & & t_2 &:= 2 \cdot c_2 = 0.09 \text{ m} & & z &:= h - \left(\frac{t_1 + t_2}{2}\right) = 0.189 \text{ m} \\ k_1 &:= \frac{h - t_2}{2h - t_1 - t_2} = 0.503 & ; & & k_2 &:= 1 - k_1 = 0.497 \end{aligned}$$

5. New membrane forces:

$$\begin{aligned} n_{x1} &:= k_1 \cdot n_x - \frac{m_x}{z} = 190 \frac{kN}{m} & n_{x2} &:= k_2 \cdot n_x + \frac{m_x}{z} = 315 \frac{kN}{m} \\ n_{y1} &:= k_1 \cdot n_y - \frac{m_y}{z} = -70 \frac{kN}{m} & n_{y2} &:= k_2 \cdot n_y + \frac{m_y}{z} = 150 \frac{kN}{m} \\ n_{xy1} &:= k_1 \cdot n_{xy} - \frac{m_{xy}}{z} = -0.26 \frac{kN}{m} & n_{xy2} &:= k_2 \cdot n_{xy} + \frac{m_{xy}}{z} = 4 \frac{kN}{m} \end{aligned}$$

Assuming yielding in reinforcement for both directions. Calculate the crack angles:

$$\tan\phi_{1.S1B} := \tan\phi_1^2 + \left(\frac{n_{x1}}{n_{xy1}} - \frac{n_{y1}}{n_{xy1}} \cdot \frac{A_{sx1}}{A_{sy1}}\right) \cdot \tan\phi_1 - \frac{A_{sx1}}{A_{sy1}} \xrightarrow{\text{solve, } \tan\phi_1} \begin{bmatrix} -0.00061801104915623021291 \\ 889.54921523113426419 \end{bmatrix}$$

$$\tan\phi_{2.S1B} := \tan\phi_2^2 + \left(\frac{n_{x2}}{n_{xy2}} - \frac{n_{y2}}{n_{xy2}} \cdot \frac{A_{sx2}}{A_{sy2}}\right) \cdot \tan\phi_2 - \frac{A_{sx2}}{A_{sy2}} \xrightarrow{\text{solve, } \tan\phi_2} \begin{bmatrix} -66.65385874947156792 \\ 0.0051565116579493287853 \end{bmatrix}$$

$$\text{root}\phi_{1.1} := \tan\phi_{1.S1B_0} = -6.18 \cdot 10^{-4} \quad ; \quad \text{root}\phi_{1.2} := \tan\phi_{1.S1B_1} = 889.549$$

$$\text{root}\phi_{2.1} := \tan\phi_{2.S1B_0} = -66.654 \quad ; \quad \text{root}\phi_{2.2} := \tan\phi_{2.S1B_1} = 0.005$$

Selecting the root with same sign as the in-plane shear forces:

$$\tan\phi_{1.S1B} := \begin{cases} \text{if } n_{xy1} \leq 0 \\ \quad \left\| \text{root}\phi_{1.1} \right\| \\ \text{else} \\ \quad \left\| \text{root}\phi_{1.1} \right\| \end{cases} = -6.18 \cdot 10^{-4} \quad \tan\phi_{2.S1B} := \begin{cases} \text{if } n_{xy2} \leq 0 \\ \quad \left\| \text{root}\phi_{2.1} \right\| \\ \text{else} \\ \quad \left\| \text{root}\phi_{2.2} \right\| \end{cases} = 0.005$$

$$\phi_{1.S1B} := \text{atan}(\tan\phi_{1.S1B}) = -0.00062$$

$$\phi_{2.S1B} := \text{atan}(\tan\phi_{2.S1B}) = 0.00516$$

Internal forces from compression field theory:

$$F_{sx1} := n_{x1} + n_{xy1} \cdot \tan\phi_{1.S1B} = 190 \frac{\text{kN}}{\text{m}}$$

$$F_{sx2} := n_{x2} + n_{xy2} \cdot \tan\phi_{2.S1B} = 315 \frac{\text{kN}}{\text{m}}$$

$$F_{sy1} := n_{y1} + \frac{n_{xy1}}{\tan\phi_{1.S1B}} = 345 \frac{\text{kN}}{\text{m}}$$

$$F_{sy2} := n_{y2} + \frac{n_{xy2}}{\tan\phi_{2.S1B}} = 917 \frac{\text{kN}}{\text{m}}$$

$$F_{c1} := \frac{n_{xy1}}{\sin(\phi_{1.S1B}) \cdot \cos(\phi_{1.S1B})} = 415 \frac{\text{kN}}{\text{m}}$$

$$F_{c2} := \frac{n_{xy2}}{\sin(\phi_{2.S1B}) \cdot \cos(\phi_{2.S1B})} = 767 \frac{\text{kN}}{\text{m}}$$

Calculating required reinforcement:

$$f_{yd} := 272 \text{ MPa}$$

$$A_{sx1.req} := \frac{F_{sx1}}{f_{yd}} = 698 \frac{\text{mm}^2}{\text{m}}$$

$$A_{sx2.req} := \frac{F_{sx2}}{f_{yd}} = 1159 \frac{\text{mm}^2}{\text{m}}$$

$$A_{sy1.req} := \frac{F_{sy1}}{f_{yd}} = 1269 \frac{\text{mm}^2}{\text{m}}$$

$$A_{sy2.req} := \frac{F_{sy2}}{f_{yd}} = 3371 \frac{\text{mm}^2}{\text{m}}$$

Control of concrete stresses in compression field:

$$f_{ck} := 25 \text{ MPa} \quad ; \quad f_{cd} := 12 \text{ MPa}$$

$$\sigma_{Rd.max} := 0.6 \cdot \left(1 - \frac{f_{ck}}{250 \cdot \text{MPa}}\right) \cdot f_{cd} = 6.48 \text{ MPa}$$

$$\sigma_{c1} := \frac{F_{c1}}{t_1} = 4.51 \text{ MPa}$$

$$\sigma_{c2} := \frac{F_{c2}}{t_2} = 8.526 \text{ MPa}$$

Utilization ratios:

$$UR_{sx1.Membrane} := \frac{A_{sx1.req}}{A_{sx1}} = 1.578$$

$$UR_{sx2.Membrane} := \frac{A_{sx2.req}}{A_{sx2}} = 5.243$$

$$UR_{sy1.Membrane} := \frac{A_{sy1.req}}{A_{sy1}} = 1.578$$

$$UR_{sy2.Membrane} := \frac{A_{sy2.req}}{A_{sy2}} = 5.243$$

$$UR_{c1.Membrane} := \frac{\sigma_{c1}}{f_{cd}} = 0.376$$

$$UR_{c2.Membrane} := \frac{\sigma_{c2}}{f_{cd}} = 0.71$$

$$UR_{c1.red.Membrane} := \frac{\sigma_{c1}}{\sigma_{Rd.max}} = 0.696$$

$$UR_{c2.red.Membrane} := \frac{\sigma_{c2}}{\sigma_{Rd.max}} = 1.316$$

Utilization ratios from the Iteration Method in the capacity program:

$$UR_{sx1} := 1.58$$

$$UR_{sx2} := 5.26$$

$$UR_{sy1} := 0.04$$

$$UR_{sy2} := 0.84$$

$$UR_c := 0.27$$

$$UR_{c.red} := 0.51$$

Deviation:

$$UR_{s1} := \frac{UR_{sx1.Membrane}}{UR_{sx1}} = 0.999$$

$$UR_{s2} := \frac{UR_{sx2.Membrane}}{UR_{sx2}} = 0.997$$

$$UR_{c1} := \frac{UR_{c1.Membrane}}{UR_c} = 1.393$$

$$UR_{c2} := \frac{UR_{c2.Membrane}}{UR_c} = 2.631$$

$$UR_{c1.red} := \frac{UR_{c1.red.Membrane}}{UR_{c.red}} = 1.366$$

$$UR_{c2.red} := \frac{UR_{c2.red.Membrane}}{UR_{c.red}} = 2.58$$

The deviation is equal to 0.1% and 1.3% for the reinforcement in layers 1 and 2, respectively. The utilization ratio of the concrete is difficult to compare because the two layers are independent in the Membrane Method, while the Iteration Method includes the strain compatibility in the cross-section.

Capacity control Column axis 6 section D (S1D), ULSa-TR

Cross-section parameters:

$$h := 370 \text{ mm}$$

Height at the critical section

$$c_1 := 53 \text{ mm}$$

Distance from bottom surface to centre reinforcement layer

$$c_2 := 99 \text{ mm}$$

Distance from top surface to centre reinforcement layer

$$A_{sx1} := 781 \frac{\text{mm}^2}{\text{m}}$$

$$A_{sx2} := 4685 \frac{\text{mm}^2}{\text{m}}$$

Longitudinal reinforcement in the two membrane layers

$$A_{sy1} := 1539 \frac{\text{mm}^2}{\text{m}}$$

$$A_{sy2} := 766 \frac{\text{mm}^2}{\text{m}}$$

Transverse reinforcement in the two membrane layers

External section forces:

$$n_x := 1101.6 \frac{\text{kN}}{\text{m}}$$

$$m_x := 5.8 \text{ kN} \cdot \frac{\text{m}}{\text{m}}$$

$$n_y := 7.5 \frac{\text{kN}}{\text{m}}$$

$$m_y := -16.7 \text{ kN} \cdot \frac{\text{m}}{\text{m}}$$

$$n_{xy} := -148.7 \frac{\text{kN}}{\text{m}}$$

$$m_{xy} := 4.5 \text{ kN} \cdot \frac{\text{m}}{\text{m}}$$

Procedure:

1. Assume uncracked:

$$t_1 := \frac{h}{2} \quad ; \quad t_2 := \frac{h}{2} \quad ; \quad k_1 := 0.5 \quad ; \quad k_2 := 0.5 \quad ; \quad z := h - \frac{(t_1 + t_2)}{2} = 0.185 \text{ m}$$

2. Membrane forces in each layer:

$$\begin{aligned} n_{x1} &:= k_1 \cdot n_x - \frac{m_x}{z} = 519 \frac{\text{kN}}{\text{m}} & n_{x2} &:= k_2 \cdot n_x + \frac{m_x}{z} = 582 \frac{\text{kN}}{\text{m}} \\ n_{y1} &:= k_1 \cdot n_y - \frac{m_y}{z} = 94 \frac{\text{kN}}{\text{m}} & n_{y2} &:= k_2 \cdot n_y + \frac{m_y}{z} = -87 \frac{\text{kN}}{\text{m}} \\ n_{xy1} &:= k_1 \cdot n_{xy} - \frac{m_{xy}}{z} = -99 \frac{\text{kN}}{\text{m}} & n_{xy2} &:= k_2 \cdot n_{xy} + \frac{m_{xy}}{z} = -50 \frac{\text{kN}}{\text{m}} \end{aligned}$$

3. Largest principal membrane force in each layer:

$$\begin{aligned} n_{11} &:= \frac{n_{x1} + n_{y1}}{2} + \sqrt{\left(\frac{n_{x1} - n_{y1}}{2}\right)^2 + n_{xy1}^2} = 541 \frac{\text{kN}}{\text{m}} & \text{--> membrane 1 is cracked!} \\ n_{21} &:= \frac{n_{x2} + n_{y2}}{2} + \sqrt{\left(\frac{n_{x2} - n_{y2}}{2}\right)^2 + n_{xy2}^2} = 586 \frac{\text{kN}}{\text{m}} & \text{--> membrane 2 is cracked!} \end{aligned}$$

4. New thicknesses:

$$\begin{aligned} t_1 &:= 2 \cdot c_1 = 0.106 \text{ m} & ; & & t_2 &:= 2 \cdot c_2 = 0.198 \text{ m} & ; & & z &:= h - \left(\frac{t_1 + t_2}{2}\right) = 0.218 \text{ m} \\ k_1 &:= \frac{h - t_2}{2h - t_1 - t_2} = 0.394 & ; & & k_2 &:= 1 - k_1 = 0.606 \end{aligned}$$

5. New membrane forces:

$$\begin{aligned} n_{x1} &:= k_1 \cdot n_x - \frac{m_x}{z} = 408 \frac{\text{kN}}{\text{m}} & n_{x2} &:= k_2 \cdot n_x + \frac{m_x}{z} = 694 \frac{\text{kN}}{\text{m}} \\ n_{y1} &:= k_1 \cdot n_y - \frac{m_y}{z} = 80 \frac{\text{kN}}{\text{m}} & n_{y2} &:= k_2 \cdot n_y + \frac{m_y}{z} = -72 \frac{\text{kN}}{\text{m}} \\ n_{xy1} &:= k_1 \cdot n_{xy} - \frac{m_{xy}}{z} = -79 \frac{\text{kN}}{\text{m}} & n_{xy2} &:= k_2 \cdot n_{xy} + \frac{m_{xy}}{z} = -69 \frac{\text{kN}}{\text{m}} \end{aligned}$$

Assuming yielding in reinforcement for both directions. Calculate the crack angles:

$$\tan\phi_{1.S1D} := \tan\phi_1^2 + \left(\frac{n_{x1}}{n_{xy1}} - \frac{n_{y1}}{n_{xy1}} \cdot \frac{A_{sx1}}{A_{sy1}}\right) \cdot \tan\phi_1 - \frac{A_{sx1}}{A_{sy1}} \xrightarrow{\text{solve, } \tan\phi_1} \begin{bmatrix} 4.742281149788915271 \\ -0.10701018531724027739 \end{bmatrix}$$

$$\tan\phi_{2.S1D} := \tan\phi_2^2 + \left(\frac{n_{x2}}{n_{xy2}} - \frac{n_{y2}}{n_{xy2}} \cdot \frac{A_{sx2}}{A_{sy2}}\right) \cdot \tan\phi_2 - \frac{A_{sx2}}{A_{sy2}} \xrightarrow{\text{solve, } \tan\phi_2} \begin{bmatrix} 16.712473566425448815 \\ -0.36596545479917836128 \end{bmatrix}$$

$$\text{root}\phi_{1.1} := \tan\phi_{1.S1D0} = 4.742 \quad ; \quad \text{root}\phi_{1.2} := \tan\phi_{1.S1D1} = -0.107$$

$$\text{root}\phi_{2.1} := \tan\phi_{2.S1D0} = 16.712 \quad ; \quad \text{root}\phi_{2.2} := \tan\phi_{2.S1D1} = -0.366$$

Selecting the root with same sign as the in-plane shear forces:

$$\tan\phi_{1.S1D} := \begin{cases} \text{if } n_{xy1} \leq 0 \\ \quad \left\| \begin{array}{l} \text{root}\phi_{1.2} \\ \text{else} \\ \text{root}\phi_{1.1} \end{array} \right\| \\ \text{else} \\ \quad \left\| \begin{array}{l} \text{root}\phi_{1.1} \\ \text{else} \\ \text{root}\phi_{1.2} \end{array} \right\| \end{cases} = -0.107$$

$$\tan\phi_{2.S1D} := \begin{cases} \text{if } n_{xy2} \leq 0 \\ \quad \left\| \begin{array}{l} \text{root}\phi_{2.2} \\ \text{else} \\ \text{root}\phi_{2.1} \end{array} \right\| \\ \text{else} \\ \quad \left\| \begin{array}{l} \text{root}\phi_{2.1} \\ \text{else} \\ \text{root}\phi_{2.2} \end{array} \right\| \end{cases} = -0.366$$

$$\phi_{1.S1D} := \text{atan}(\tan\phi_{1.S1D}) = -0.107$$

$$\phi_{2.S1D} := \text{atan}(\tan\phi_{2.S1D}) = -0.351$$

Internal forces from compression field theory:

$$F_{sx1} := n_{x1} + n_{xy1} \cdot \tan\phi_{1.S1D} = 416 \frac{\text{kN}}{\text{m}}$$

$$F_{sx2} := n_{x2} + n_{xy2} \cdot \tan\phi_{2.S1D} = 719 \frac{\text{kN}}{\text{m}}$$

$$F_{sy1} := n_{y1} + \frac{n_{xy1}}{\tan\phi_{1.S1D}} = 821 \frac{\text{kN}}{\text{m}}$$

$$F_{sy2} := n_{y2} + \frac{n_{xy2}}{\tan\phi_{2.S1D}} = 118 \frac{\text{kN}}{\text{m}}$$

$$F_{c1} := \frac{n_{xy1}}{\sin(\phi_{1.S1D}) \cdot \cos(\phi_{1.S1D})} = 750 \frac{\text{kN}}{\text{m}}$$

$$F_{c2} := \frac{n_{xy2}}{\sin(\phi_{2.S1D}) \cdot \cos(\phi_{2.S1D})} = 215 \frac{\text{kN}}{\text{m}}$$

Calculating required reinforcement:

$$f_{yd} := 272 \text{ MPa}$$

$$A_{sx1.req} := \frac{F_{sx1}}{f_{yd}} = 1531 \frac{\text{mm}^2}{\text{m}}$$

$$A_{sx2.req} := \frac{F_{sx2}}{f_{yd}} = 2643 \frac{\text{mm}^2}{\text{m}}$$

$$A_{sy1.req} := \frac{F_{sy1}}{f_{yd}} = 3017 \frac{\text{mm}^2}{\text{m}}$$

$$A_{sy2.req} := \frac{F_{sy2}}{f_{yd}} = 432 \frac{\text{mm}^2}{\text{m}}$$

Control of concrete stresses in compression field:

$$f_{ck} := 25 \text{ MPa} \quad ; \quad f_{cd} := 12 \text{ MPa}$$

$$\sigma_{Rd.max} := 0.6 \cdot \left(1 - \frac{f_{ck}}{250 \cdot \text{MPa}}\right) \cdot f_{cd} = 6.48 \text{ MPa}$$

$$\sigma_{c1} := \frac{F_{c1}}{t_1} = 7.07 \text{ MPa}$$

$$\sigma_{c2} := \frac{F_{c2}}{t_2} = 1.086 \text{ MPa}$$

Utilization ratios:

$$UR_{sx1.Membrane} := \frac{A_{sx1.req}}{A_{sx1}} = 1.96$$

$$UR_{sx2.Membrane} := \frac{A_{sx2.req}}{A_{sx2}} = 0.564$$

$$UR_{sy1.Membrane} := \frac{A_{sy1.req}}{A_{sy1}} = 1.96$$

$$UR_{sy2.Membrane} := \frac{A_{sy2.req}}{A_{sy2}} = 0.564$$

$$UR_{c1.Membrane} := \frac{\sigma_{c1}}{f_{cd}} = 0.589$$

$$UR_{c2.Membrane} := \frac{\sigma_{c2}}{f_{cd}} = 0.09$$

$$UR_{c1.red.Membrane} := \frac{\sigma_{c1}}{\sigma_{Rd.max}} = 1.091$$

$$UR_{c2.red.Membrane} := \frac{\sigma_{c2}}{\sigma_{Rd.max}} = 0.168$$

Utilization ratios from the Iteration Method in the capacity program:

$$UR_{sx1} := 2.09$$

$$UR_{sx2} := 0.59$$

$$UR_{sy1} := 0.55$$

$$UR_{sy2} := 0.18$$

$$UR_c := 0.13$$

$$UR_{c.red} := 0.25$$

Deviation:

$$UR_{s1} := \frac{UR_{sr1.Membrane}}{UR_{sr1}} = 0.938$$

$$UR_{s2} := \frac{UR_{sr2.Membrane}}{UR_{sr2}} = 0.956$$

$$UR_{c1} := \frac{UR_{c1.Membrane}}{UR_c} = 4.533$$

$$UR_{c2} := \frac{UR_{c2.Membrane}}{UR_c} = 0.696$$

$$UR_{c1.red} := \frac{UR_{c1.red.Membrane}}{UR_{c.red}} = 4.365$$

$$UR_{c2.red} := \frac{UR_{c2.red.Membrane}}{UR_{c.red}} = 0.67$$

The deviation is equal to 6.2% and 4.4% for the reinforcement in layers 1 and 2, respectively. The utilization ratio of the concrete is difficult to compare because the two layers are independent in the Membrane Method, while the Iteration Method includes the strain compatibility in the cross-section.

Capacity control in axis of zero bending moment, section A (S2A) ULSa-TR

Cross-section parameters:

$$h := 255 \text{ mm}$$

Height at the critical section

$$c_1 := 47 \text{ mm}$$

Distance from bottom surface to centre reinforcement layer

$$c_2 := 67 \text{ mm}$$

Distance from top surface to centre reinforcement layer

$$A_{sr1} := 442 \frac{\text{mm}^2}{\text{m}}$$

$$A_{sr2} := 4243 \frac{\text{mm}^2}{\text{m}}$$

Longitudinal reinforcement in the two membrane layers

$$A_{sy1} := 709 \frac{\text{mm}^2}{\text{m}}$$

$$A_{sy2} := 1835 \frac{\text{mm}^2}{\text{m}}$$

Transverse reinforcement in the two membrane layers

External section forces:

$$n_x := -967.8 \frac{\text{kN}}{\text{m}}$$

$$m_x := 8.9 \text{ kN} \cdot \frac{\text{m}}{\text{m}}$$

$$n_y := -0.5 \frac{\text{kN}}{\text{m}}$$

$$m_y := 89.8 \text{ kN} \cdot \frac{\text{m}}{\text{m}}$$

$$n_{xy} := -314.6 \frac{\text{kN}}{\text{m}}$$

$$m_{xy} := 2.2 \text{ kN} \cdot \frac{\text{m}}{\text{m}}$$

Procedure:

1. Assume uncracked:

$$t_1 := \frac{h}{2} ; \quad t_2 := \frac{h}{2} ; \quad k_1 := 0.5 ; \quad ; \quad k_2 := 0.5 ; \quad ; \quad z := h - \frac{(t_1 + t_2)}{2} = 0.128 \text{ m}$$

2. Membrane forces in each layer:

$$n_{x1} := k_1 \cdot n_x - \frac{m_x}{z} = -554 \frac{\text{kN}}{\text{m}}$$

$$n_{x2} := k_2 \cdot n_x + \frac{m_x}{z} = -414 \frac{\text{kN}}{\text{m}}$$

$$n_{y1} := k_1 \cdot n_y - \frac{m_y}{z} = -705 \frac{\text{kN}}{\text{m}}$$

$$n_{y2} := k_2 \cdot n_y + \frac{m_y}{z} = 704 \frac{\text{kN}}{\text{m}}$$

$$n_{xy1} := k_1 \cdot n_{xy} - \frac{m_{xy}}{z} = -175 \frac{kN}{m} \quad n_{xy2} := k_2 \cdot n_{xy} + \frac{m_{xy}}{z} = -140 \frac{kN}{m}$$

3. Largest principal membrane force in each layer:

$$n_{111} := \frac{n_{x1} + n_{y1}}{2} + \sqrt{\left(\frac{n_{x1} - n_{y1}}{2}\right)^2 + n_{xy1}^2} = -439 \frac{kN}{m} \quad \text{--> membrane 1 is uncracked!}$$

$$n_{211} := \frac{n_{x2} + n_{y2}}{2} + \sqrt{\left(\frac{n_{x2} - n_{y2}}{2}\right)^2 + n_{xy2}^2} = 721 \frac{kN}{m} \quad \text{--> membrane 2 is cracked!}$$

4. New thickness in each layer:

$$t_1 := \frac{h}{2} = 0.128 \text{ m} ; \quad t_2 := 2 \cdot c_2 = 0.134 \text{ m} ; \quad z := 0.75 \cdot h - c_2 = 0.124 \text{ m}$$

$$k_1 := \frac{0.25 \cdot h}{0.75 \cdot h - c_2} = 0.513 \quad k_2 := 1 - k_1 = 0.487$$

5. New membrane forces:

$$n_{x1} := k_1 \cdot n_x - \frac{m_x}{z} = -568 \frac{kN}{m} \quad n_{x2} := k_2 \cdot n_x + \frac{m_x}{z} = -400 \frac{kN}{m}$$

$$n_{y1} := k_1 \cdot n_y - \frac{m_y}{z} = -723 \frac{kN}{m} \quad n_{y2} := k_2 \cdot n_y + \frac{m_y}{z} = 722 \frac{kN}{m}$$

$$n_{xy1} := k_1 \cdot n_{xy} - \frac{m_{xy}}{z} = -179 \frac{kN}{m} \quad n_{xy2} := k_2 \cdot n_{xy} + \frac{m_{xy}}{z} = -135 \frac{kN}{m}$$

Assuming yielding in reinforcement for both directions. Calculate the crack angles:

$$\tan\phi_{1.S2A} := \tan\phi_1^2 + \left(\frac{n_{x1}}{n_{xy1}} - \frac{n_{y1}}{n_{xy1}} \cdot \frac{A_{sx1}}{A_{sy1}} \right) \cdot \tan\phi_1 - \frac{A_{sx1}}{A_{sy1}} \xrightarrow{\text{solve, } \tan\phi_1} \begin{bmatrix} 0.52705168833192271093 \\ -1.1828313463582067445 \end{bmatrix}$$

$$\tan\phi_{2.S2A} := \tan\phi_2^2 + \left(\frac{n_{x2}}{n_{xy2}} - \frac{n_{y2}}{n_{xy2}} \cdot \frac{A_{sx2}}{A_{sy2}} \right) \cdot \tan\phi_2 - \frac{A_{sx2}}{A_{sy2}} \xrightarrow{\text{solve, } \tan\phi_2} \begin{bmatrix} 0.14985048647403928698 \\ -15.430457616712889829 \end{bmatrix}$$

$$\text{root}\phi_{1.1} := \tan\phi_{1.S2A_0} = 0.527 \quad ; \quad \text{root}\phi_{1.2} := \tan\phi_{1.S2A_1} = -1.183$$

$$\text{root}\phi_{2.1} := \tan\phi_{2.S2A_0} = 0.15 \quad ; \quad \text{root}\phi_{2.2} := \tan\phi_{2.S2A_1} = -15.43$$

Selecting the root with same sign as the in-plane shear forces:

$$\tan\phi_{1.S2A} := \begin{cases} \text{if } n_{xy1} \leq 0 \\ \quad \left\| \begin{array}{l} \text{root}\phi_{1.2} \\ \text{else} \\ \text{root}\phi_{1.1} \end{array} \right\| \end{cases} = -1.183$$

$$\tan\phi_{2.S2A} := \begin{cases} \text{if } n_{xy2} \leq 0 \\ \quad \left\| \begin{array}{l} \text{root}\phi_{2.2} \\ \text{else} \\ \text{root}\phi_{2.1} \end{array} \right\| \end{cases} = -15.43$$

$$\phi_{1.S2A} := \text{atan}(\tan\phi_{1.S2A}) = -0.86896$$

$$\phi_{2.S2A} := \text{atan}(\tan\phi_{2.S2A}) = -1.50608$$

Internal forces from compression field theory:

$$F_{sx1} := n_{x1} + n_{xy1} \cdot \tan\phi_{1.S2A} = -356 \frac{kN}{m}$$

$$F_{sx2} := n_{x2} + n_{xy2} \cdot \tan\phi_{2.S2A} = 1691 \frac{kN}{m}$$

$$F_{sy1} := n_{y1} + \frac{n_{xy1}}{\tan\phi_{1.S2A}} = -572 \frac{\text{kN}}{\text{m}}$$

$$F_{c1} := \frac{n_{xy1}}{\sin(\phi_{1.S2A}) \cdot \cos(\phi_{1.S2A})} = 363 \frac{\text{kN}}{\text{m}}$$

$$F_{sy2} := n_{y2} + \frac{n_{xy2}}{\tan\phi_{2.S2A}} = 731 \frac{\text{kN}}{\text{m}}$$

$$F_{c2} := \frac{n_{xy2}}{\sin(\phi_{2.S2A}) \cdot \cos(\phi_{2.S2A})} = 2099 \frac{\text{kN}}{\text{m}}$$

Calculating required reinforcement:

$$f_{yd} := 272 \text{ MPa}$$

$$A_{sx1.req} := \frac{F_{sx1}}{f_{yd}} = -1310 \frac{\text{mm}^2}{\text{m}}$$

$$A_{sx2.req} := \frac{F_{sx2}}{f_{yd}} = 6217 \frac{\text{mm}^2}{\text{m}}$$

$$A_{sy1.req} := \frac{F_{sy1}}{f_{yd}} = -2101 \frac{\text{mm}^2}{\text{m}}$$

$$A_{sy2.req} := \frac{F_{sy2}}{f_{yd}} = 2689 \frac{\text{mm}^2}{\text{m}}$$

Control of concrete stresses in compression field:

$$f_{ck} := 25 \text{ MPa} \quad ; \quad f_{cd} := 12 \text{ MPa}$$

$$\sigma_{Rd.max} := 0.6 \cdot \left(1 - \frac{f_{ck}}{250 \cdot \text{MPa}}\right) \cdot f_{cd} = 6.48 \text{ MPa}$$

$$\sigma_{c1} := \frac{F_{c1}}{t_1} = 2.85 \text{ MPa}$$

$$\sigma_{c2} := \frac{F_{c2}}{t_2} = 15.666 \text{ MPa}$$

Utilization ratios:

$$UR_{sx1.Membrane} := \frac{A_{sx1.req}}{A_{sx1}} = -2.964 \text{ (Compression)}$$

$$UR_{sx2.Membrane} := \frac{A_{sx2.req}}{A_{sx2}} = 1.465$$

$$UR_{sy1.Membrane} := \frac{A_{sy1.req}}{A_{sy1}} = -2.964 \text{ (Compression)}$$

$$UR_{sy2.Membrane} := \frac{A_{sy2.req}}{A_{sy2}} = 1.465$$

$$UR_{c1.Membrane} := \frac{\sigma_{c1}}{f_{cd}} = 0.237$$

$$UR_{c2.Membrane} := \frac{\sigma_{c2}}{\sigma_{Rd.max}} = 2.418$$

Utilization ratios from the Iteration Method in the capacity program:

$$UR_{sx1} := 0.19$$

$$UR_{sx2} := 0.03$$

$$UR_{sy1} := 0.22$$

$$UR_{sy2} := 1.23$$

$$UR_c := 1.13$$

Deviation:

$$UR_{s2} := \frac{UR_{sy2.Membrane}}{UR_{sy2}} = 1.191$$

$$UR_{c1} := \frac{UR_{c1.Membrane}}{UR_c} = 0.21$$

$$UR_{c2} := \frac{UR_{c2.Membrane}}{UR_c} = 2.14$$

The reinforcement in layer 1 is in compression and will therefore not have a utilization ratio. The deviation of the reinforcement in layer 2 is 19.1%.

Capacity control in axis 10, section A (S7A), ULSa-TE

Cross-section parameters:

$h := 255 \text{ mm}$	Height at the critical section
$c_1 := 47 \text{ mm}$	Distance from bottom surface to centre reinforcement layer
$c_2 := 43 \text{ mm}$	Distance from top surface to centre reinforcement layer
$A_{sx1} := 442 \frac{\text{mm}^2}{\text{m}}$	$A_{sx2} := 221 \frac{\text{mm}^2}{\text{m}}$ Longitudinal reinforcement in the two membrane layers
$A_{sy1} := 709 \frac{\text{mm}^2}{\text{m}}$	$A_{sy2} := 1835 \frac{\text{mm}^2}{\text{m}}$ Transverse reinforcement in the two membrane layers

External section forces:

$n_x := 40.3 \frac{\text{kN}}{\text{m}}$	$m_x := 12.9 \text{ kN} \cdot \frac{\text{m}}{\text{m}}$
$n_y := -94.5 \frac{\text{kN}}{\text{m}}$	$m_y := 116.1 \text{ kN} \cdot \frac{\text{m}}{\text{m}}$
$n_{xy} := 38.8 \frac{\text{kN}}{\text{m}}$	$m_{xy} := 0.5 \text{ kN} \cdot \frac{\text{m}}{\text{m}}$

Procedure:

1. Assume uncracked:

$$t_1 := \frac{h}{2} \quad ; \quad t_2 := \frac{h}{2} \quad ; \quad k_1 := 0.5 \quad ; \quad k_2 := 0.5 \quad ; \quad z := h - \frac{(t_1 + t_2)}{2} = 0.128 \text{ m}$$

2. Membrane forces in each layer:

$$\begin{aligned} n_{x1} &:= k_1 \cdot n_x - \frac{m_x}{z} = -81 \frac{\text{kN}}{\text{m}} & n_{x2} &:= k_2 \cdot n_x + \frac{m_x}{z} = 121 \frac{\text{kN}}{\text{m}} \\ n_{y1} &:= k_1 \cdot n_y - \frac{m_y}{z} = -958 \frac{\text{kN}}{\text{m}} & n_{y2} &:= k_2 \cdot n_y + \frac{m_y}{z} = 863 \frac{\text{kN}}{\text{m}} \\ n_{xy1} &:= k_1 \cdot n_{xy} - \frac{m_{xy}}{z} = 15 \frac{\text{kN}}{\text{m}} & n_{xy2} &:= k_2 \cdot n_{xy} + \frac{m_{xy}}{z} = 23 \frac{\text{kN}}{\text{m}} \end{aligned}$$

3. Largest principal membrane force in each layer:

$$\begin{aligned} n_{111} &:= \frac{n_{x1} + n_{y1}}{2} + \sqrt{\left(\frac{n_{x1} - n_{y1}}{2}\right)^2 + n_{xy1}^2} = -81 \frac{\text{kN}}{\text{m}} & \text{--> membrane 1 is uncracked!} \\ n_{211} &:= \frac{n_{x2} + n_{y2}}{2} + \sqrt{\left(\frac{n_{x2} - n_{y2}}{2}\right)^2 + n_{xy2}^2} = 864 \frac{\text{kN}}{\text{m}} & \text{--> membrane 2 is cracked!} \end{aligned}$$

4. New thickness in each layer:

$$t_1 := \frac{h}{2} = 0.128 \text{ m} ; \quad t_2 := 2 \cdot c_2 = 0.086 \text{ m} ; \quad z := 0.75 \cdot h - c_2 = 0.148 \text{ m}$$

$$k_1 := \frac{0.25 \cdot h}{0.75 \cdot h - c_2} = 0.43 \quad k_2 := 1 - k_1 = 0.57$$

5. New membrane forces:

$$n_{x1} := k_1 \cdot n_x - \frac{m_x}{z} = -70 \frac{\text{kN}}{\text{m}} \quad n_{x2} := k_2 \cdot n_x + \frac{m_x}{z} = 110 \frac{\text{kN}}{\text{m}}$$

$$n_{y1} := k_1 \cdot n_y - \frac{m_y}{z} = -824 \frac{\text{kN}}{\text{m}} \quad n_{y2} := k_2 \cdot n_y + \frac{m_y}{z} = 729 \frac{\text{kN}}{\text{m}}$$

$$n_{xy1} := k_1 \cdot n_{xy} - \frac{m_{xy}}{z} = 13 \frac{\text{kN}}{\text{m}} \quad n_{xy2} := k_2 \cdot n_{xy} + \frac{m_{xy}}{z} = 25 \frac{\text{kN}}{\text{m}}$$

Assuming yielding in reinforcement for both directions. Calculate the crack angles:

$$\tan\phi_{1.S7A} := \tan\phi_1^2 + \left(\frac{n_{x1}}{n_{xy1}} - \frac{n_{y1}}{n_{xy1}} \cdot \frac{A_{sx1}}{A_{sy1}} \right) \cdot \tan\phi_1 - \frac{A_{sx1}}{A_{sy1}} \xrightarrow{\text{solve, } \tan\phi_1} \begin{bmatrix} -33.362025311753091828 \\ 0.018686313324341017988 \end{bmatrix}$$

$$\tan\phi_{2.S7A} := \tan\phi_2^2 + \left(\frac{n_{x2}}{n_{xy2}} - \frac{n_{y2}}{n_{xy2}} \cdot \frac{A_{sx2}}{A_{sy2}} \right) \cdot \tan\phi_2 - \frac{A_{sx2}}{A_{sy2}} \xrightarrow{\text{solve, } \tan\phi_2} \begin{bmatrix} 0.12155676597931030329 \\ -0.99077962737961658239 \end{bmatrix}$$

$$\text{root}\phi_{1.1} := \tan\phi_{1.S7A_0} = -33.362 ; \quad \text{root}\phi_{1.2} := \tan\phi_{1.S7A_1} = 0.019$$

$$\text{root}\phi_{2.1} := \tan\phi_{2.S7A_0} = 0.122 ; \quad \text{root}\phi_{2.2} := \tan\phi_{2.S7A_1} = -0.991$$

Selecting the root with same sign as the in-plane shear forces:

$$\tan\phi_{1.S7A} := \begin{cases} \text{if } n_{xy1} \leq 0 \\ \quad \left\| \begin{array}{l} \text{root}\phi_{1.1} \\ \text{root}\phi_{1.2} \end{array} \right\| \\ \text{else} \\ \quad \left\| \begin{array}{l} \text{root}\phi_{1.1} \\ \text{root}\phi_{1.2} \end{array} \right\| \end{cases} = 0.019$$

$$\tan\phi_{2.S7A} := \begin{cases} \text{if } n_{xy2} \leq 0 \\ \quad \left\| \begin{array}{l} \text{root}\phi_{2.2} \\ \text{root}\phi_{2.1} \end{array} \right\| \\ \text{else} \\ \quad \left\| \begin{array}{l} \text{root}\phi_{2.2} \\ \text{root}\phi_{2.1} \end{array} \right\| \end{cases} = 0.122$$

$$\phi_{1.S7A} := \text{atan}(\tan\phi_{1.S7A}) = 0.01868$$

$$\phi_{2.S7A} := \text{atan}(\tan\phi_{2.S7A}) = 0.12096$$

Internal forces from compression field theory:

$$F_{sx1} := n_{x1} + n_{xy1} \cdot \tan\phi_{1.S7A} = -69 \frac{\text{kN}}{\text{m}}$$

$$F_{sx2} := n_{x2} + n_{xy2} \cdot \tan\phi_{2.S7A} = 113 \frac{\text{kN}}{\text{m}}$$

$$F_{sy1} := n_{y1} + \frac{n_{xy1}}{\tan\phi_{1.S7A}} = -111 \frac{\text{kN}}{\text{m}}$$

$$F_{sy2} := n_{y2} + \frac{n_{xy2}}{\tan\phi_{2.S7A}} = 939 \frac{\text{kN}}{\text{m}}$$

$$F_{c1} := \frac{n_{xy1}}{\sin(\phi_{1.S7A}) \cdot \cos(\phi_{1.S7A})} = 713 \frac{\text{kN}}{\text{m}}$$

$$F_{c2} := \frac{n_{xy2}}{\sin(\phi_{2.S7A}) \cdot \cos(\phi_{2.S7A})} = 213 \frac{\text{kN}}{\text{m}}$$

Calculating required reinforcement:

$$f_{yd} := 272 \text{ MPa}$$

$$A_{sx1.req} := \frac{F_{sx1}}{f_{yd}} = -255 \frac{mm^2}{m}$$

$$A_{sx2.req} := \frac{F_{sx2}}{f_{yd}} = 416 \frac{mm^2}{m}$$

$$A_{sy1.req} := \frac{F_{sy1}}{f_{yd}} = -409 \frac{mm^2}{m}$$

$$A_{sy2.req} := \frac{F_{sy2}}{f_{yd}} = 3452 \frac{mm^2}{m}$$

Control of concrete stresses in compression field:

$$f_{ck} := 25 \text{ MPa} \quad ; \quad f_{cd} := 12 \text{ MPa}$$

$$\sigma_{Rd.max} := 0.6 \cdot \left(1 - \frac{f_{ck}}{250 \cdot \text{MPa}} \right) \cdot f_{cd} = 6.48 \text{ MPa}$$

$$\sigma_{c1} := \frac{F_{c1}}{t_1} = 5.59 \text{ MPa}$$

$$\sigma_{c2} := \frac{F_{c2}}{t_2} = 2.474 \text{ MPa}$$

Utilization ratios:

$$UR_{sx1.Membrane} := \frac{A_{sx1.req}}{A_{sx1}} = -0.578 \text{ (Compression)}$$

$$UR_{sx2.Membrane} := \frac{A_{sx2.req}}{A_{sx2}} = 1.881$$

$$UR_{sy1.Membrane} := \frac{A_{sy1.req}}{A_{sy1}} = -0.578 \text{ (Compression)}$$

$$UR_{sy2.Membrane} := \frac{A_{sy2.req}}{A_{sy2}} = 1.881$$

$$UR_{c1.Membrane} := \frac{\sigma_{c1}}{f_{cd}} = 0.466$$

$$UR_{c2.Membrane} := \frac{\sigma_{c2}}{f_{cd}} = 0.206$$

Utilization ratios from the Iteration Method in the capacity program:

$$UR_{sx1} := 0.20$$

$$UR_{sx2} := 1.56$$

$$UR_{sy1} := 0.29$$

$$UR_{sy2} := 1.21$$

$$UR_c := 1.23$$

Deviation:

$$UR_{s2} := \frac{UR_{sx2.Membrane}}{UR_{sx2}} = 1.206$$

$$UR_{c1} := \frac{UR_{c1.Membrane}}{UR_c} = 0.379$$

$$UR_{c2} := \frac{UR_{c2.Membrane}}{UR_c} = 0.168$$

The reinforcement in layer 1 is in compression and will therefore not have a utilization ratio. The deviation of the reinforcement in layer 2 is 20.6%.

